Micro/Nano Structured Materials for Enhanced Device Performance and Antibacterial Applications

by

Md Imrul Kayes

B.S. in E.E., Bangladesh University of Engineering and Technology, 2011

M.S. in I.E., University of Pittsburgh, 2015

Submitted to the Graduate Faculty of
the Swanson School of Engineering in partial fulfillment
of the requirements for the degree of

Doctor of Philosophy

University of Pittsburgh

2019

UNIVERSITY OF PITTSBURGH

SWANSON SCHOOL OF ENGINEERING

This dissertation was presented

by

Md Imrul Kayes

It was defended on

May 30, 2019

and approved by

Paul W. Leu, Ph.D., Associate Professor, Department of Industrial Engineering

M. Ravi Shankar, Ph.D., Professor, Department of Industrial Engineering

Young Jae Chun, Ph.D., Associate Professor, Department of Industrial Engineering

Robert M. Shanks, Ph.D., Associate Professor, Department of Ophthalmology

Dissertation Director: Paul W. Leu, Ph.D., Associate Professor, Department of Industrial Engineering

Micro/Nano Structured Materials for Enhanced Device Performance and Antibacterial Applications

Md Imrul Kayes, PhD

University of Pittsburgh, 2019

Micro/nanostructured materials have been used extensively for various applications due to their unique chemical, physical, and mechanical properties. In this thesis we report the fabrication and characterization of micro/nanostructured materials with antibacterial properties. Plastics are used in a wide range of medical components such as prosthetics, implants, catheters, and syringes. However, contaminating bacteria can attach to plastic surfaces and grow and form biofilms that lead to healthcare associated infections. The consequences on patients and their families are serious, as infections can extend hospital stays, create long-term disability, increase healthcare costs, and even result in unnecessary deaths. Two strategies for creating antibacterial surfaces are (1) anti-biofouling surfaces that make the bacterial attachment process difficult and (2) bactericidal surfaces that kill bacteria cells that come in proximity of or contact the surface. We demonstrate that a fluorine etch chemistry may be utilized to create lotus leaf-inspired, low surface energy, hierarchical micro-structure/nanofibrils in Polypropylene (PP). Our anti-biofouling PP surfaces exhibit a 99.6% reduction of *Escherichia coli* cell adhesion compared to untreated PP. We also fabricated bactericidal surfaces consisting of uniform and regular nanostructured arrays. The interest in mechanical bactericidal effect has recently increased, as the bacteria cells grow drug resistance. Nanosphere lithography and combination of reactive ion etching and deep reactive ion etching were utilized to prepare these substrates. The pitch, diameter, taper, and height of the nanostructures are controlled. The bactericidal effect of these structures is investigated and significant enhancement in killing is observed.

We also report fabrication of micro/nanostructured materials to improve device performance. Our simulation results show that absorption enhancement in vertical nanowire arrays on a perfectly electric conductor can be further improved through tilting. Tilted

nanowire arrays, with the same amount of material, exhibit improved performance over vertical nanowire arrays over a broad range of tilt angles. The optimum tilt of 53° has an improvement of 8.6% over that of vertical nanowire arrays and 80.4% of the ideal double pass thin film. Incorporation of these structures could improve the efficiency of solar cells.

Table of Contents

List of Tables

List of Figures

Preface

This work is dedicated to my parents: Md Abdul Jabbar, Kawser Parveen and my wife Sabrina Rashid.

I would first like to thank my academic advisor, Dr. Paul Leu, for giving me the opportunity to pursue my Ph.D degree at University of Pittsburgh. I would also like to thank Professors Ravi Shankar, Youngjae Chun, and Robert Shanks for serving on my candidacy and thesis committees. I appreciate their time and the valuable suggestions on my research.

I would also thank Professors Tuan Tran, Robert Shanks, Graham Hatfull, and Bryan Brown their helpful suggestions and insightful discussions for different projects. I would like to acknowledge and thank all of the students and staff members that I have worked with in the last five years. I'd like to thank the staff members who helped me at University of Pittsburgh: Mike McDonald, Matthew France, Dr. Susheng Tan, Dr. Jun Chen, Dr. Esta Abelev and Joanna Barr in the Gertrude E. & John M. Petersen Institute of NanoScience and Engineering, and Cole van Ormer in the Materials Micro-Characterization Laboratory, and Dr. Joel Gillespie in the Materials Characterization Laboratory. I also would like to thank the CMU Nanofab staff members: Norman Gottron, Mason Risley, and Dr. Matthew Moneck for the training sessions and helpful advice.

I would like to thank the lab members of our research group Laboratory of Advanced Materials at Pittsburgh (LAMP), with whom I worked on different projects: Tongchuan, Sajad, Ziyu, Anthony, Brad, Baomin, Zhengyu, Sooraj, Mohamed, Rafael, Luke, Sean, Linkon, Dalton, Brendan, Donny, and Miriam . I also would like to thank my collaborators who have helpmed me to conduct different experiments: Carlos, Gabby, Emily, Binh, Nick, Aimon, and Alexis.

I would like to express my sincere gratitude to all the Bangladeshi friends here in Pittsburgh for their continuous help and support. I would definitely miss my Pittsburgh family. I would also thank my friends from Faujdarhat Cadet College, who have always been there for me. I would also thank the members of the two table tennis clubs in Pittsburgh. I enjoyed playing table tennis with them and it helped me to remain fit and active. I would like to

thank Fakhrul vai, Mark, and Akbar for the training sessions, which helped me to improve my skills over the years. I would also thank my friends at the Department of Industrial Engineering- specially Hamdy and Anna for their help and for being such good friends.

Lastly but most importantly, I would like to thank my mom, and dad for their love and support. They have always helped though out my academic career and personal life. And my wife Sabrina for bearing with me through difficult times and for her unconditional support. I would not be able to finish this journey without her.

1.0 Introduction

Micro/nano structured materials have been studied extensively in the recent years and the use of these materials have increased drastically over the years. These materials have their unique chemical, physical, and mechanical advantages and have vast application in various research fields. Micro/nanostructured materials have been used for electronic devices, sensors, water treatment, automotive, aerospace engineering, communication engineering, medicine, and antibacterial applications [1]. Nanotubes, polymeric nanofibers, nanoparticles, nanowires, nanocomposites, and micropillars are some of the commonly reported micro/nanostructures that have been used for the above-mentioned applications.

1.1 Types of Micro/Nano Structures

Nanotubes

Nanotubes are hollow tube-like structures, generally having diameter in the nanoscale, while the length ranges from nanoscale to microscale [2]. Based on the number of layers of atoms wrapped around the hollow core nanotubes can be categorized as single walled or multi walled. Nanotubes made of different materials such as Carbon, Boron Nitride, Titania, Silica, Silicon etc have been fabricated [3, 4, 5, 6, 7, 8]. Among these Carbon nanonubes (CNTs) have been studied extensively and used for various applications such as energy storage materials, gas storage materials, polymer reinforcements, electronics, field emission displays and radiation sources; semiconductor devices, probes, interconnects and biosensors [9, 10, 11]. The combination of superior thermal, mechanical and electronic properties of CNTs have made them useful for different application [12]. Titania nanotubes have also shown enhanced properties for application in sensing, photoelectrolysis, photocatalysis, and photovoltaics [13].

Nanoparticles

Nanoparticles (NPs) are microscopic particles having a size between 1-100 nm. NPs being cheap, easy, and reproducible have been used for electronic, optoelectronic, and photoelectronic applications [14, 15, 16]. Novel applications such as cleaning up pollutants in water and leaving only biodegradable compounds have also been reported [17]. NPs have been used in the biological field extensively due to having important properties such as fluorescence and magnetic behavior [18]. The size of NPs being comparable to biomolecules such as proteins also play an important role. Silver NPs have found considerable usage in the biomedical field, while their plasmonic-resonance optical scattering property have enabled them to be used for bio-sensing and imaging applications [19]. Gold NPs have been used to develop colorimetric biosensors due to their size dependent optical and chemical properties [20]. They have also been used in drug delivery applications, as the gold core is inert and non-toxic [21].

Nanofibers

Nanofibers (NFs) have found considerable interest due to the advantages they offer. They are lightweight, have high surface area to volume ratio have small diameters and have controllable pore structures [22, 23]. NFs have been used for chemical, biological, and optical sensors, as well as for biomedical applications such as tissue engineering and drug delivery [24]. NFs have also been used for piezoelectric polymeric nanogenerators capable to convert mechanical energy to electricity [25]. Electrospun polymeric NFs have been used for wound dressing as they support cell adhesion, migration, growth which are impoortant for the wound healing process [26]. Carbon NFs have been used to remove cationic pollutants, to develop supercapacitors, and as an electrode for vanadium redox flow battery [27, 28, 29, 30].

Nanowires

Silicon nanostructures have been subjected to comprehensive studies to evaluate their significant impact on electronic devices. Due to their unique electrical, optical, and structural properties these nanostructured surfaces have been used for various applications. Silicon nanowires (SiNWs) have been used for various applications such as photovoltaics [31, 32], chemical and biological sensors [33, 34, 35, 36, 37, 38], field effect transistors [39] etc. Similarly silicon nanocone (SiNC) arrays have been used for self-cleaning antireflection coatings [40], solar cells [41], fuel cells [42, 43], improved lithium-ion batteries [44] etc. The use of nanostructured surfaces is not limited to these scopes only. They have also been used for antibacterial biomedical devices [45, 46]. Nanowire structures have been used in solar cells as they provide several advantages such as reduced reflection, improved band gap tuning, extreme light trapping, increased defect tolerance, enhanced charge transport capacity [47, 48]. This results in significant cost reductions as reduced amount of materials are used. Nanowires have also been used for highly transparent flexible metal electrode touch panel, high performance anode for lithium ion batteries, gas sensors, supercapacitors, fully stretchable light-emitting diodes etc [49, 50, 51, 52, 53].

Nanocomposites

Nanocomposites (NCs) can be regarded as multiphase nanostructures with one phase being at the nanoscale dimension [23]. Continuously fabricated transparent conductive polycarbonate/carbon nanotube NC films have been used for switchable thermochromic applications [54]. These transparent conductors have shown excellent mechanical flexibility, and good environmental resistance. NC hydrogels have also been used for environmental protection applications such as ion exchangers, adsorption, photocatalysis and soil conditioning and biomedical engineering applications such as drug delivery agents, wound dressing, and tissue engineering [55]. Graphene based NC fibers have shown antibacterial property, low cytotoxicity, and ultrahigh ultimate tensile strength [56]. Different NC materials also have been used for antibacterial applications [57, 58, 59, 60].

Mircopillars

Micropillars (MPs) have been used to study boiling heat transfer and critical heat flux extensively [61, 62, 63]. Boiling heat transfer on MP substrate was reported to increase with the surface roughness ratio [64]. MP structured surfaces have been used to study wetting behaviors and transition from the CassieBaxter state to the Wenzel state [65]. MP arrays have been used for optoelectronic applications [66, 67]. Incorporation of tilted MPs also enhanced the performance of flexible capacitive Pressure sensors [68]. MPs have also been used for solar cells and showed improved efficiency [69, 70]. MPs have been used as an anti reflection coating for solar cells and shown stretchability without affecting the device functionality [71, 72].

1.2 Dissertation Outline

The research focus of this dissertation is divided into two parts. In the first part we evaluate the use of silicon nanostructures to improve device performance. In our first study, we did Finite-Difference Time-Domain (FDTD) simulation to evaluate the optical performance of tilted Silicon nanowire array. Silicon nanowire arrays have been shown to demonstrate light trapping properties and promising potential for next-generation photovoltaics. In this study, we performed systematic and detailed simulation studies on the optical properties of tilted silicon nanowire arrays as compared to vertical nanowires arrays. Our results show that the absorption enhancement in vertical nanowire arrays on a perfectly electric conductor can be further improved through tilting. Tilted nanowire arrays exhibit improved absorption over the solar spectrum compared with vertical nanowires since the tilt removes symmetry requirements on the resonance modes in the nanowires. The results were published in [73].

Then we did experimental and theoretical analysis to control critical heat flux and boiling crisis using Silicon nanopillars. Boiling is a key heat transfer process for a variety of power generation and electronics cooling technologies. In such applications, it is very important to improve the energy efficiency by increasing the critical heat flux(CHF),and to reduce the operational risks by avoiding the boiling crisis. In this study, we show that nanopillar arrays fabricated on a substrate enhance both the critical heat flux (CHF) and the critical temperature at CHF of the substrate and thus, effectively increase the limit of boiling before the boiling crisis is triggered. We conclude that the enhancement in both the CHF and the critical temperature results from an intensified rewetting process which increases with the height of nanopillars. The results were published in [74].

Infections due to bacterial adhesion is very common for implanted medical devices and extensive research is being done to address this issue. In the second part of the thesis we evaluate the adhesion and killing of bacteria cells by antibacterial surfaces. First we report on the micro/nanostructuring and surface functionalization of Polypropylene (PP) substrate, which is used in a wide variety of medical components, through various oxygen and fluorine reactive ion etching (RIE) treatments and their effects on wettability and bacteria adhesion. The results were published in [75].

The interest in mechanical bactericidal effect has increased, as the bacteria cells grow drug resistance. We fabricated uniform and regular nanostructured arrays with control over pitch, diameter, taper, and height. Nanosphere lithography and combination of reactive ion etching and deep reactive ion etching were utilized to prepare uniform silicon nanostructure arrays of different morphology. The bactericidal effect of these structures were investigated against Gram-positive bacteria (*Staphylococcus epidermidis*). Gram-positive bacteria have a thicker cell wall compared to Gram-negative bacteria, and has been reported difficult to kill mechanically. Our results shows that the center-to-center spacing among the pillars plays an important role in the bactericidal performance of the substrate. Significant enhancement in killing (82%) was observed for 1μm long, 300 nm pitch nanostructured surface with a tip diameter of 80 nm compared to the flat control substrates.

2.0 Tilted Silicon Nanowire Arrays for Photovoltaics

2.1 Introduction

Silicon is a naturally abundant, stable, non-toxic material that has been used extensively for semiconductor devices so that its processing and manufacturing is well developed. While silicon has an almost-ideal band gap for single p-n junction photovoltaics, its infrared absorption is poor. Typical single-crystalline silicon photovoltaics are thus usually several hundred microns thick to absorb sunlight effectively. These silicon solar cells require costly manufacturing processes such as purification, crystallization, and wafer slicing in order to ensure that generated carriers are collected efficiently. Light trapping helps address this issue by increasing the distance photons travel in the silicon before escaping to increase absorption and efficiencies for a particular active layer thickness. Manufacturing costs are reduced because less silicon and poorer quality silicon may be used. Poorer quality silicon with smaller minority carrier diffusion lengths may be used because charge carriers have to diffuse over smaller distances in order to be collected. A variety of structures have been investigated for utilizing light trapping to increase absorption in thin film silicon photovoltaics such as diffraction gratings [76], grating couplers [77], photonic crystals [78, 79, 80, 81], and random surface textures [82, 83]. These structures contain features that are the same size or smaller than the wavelength of light, such that conventional geometrical light trapping limits (the Yablonovitch or Lambertian limit [84, 85]) are no longer applicable. Much solar cell research has focused on silicon (Si) nanowires, which have been demonstrated to be a promising active layer material for next-generation solar cells [86, 87, 88, 89, 90, 91, 92, 93, 94, 95]. Nanowires may orthogonalize light absorption and carrier collection processes to facilitate high optical absorption and efficient collection of photogenerated carriers [96]. Furthermore, nanowires have demonstrated light-trapping properties, where their absorption is enhanced over that of planar silicon [88, 86, 87, 94]. These structures may also be deposited on low-cost or flexible substrates using chemical vapor deposition or contact transfer methods [97]. Various

structures that break the symmetry of nanowire arrays such as nanocones [98, 99, 100] or aperiodic vertical arrays [101] have been demonstrated to have increased absorption over vertical nanowire arrays.

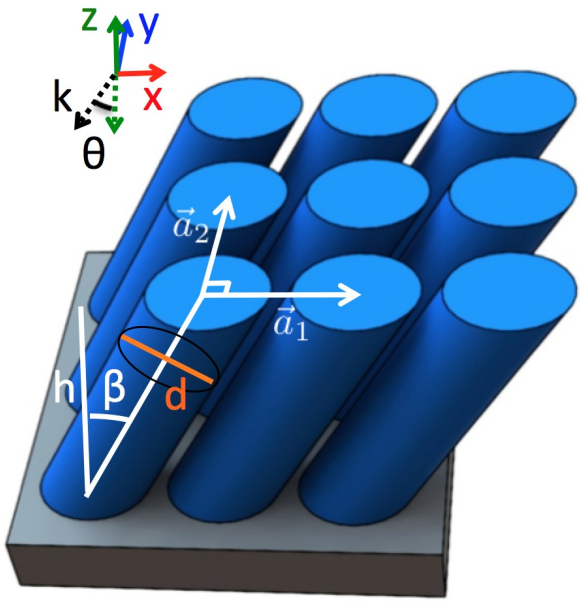

Figure 1: Schematic of the tilted silicon nanowire array structure. The nanowires sit on a perfectly electric conductor and are defined by the height h, circular cross-sectional diameter d, and tilt with respect to the zenith β. The nanowires form a two-dimensional lattice defined by the lattice vectors $\vec{a}_1$ and $\vec{a}_2$, where $|\vec{a}_2| = a$ and $|\vec{a}_1| = a/\cos\alpha$. The incidence angle of the incoming radiation is defined with respect to the negative z-direction.

In this study, we investigate the optical performance of tilted nanowire arrays on a metal contact and compare their performance to that of vertical nanowire arrays. We report how the nanowire tilt may be used to improve solar absorption and thus, ultimate efficiency. We demonstrate that this enhancement occurs over a broad range of incidence angles.

2.2 Methods

Figure 1 shows a schematic of the tilted silicon nanowire arrays studied, which sit on top of a perfectly electric conductor (PEC). The PEC may be, for example, the idealized perfectly reflecting back contact of a solar cell. The parameters of the structure are the height h, circular cross-sectional diameter d, and tilt with respect to the zenith β. The nanowires form a two-dimensional lattice defined by the lattice vectors $\vec{a}_1$ and $\vec{a}_2$ where $\vec{a}_1$ and $\vec{a}_2$ are in the x- and y-directions respectively. The nanowires are tilted in the x-z plane. $|\vec{a}_2| = a$ and $|\vec{a}_1| = a/\cos\beta$, where a is the vertical nanowire pitch. The total nanowire array volume is invariant with β since the fill factor ($\frac{\pi d^2}{4a^2}$) is independent of β. $d \leq a$ in order to avoid the intersection of nanowires. We studied nanowires with $h = 1000$ nm.

Maxwell's equations were solved using the finite difference time domain (FDTD) method, which computes the energy dependent transmission $T(E)$, reflection $R(E)$, and absorption spectra $A(E)$ efficiently. The ultimate efficiency is calculated using the following equation

$$\eta = \frac{\int_{E_g}^{\infty} I(E)A(E)\frac{E_g}{E}dE}{\int_0^{\infty} I(E)dE} \tag{2.1}$$

where E is the photon energy, E_g is the band gap of crystalline silicon, $I(E)$ is the solar irradiance under the global 37° tilt Air Mass 1.5 spectrum [102], and $A(E)$ is the absorption [103]. The ultimate efficiency is the maximum efficiency of a solar cell when the temperature approaches 0 K, where there is no recombination and each absorbed photon produces an electron-hole pair. The band gap $E_g = 1.12$ eV for crystalline silicon. The absorption and reflection spectra was obtained over the energy range of the solar spectrum from $E = 1.12$ to 4.13 eV (wavelengths from 1100 to 300 nm). Assuming each photon produces an electron-hole pair and there is no recombination, such that all photogenerated carriers are collected, the short circuit current density is

$$J_{sc} = q\int_{E_g}^{\infty} b_s(E)A(E)dE \tag{2.2}$$

where q is the elementary charge and $b_s(E)$ is the photon flux density. The irradiance and photon flux density are related by $I(E) = Eb_s(E)$. The total solar absorption is calculated from

$$A_{sol} = \frac{\int_{E_g}^{\infty} b_s(E)A(E)dE}{\int_0^{\infty} b_s(E)dE}. \tag{2.3}$$

The optical constants for silicon were taken from experimental measurement results in Palik's *Handbook of Optical Constants of Solids* [104]. A non-uniform mesh with a minimum size of 15 nm was used for the simulation. Perfectly matched layer boundary conditions were used for the upper boundary of the simulation cell [105], PEC boundary conditions were used for the lower boundary of the simulation cell, while appropriate boundary conditions were used for the side boundaries to model the periodic nature of the arrays.

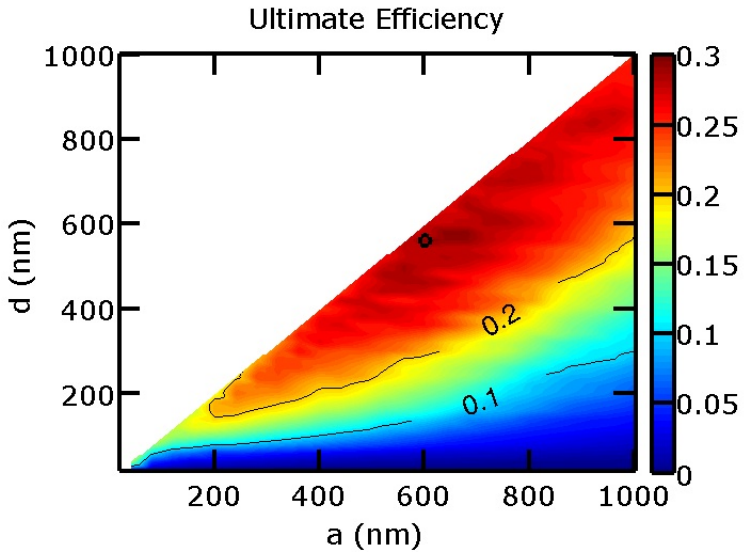

Figure 2: Ultimate efficiency of square arrays of vertical nanowires. The vertical nanowires ($\alpha = 0$) have height $h = 1000$ nm and the ultimate efficiency is shown as a function of array pitch a and nanowire diameter d. The highest ultimate efficiency is 29.7% at $a = 600$ nm, $d = 560$ nm, which is marked with a circle in the contour plot.

2.3 Results and Discussion

We first focused on evaluating vertical nanowires where $\beta = 0$. The vertical nanowires form a square lattice where $|\vec{a}_1| = |\vec{a}_2| = a$. $h = 1000$ nm as mentioned before. We varied the pitch a from 40 nm to 1000 nm and the diameter from 20 nm up to the pitch. Figure 2 shows the results of our studies. The best vertical nanowire array was determined to be with $a = 600$ nm and $d = 560$ nm, which is marked with a circle in the contour plot. The pitch of 600 nm is the same as that found in previous research [87, 106]. High efficiencies are generally achievable from arrays with high fill factors. The best vertical nanowire has an ultimate efficiency of 29.7%.

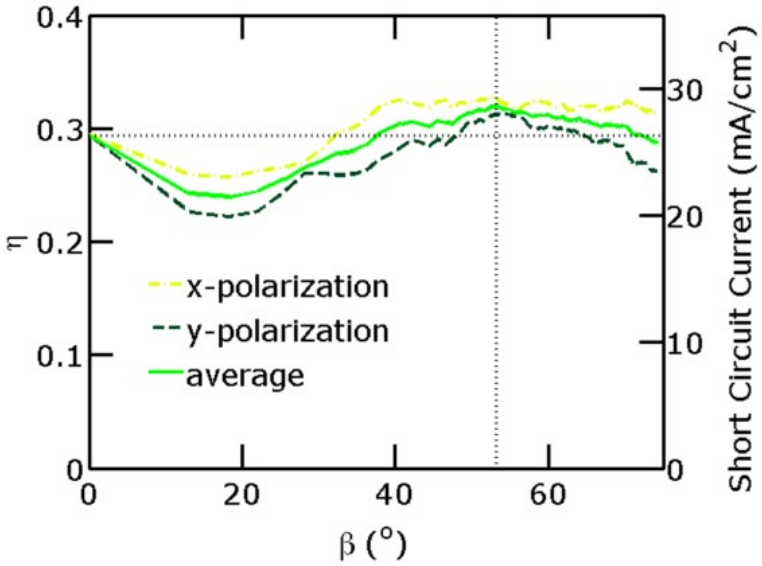

Figure 3: Tilted nanowire array simulation results. Ultimate efficiency η function of nanowire array tilt angle β. The short circuit current density is shown on the right y-axis.The nanowires have height $h = 1000$ nm, diameter $d = 560$ nm, and vertical pitch $a = 600$ nm.

The vertical nanowire array with $a = 600$ nm and $d = 560$ nm has the same amount of silicon as a flat thin film structure with a thickness of $L = 684$ nm. For comparison purposes, we compare the performance of double pass thin films. The double pass thin film assumes perfect antireflection at the front surface of the thin film and perfect reflection at the back surface, such that light passes through the material twice with no light trapping. The absorption for double pass thin films under normal incidence light is

$$A(E) = 1 - \exp[-2\alpha(E)L] \tag{2.4}$$

where $\alpha(E)$ is the energy dependent absorption coefficient of Si. The ultimate efficiency of an ideal double pass thin film with $L = 684$ nm is 17.9%. We also studied the similar properties of the 500nm nanowires. The highest efficiency was obtained for 680 nm pitch and 640 nm diameter, which is shown in Appendix A.

Next, we studied tilted nanowire arrays. The pitch and diameter were fixed at $a = 600$ and $d = 560$ nm respectively, while the nanowires were systematically tilted by varying β. The height is $h = 1000$ nm as before. As mentioned earlier, the amount of silicon does not change as the wires are tilted. Simulation were performed with the normal incident light polarized in the x-direction and then, in the y-direction as the nanowires are tilted. Results of our tilted nanowire array studies are poltted. Figure 3 plots the ultimate efficiency η as a function of the nanowire array tilt angle β. $\eta = 29.7\%$ for the vertical nanowire array ($\beta = 0°$). A horizontal dash-dotted line is shown at this ultimate efficiency for references. The ultimate efficiency is shown for incident light polarized in the x-direction, y-direction, and the average of these two results.

By tilting the nanowires, higher average ultimate efficiencies may be achieved at nanowire array tilts between 38 and 72°. The ultimate efficiency is 32.2% and a maximum at $\beta = 53°$, which is indicated with a vertical dotted line. $\vec{a}_1 = 997$ nm at this tilt. Figure 4 plots the absorption as a function of the wavelength and nanowire tilt angle β. The absorption shown is the average of the two polarizations. The optimum tilt of $\beta = 53°$ is again marked with a dashed line in the contour plot. Normal incident light can only couple to HE_{1m} in vertical nanowires due to symmetry requirements [107]. Distinct resonance peaks can be seen in the absorption spectrum of the vertical nanowire array. For tilts less than 38°, the ultimate

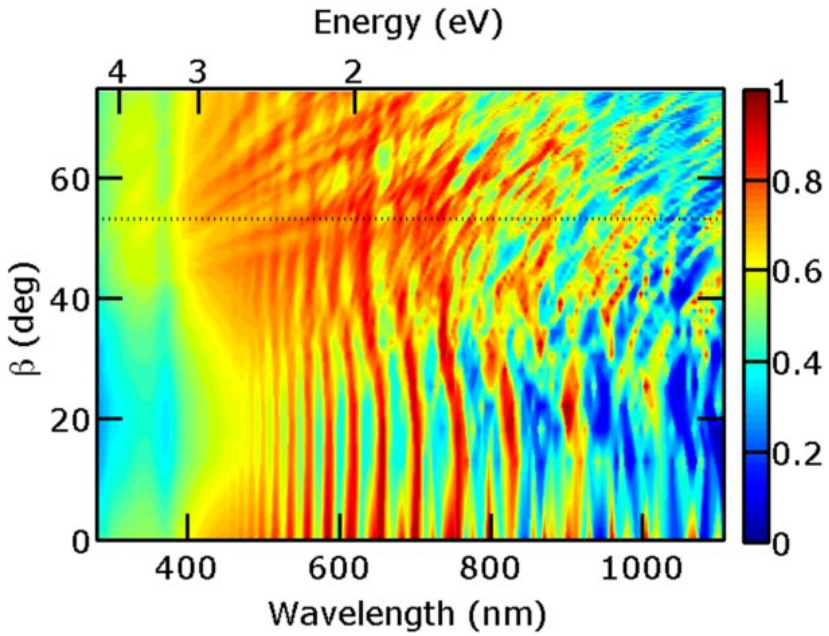

Figure 4: Tilted nanowire array simulation results.Absorption as a function of wavelength and nanowire tilt β. The absorption shown is the average of the two polarizations.

efficiency decreases when compared to the vertical nanowire arrays. The minimum ultimate efficiency is 24.0% at $\beta = 18°$. Figure 5 plots the absorption spectra of the vertical nanowire array ($\beta = 0°$) and this tilted nanowire array. The absorption spectra of the $\beta = 18°$ tilted nanowire array closely resembles that of the vertical nanowire array, but the magnitude of the various absorption resonances are lower. For small tilt angles, the ultimate efficiency decreases because the excitation efficiencies of the HE_{1m} modes decrease. However, as the nanowire is tilted, additional modes besides the HE_{1m} modes may be excited. The overall absorption for tilted nanowires is thus increased compared to tilted nanowires for higher tilt angles. The tilted nanowires exhibit improved performance over vertical nanowires over the range of $\beta = 38$ to $72°$.

Figure 6 plots the absorption spectra of the ideal double pass thin film, vertical nanowire array, and best tilted nanowire array. Table 1 lists the fraction of photons absorbed in different regions of the solar spectrum for these three. The infrared region (above the Si

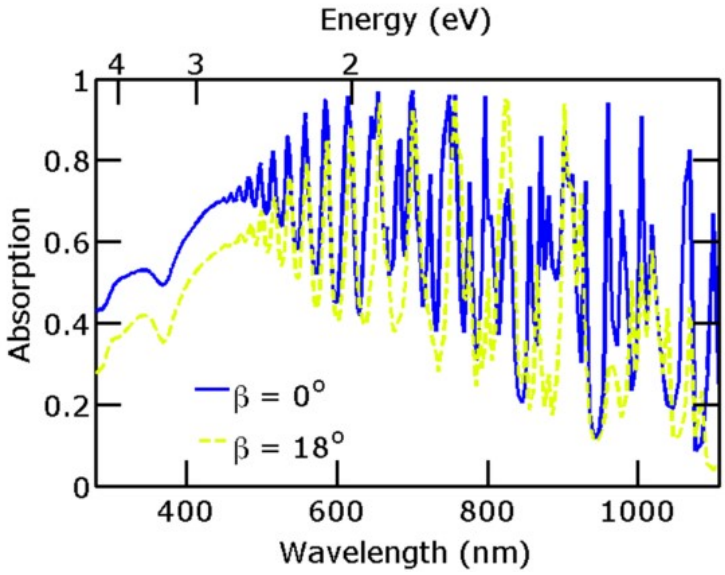

Figure 5: Tilted nanowire array simulation results. The absorption spectra of the vertical nanowire array ($\beta = 0°$) and worst tilted nanowire array ($\beta = 18°$).

band gap) is from 1.12 to 1.67 eV (1100 to 740 nm), the visible region is from 1.67 to 3.1 eV (740 to 400 nm), and the ultraviolet region is from 3.1 to 4.4 eV (400 to 280 nm). The total absorption shown only includes the range above the c-Si band gap energy from 1.12 to 4.4 eV (1100 to 280 nm). Vertical nanowire arrays have improved absorption in the lower energy regime (infrared and visible region) compared with the ideal double pass silicon thin film due to light trapping. Tilted nanowire arrays improve the light trapping performance even more by increasing absorption across the infrared, visible, and ultraviolet regions compared to the vertical nanowire arrays.

The performance of these three different structures for solar cells are compared in Table 2. The total solar absorption, ultimate efficiency, and short circuit current density are all shown in this Table. The total solar absorption shown in this table is over the entire solar spectrum and not just over energies above the silicon band gap as shown in Table 1. The ultimate efficiency of the vertical nanowire arrays is 29.7%, a 66.2% improvement over the 17.9% exhibited by the ideal double pass thin film with the equivalent amount of material.

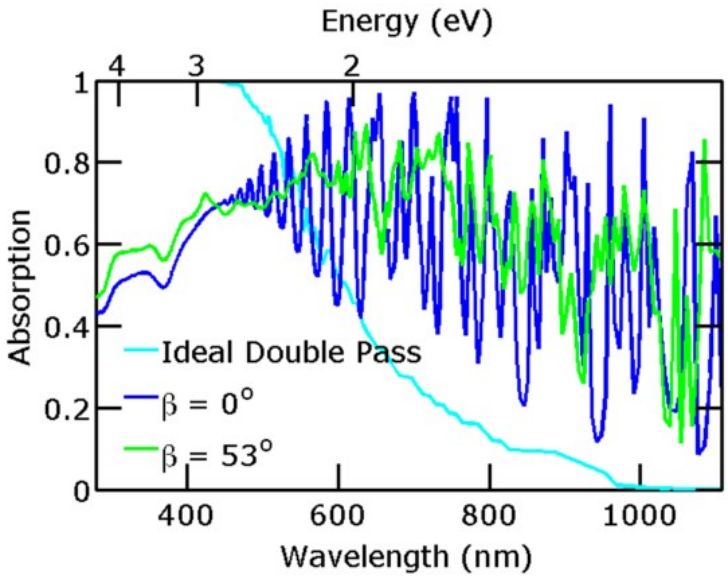

Figure 6: Tilted nanowire array simulation results. The absorption spectra of the ideal double pass thin film, vertical nanowire array ($\beta = 0°$), and best tilted nanowire array ($\beta = 53°$).

The ultimate efficiency of the tilted nanowires arrays is 32.2%, or an improvement of 8.6% compared to vertical nanowire arrays or 80.4% over the ideal double pass thin film. These simulations demonstrate the potential of tilted nanowire arrays to improve the performance of vertical nanowire arrays under normal incidence.

We further studied the performance of the nanowire arrays under oblique incidence. The source was varied from $\theta = -90°$ to $90°$ for the best vertical nanowire array ($a = 600$ nm, $d = 560$ nm, and $\beta = 0°$) and the best tilted nanowire array ($a = 600$ nm, $d = 560$ nm, and $\beta = 53°$). The incidence angle θ is with respect to the negative z direction as shown in the Figure 1 schematic. Figure 7 shows results for transverse electric (TE) waves, which are are linearly polarized transverse to the plane of incidence, and transverse magnetic (TM) waves, which have linear polarization so that the magnetic field is purely transverse. Our results at an incidence angle of $\theta = 0°$ are slightly different from that above due to the use of different boundary conditions. The performance of the vertical nanowire arrays is symmetric

Table 1: Absorption (%) in different spectral regions. The infrared and total solar regions are calculated for those portions that are above the Si band gap ($E > 1.12$ eV).

Spectrum	**IR**	**Vis**	**UV**	**Total**
Ideal Double Pass	6.0	59.4	100.0	36.4
Vertical Nanowire Array	41.8	70.5	57.2	60.5
Tilted Nanowire Array	46.7	74.7	60.0	65.7

Table 2: The total solar absorption, A_{sol} (%), short circuit current density J_{sc} (mA/cm^2), and the ultimate efficiency η (%).

	$\boldsymbol{A_{sol}}$	$\boldsymbol{J_{sc}}$	$\boldsymbol{\eta}$
Ideal Double Pass	23.1	15.9	17.9
Vertical Nanowire Array	38.4	26.5	29.7
Tilted Nanowire Array	41.7	28.8	32.2

with respect to positive and negative incidence angles. While freestanding vertical nanowire arrays have better performance under TM-polarized incident light than TE [93, 87], our results indicate that vertical nanowire arrays on a perfect back reflector have the opposite trend where the ultimate efficiency is higher for TE polarization than TM polarization. The increased absorption under TM-polarized incident light in freestanding vertical nanowires is due to reduced transmission [108], whereas our system has no transmission due to the perfect back reflector.

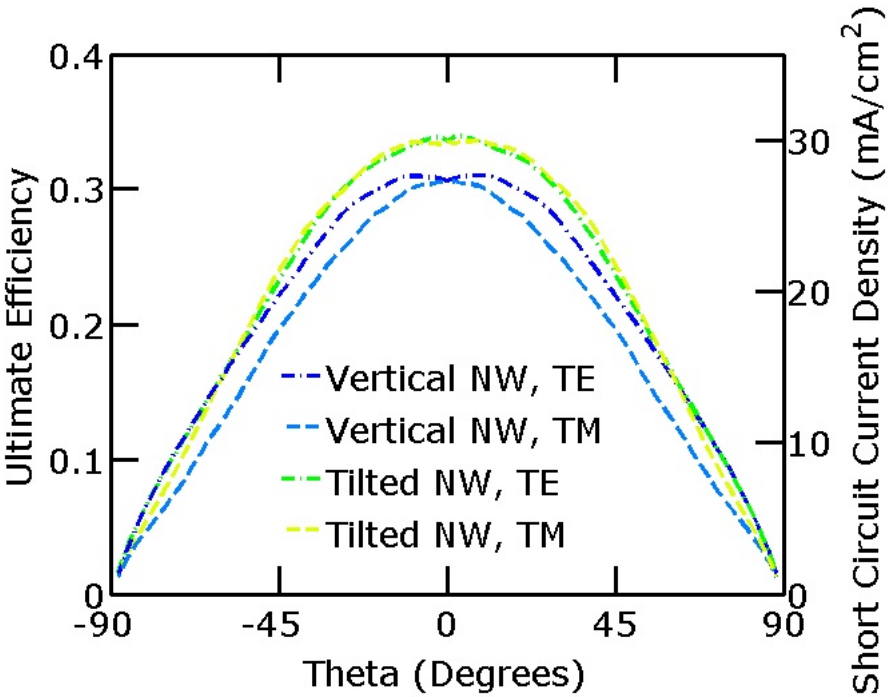

Figure 7: Ultimate efficiency of vertical nanowire and tilted nanowire arrays as a function of incidence angle θ. The TE polarization results for the tilted nanowire arrays are the average of the light polarized along the x-axis and the y-axis. Likewise, the TM polarization results for the tilted nanowire arrays are the average of the magnetic field along the x-axis and the y-axis. The tilted nanowire arrays consistently perform better than the vertical nanowire arrays for incidence angles under about 60°.

In our simulations of tilted nanowires, the performance is symmetric with respect to positive and negative incidence angles for TE waves with electric field along the x-axis and TM waves with magnetic field along the y-axis. However, this symmetry is broken for TE-incidence with electric field along the y-axis and TM-incidence with magnetic field along the x-axis. The results shown for the tilted nanowire arrays are the average of the two orthogonal polarizations. The performance of the tilted nanowires is slightly better under positive incidence angles versus negative incidence angles, where the Poynting vector is closer to along the axis of the nanowire. In addition, we note that the performance of the tilted nanowires is consistently higher than that of the vertical nanowire arrays for incidence angles under about 60°. For high angles of incidence, the performance of the vertical and tilted nanowires converge for both TE-incidence and TM-incidence.

2.4 Conclusion

We have performed a comparative study of the optical performances of tilted silicon nanowire arrays on a perfectly electric conductor for photovoltaic applications using the finite difference time domain method. Our results show that the absorption enhancement in vertical nanowire arrays over silicon thin films can be further improved through tilted nanowires. Optimized vertical nanowire arrays with a height of 1000 nm have a 66.2% ultimate efficiency improvement over an ideal double pass thin film of the equivalent amount of material. Tilted nanowire arrays, with the same amount of material, exhibit improved performance over vertical nanowire arrays over a broad range of tilt angles (from 38 to 72°). The optimum tilt of 53° has an improvement of 8.6% over that of the vertical nanowire arrays and 80.4% of the ideal double pass thin film. Tilted nanowire arrays exhibit improved absorption over the infrared, visible, and ultraviolet regime compared with vertical nanowires since the tilt removes symmetry requirements on the resonance modes in the nanowires. We also observed that tilted nanowire arrays have improved performance over vertical nanowire array over a large range of incidence angles (under about 60°).

3.0 Critical Heat Flux Enhancement in Pool Boiling through Increased Rewetting on Nanopillar Array Surfaces

3.1 Introduction

Boiling is a central phenomenon in technological and industrial applications as diverse as thermal management in electronics, power generation and chemical processing [109, 110, 111]. Pool boiling is the process, when a stagnant pool of liquid is heated and boiling occurs in the liquid at the bottom of the bulk liquid pool. Four different regimes can be seen in the pool boiling curve: natural convection, nucleate boiling, transition boiling, and film boiling. Nucleate boiling regime is important, as high heat flux can be achieved without damaging the substrate. The enhancement of the energy efficiency during boiling applications can be done by increasing the critical heat flux (CHF), the highest heat flux a boiling substrate can achieve. Increasing the CHF also reduces the operational risks by avoiding the notorious "boiling crisis," a major cause of burnouts in boilers or heat exchanging devices [112]. The boiling crisis occurs because of excessive vaporisation of liquid on a boiling substrate. A vapor layer is formed which severely impedes heat transfer through the substrate and a sudden jump in the surface temperature is observed. Subsequently the substrate of the boiling equipment is damaged irreversibly. The temperature T_c at which CHF occurs, known as the critical temperature, therefore is directly connected to the boiling crisis; a boiling system operating at temperature higher than T_c inevitably drifts towards the boiling crisis. In order to enhance the boiling performance and to avoid the boiling crisis both CHF and critical temperature T_c need to be increased.

Many studies have been conducted to understand the mechanism of nucleate boiling. With increasing surface temperature, CHF is the upper bound of heat flux in the nucleate boiling regime before the boiling crisis occurs [113]. Different microscale models have been proposed to explain nucleate boiling heat transfer mechanisms [114]. Latent heat transfer is dominant compared to convective heat transfer in the nucleate boiling regime. Surface roughness ranging from nano- to micro-scales [115], and wettability [116] have been reported

as important parameters which affect the heat flux in the nucleate boiling regime. To increase the critical heat flux researchers have followed two major approaches: fluid modification and surface treatment. However, fluid modification approach uses additives [117, 118] or nanoparticles [119] and puts constraints on fluid selection and operating conditions of the boiling system [120]. The surface treatment approach includes either treatments to enhance surface wettability [121, 122], or morphological alteration of the substrate. Incorporation of porous coatings [123, 124], artificial fins [125, 126, 127] and nano/microstructures [120, 128] are some of the examples of morphological alteration. Although numerous surface modification methods have been found to increase CHF, in particular those utilising nano/microstructures, the roles of surface structures at different length scales in changing the heat flux and the critical temperature remain elusive. Although it has been suggested that nanoscale structures may intensify the wetting velocity, which is a crucial factor leading to CHF enhancement [122, 129], the relation between a systematic change in nanoscale structures, wetting velocity and CHF has not been established. Moreover, little effort has been made to relate surface wettability or nanoscale structures to the change in the critical temperature T_c .

In this study, we investigate the boiling phenomenon of FC-72 on nanostructured surfaces. Fluorinert liquid FC-72 is an ideal coolant liquid commonly used in various heat management applications and has a low boiling point (56°C). We show that modifying the surface morphology at nanoscales leads to significant enhancement in the boiling performance, including both the critical heat flux and the critical temperature. By using nanopillars with systematically varying heights on silicon substrates, we demonstrate scalable boiling enhancement with increasing height of nanopillars. The enhancement in both the CHF and the critical temperature results from an intensified rewetting process which increases with the height of nanopillars.

3.2 Methods

3.2.1 Fabrication of Nanopillar Substrates.

The nanopillar silicon substrates are obtained by Inductively Coupled Plasma Reactive Ion Etching (ICPRIE). The process flow is shown in Figure 8. The fabrication process consists of three steps, (1) manufacture of the etching mask, (2) etching the underlying silicon by ICPRIE, and (3) removal of etching mask. Polystyrene (PS) nanospheres are utilised to generate the etching mask.

First, a monolayer of nanopheres with the diameter of 800 nm are self-assembled in the air-

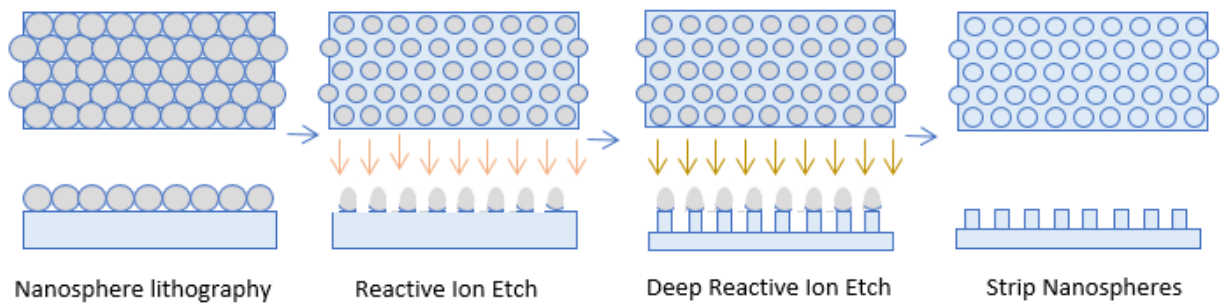

Figure 8: Schematic depiction of the fabrication process.

water interface [130, 131, 132]. Subsequently the monolayer is transferred to a P-type boron-doped (100) silicon substrate, which has been cleaned with acetone, methanol, isopropanol and then dried with nitrogen gas. After the substrate is dried in air at room temperature, Reactive Ion Etching (RIE) with oxygen is applied to reduce the diameter of nanopheres to the required size (≈440 nm). During the RIE process the pressure was set at 25 mTorr and the RF power was set at 25 W. The flow rate of oxygen was 25 sccm, which yielded an etch rate of 80 nm per minute. The duraion of the RIE process was 270 seconds. By varying the RIE duration, it is possible to vary the diameters of the mask and hence that of the nanowires.

Table 3: Reactive ion etching parameters

Gas	**Flow Rate** (sccm)	**Pressure** (mTorr)	**Power** (Watts)	**Duration** (mintues)	**Etch Rate** (nm/min)
Oxygen	25	25	25	variable	80

Table 4: Parameters of fabricated nanopillar substrates.

Etch duration (minute)	**Top radius** d_t (nm)	**Bottom radius** d_b (nm)	**Height** h (nm)	**Roughness** r
1	440	440	260	1.7
2	440	440	390	2.7
4	440	440	690	2
6.5	200	405	1390	3.2

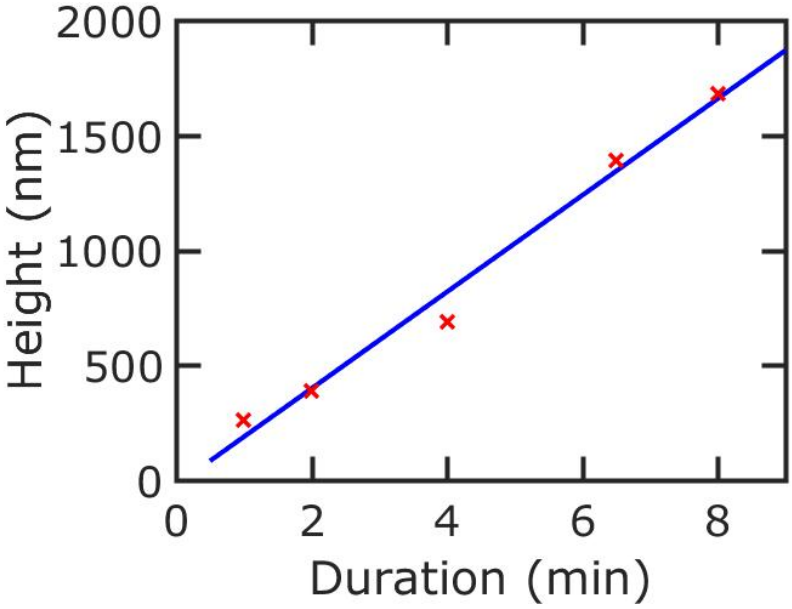

Figure 9: Nanopillar height vs etch duration during pseudo bosch process.

After the etching mask is manufactured, ICPRIE is used to etch the silicon substrate to fabricate silicon nanopillars with desired dimensions. Mixed mode of operation is used to fabricate the samples instead of the commonly used bosch process. The difference between the mixed mode and the bosch process is that during the bosch process there are two different steps that works during each cycle. First the etching gas is flown and then the passivation gas is flown. The gases are flown separately. The purpose of using the passivation gas is to is to make the sidewalls smooth. However, due to the separation of etching and passivation step the nanowires has the spiral structures. The number of cycles of these steps determine the length of the nanowires. On the other hand during the mixed mode process, which has also been referred as the pseudo bosch etching method, both the passivation and etching gases are flown together. The etch rate is comparatively slower than the bosch process, but the vertical sidewalls of the nanowires are smooth and the spiral structures are avoided. SF_6 is used for etching purpose and C_4F_8 is used for passivation purpose. The ratio of the etch and passivation gas is varied to find the optimized ratio for fabricating silicon nanopillars.

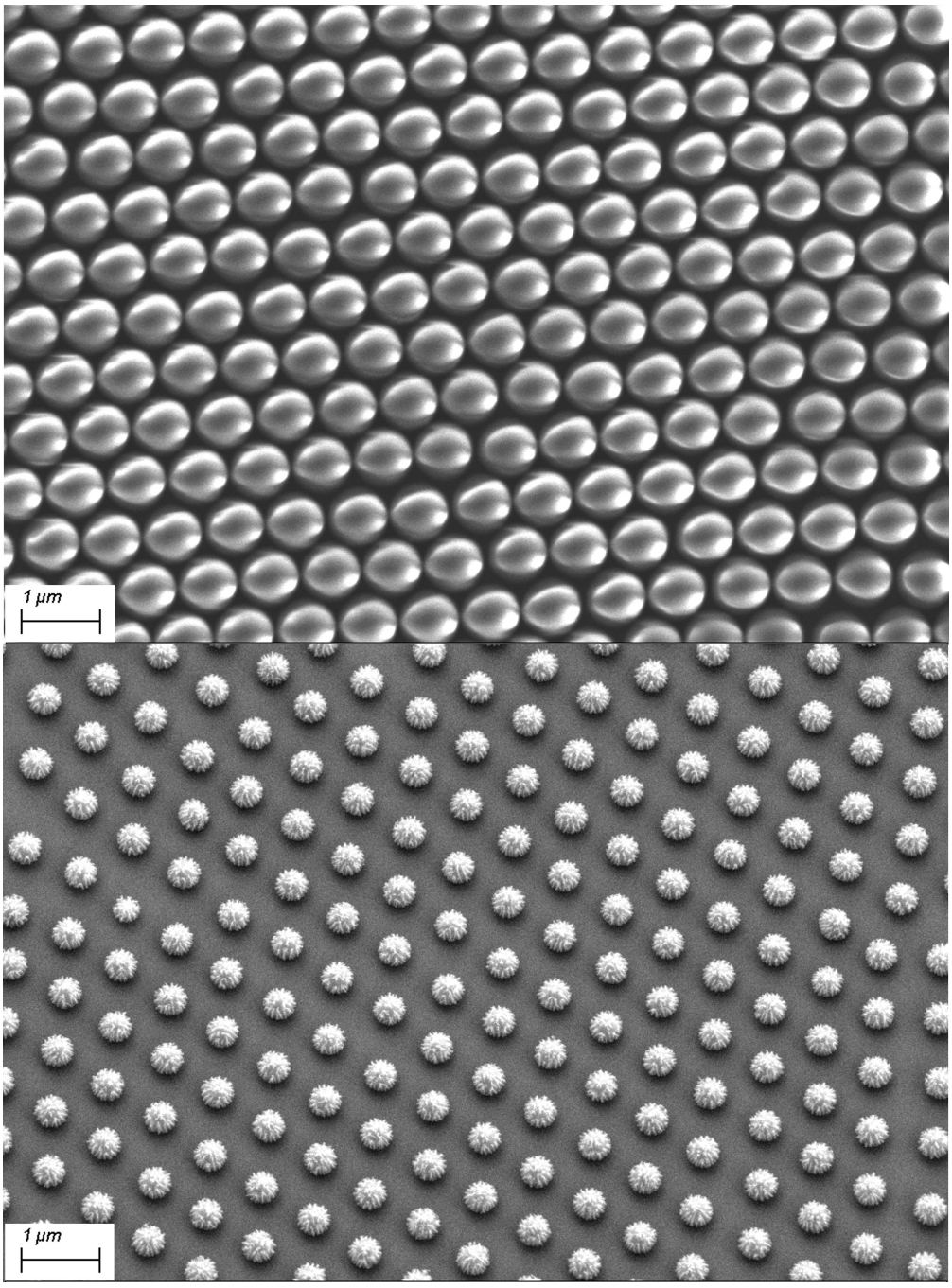

Figure 10: SEM images of Silicon substrate a) After Nanosphere Lithograpy, b) after Reactive Ion Etching, c) after Deep Reactive Ion Etching and ultrasonication.

Three different gas ratios were used to evaluate the fabricated nanopillars, while other process parameters were kept constant. Ratio of SF_6 and C_4F_8 was 33:57, 33:82, 33:110 for three different batches of samples. Based on the SEM images of these samples, the optimal ratio of SF_6 and C_4F_8 is found to be 33:82 and is used for subsequent runs. Different height of nanopillars are obtained by varying the duration of this step. The ICP power, and forward power were 600 Watts and 20 Watts respectively.

It should be noted that when the time duration is longer than 5 minutes the PS mask is impacted and the nanopillar base diameter is different from the etching mask. When the etching is completed, the PS mask is be removed by ultrasonication in acetone for 5 minutes.

3.2.2 Boiling Experiment.

Initially, fabricated silicon nanopillar substrates were sent to our collaborators at the Nanyang Technological University, Singapore for boiling experiments. Based on their feedback a second batch of samples with optimized parameters were prepared and sent to them again. Details of those samples were provided in the previous section and those samples were used for the boiling experiments. The experimental setup used to measure the heat flux through different substrates consisted of three sections: heating, testing and condensation. In the heating section, a cartridge heater embedded in a cylindrical copper rod was used to generate heat. A Teflon holder was used to insulate the copper rod from the surrounding environment. In the testing section, a boiling substrate is placed between the copper rod and a glass cuvette. The test substrate was cleaned with organics (ethanol and acetone) in a ultrasonic bath and rinsed with distilled water before each experiment. The cuvette was filled with degassed FC-72 as a working liquid and was enclosed by a stainless steel container. Hot water of temperature $55.5 \pm 0.5\,^{\circ}C$ was circulated in the gap between the cuvette and the container to keep the temperature of the working liquid close to the boiling point. Two glass windows on two opposite sides of the container enabled the optical recording during the boiling experiement. A condenser was used to collect vapor generated from the working liquid. The cooling power of the condenser was adjusted to keep the vapor pressure inside the cuvette at atmospheric pressure.

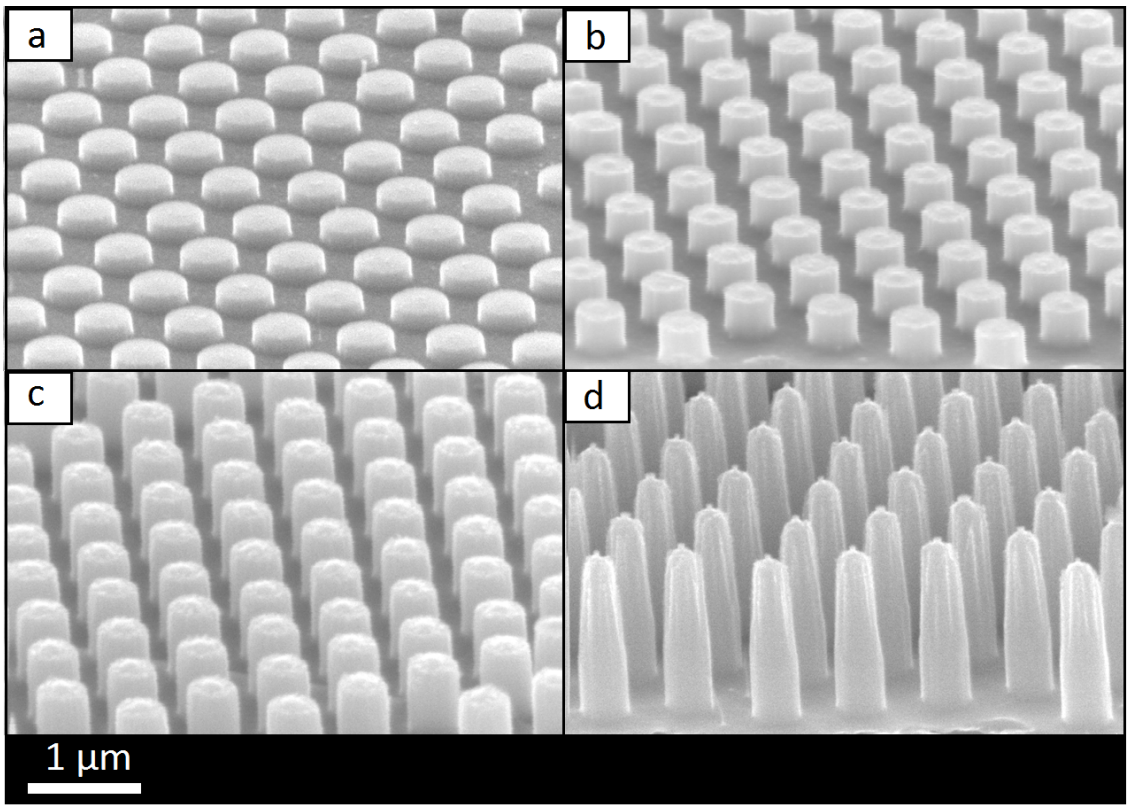

Figure 11: SEM images of fabricated samples and corresponding surface roughnesses r.

The vapor pressure was measured by pressure transducer (Gefran) and maintained at atmospheric pressure by adjusting the cooling power of a Peltier module. The temperature was measured by K-type thermocouples and the boiling process was recorded by a high speed camera (SA-5, Photon). Three thermocouples were distributed along the asymmetrical axis of the copper cylinder. The temperatures measured by these thermocouples were used to calculate the heat flux q through the test substrate and the surface temperature T. The heat flux in the vertical direction was approximated with the assumption that the rate of heat loss to the side was constant [133, 134]. Thus the heat flux through the substrate was estimated as:

$$q = 0.5k_c \left(4T_2 - T_1 - 3T_3\right) \Delta x_c^{-1}. \tag{3.1}$$

where k_c was the thermal conductivity of copper, T_1, T_2, T_3 were obtained from the thermocouples in the copper rod, and Δx_c was the distance between them. There were three layers between the top thermocouple and the top surface: a copper layer (7 mm), a thermal glue layer ($\approx 10\,\mu$m) and the silicon substrate ($500\,\mu$m). The surface temperature T of the test substrate was then estimated by the one-dimensional heat conduction equation:

$$T = T_3 - q\left(\Delta x_c {k_c}^{-1} + \Delta x_g k_g^{-1} + \Delta x_s k_s^{-1}\right), \tag{3.2}$$

where $\Delta x_c/k_c$, $\Delta x_g/k_g$ and $\Delta x_s/k_s$ denoted the heat resistance of copper, thermal glue, and silicon substrate respectively. For each tested substrate, the heat flux q and the corresponding superheat $\Delta T = T - T_b$ were measured when the system was in the steady state and with temperature steps of 5 K. The experimental uncertainty was obtained by repeating the experiment three times.

3.2.3 Experimental Validation.

The measurement procedure and analysis were validated by comparing the heat transfer data obtained on the smooth substrate to the well-known dataset obtained by Ujereh *et al.* [135], as well as to classical model, including the one for nucleate boiling heat transfer by Rohsenow [136] and the one for critical heat flux by Zuber [137] (Figure 12).

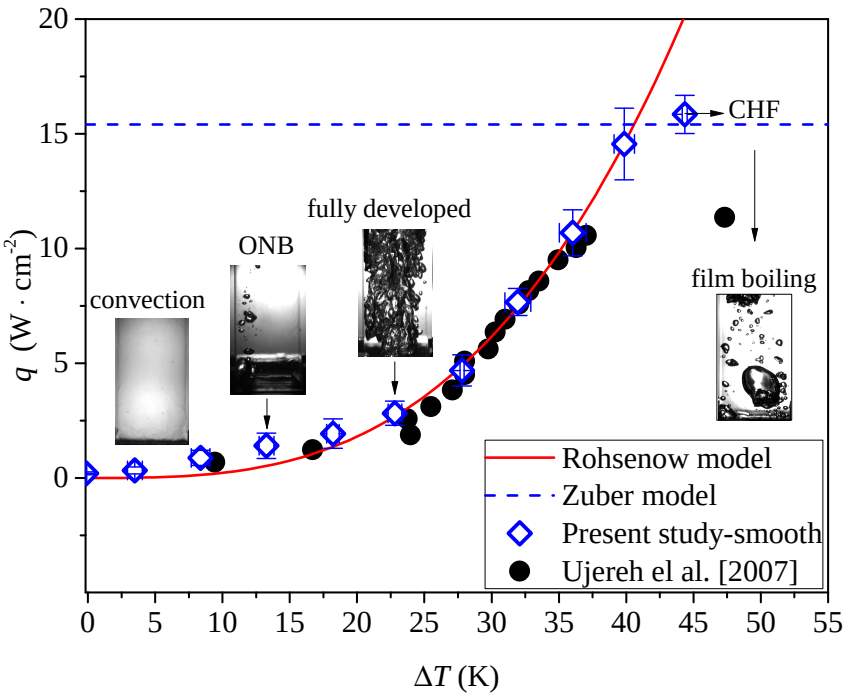

Figure 12: Comparison between the boiling curve measured on silicon smooth surface in the present study and the one obtained by Ujereh *et al.* [135]. The solid line represents the heat flux predicted by Rohsenow model, and the dashed line represent the critical heat flux predicted by Zuber model [137].

3.3 Results and Discussion

3.3.1 Enhancement in Critical Heat Flux and Nucleate Boiling Limit.

We systematically varied the height l of nanopillars fabricated on silicon substrates (Figure 11) and showed that increasing l resulted in the enhancement of both the critical heat flux (CHF) and the upper limiting temperature of nucleating boiling. The nanopillars were fabricated by an inductively coupled plasma reactive ion etching (ICPRIE) process that directly modified the surface. No coating layers were added which could induce additional thermal resistance to the substrate [138]. Typically, the quantity used for characterising the upper limiting temperature is either the CHF temperature T_c, or the Leidenfrost temperature T_L. The nanopillars were arranged in a hexagonal lattice with the lattice pitch $p \approx 800\,\text{nm}$, the base diameter of nanopillars $d_b \approx 440\,\text{nm}$, and l being varied from 260 nm to 1390 nm. The differences in boiling behavior and performance between these substrates therefore are attributed to variation in l, or alternatively the surface roughness $r = A_t/A_p$. Here A_t denotes the total surface area due to the presence of the nanopillars, and A_p is the projected boiling area. In our experiment, r ranged from 1 for the smooth silicon substrate to 3.2 for the longest nanopillar substrate with $l = 1390\,\text{nm}$. To qualitatively evaluate the effect of the nanopillars on boiling, we first compared the boiling behavior of the smooth substrate and the nanopillar substrate with $r = 3.2$ at several surface temperatures T (Figure 13). Although the onset of boiling occured at $T \approx 69\,^\circ\text{C}$ for both substrates, the size of bubbles generated on the smooth substrate varied much more broadly than that on the nanopillar substrate. The difference in bubble dynamics became even more contrasting at higher temperature. The bubbles on the smooth substrate tended to merge and create either large bubbles or vapor columns starting from the substrate. But those generated on the nanopillar substrate had much lesser tendency to merge and it seemed that they were more uniform in size. We note that it is unlikely for bubbles to coalesce after their detachment from the substrate due to liquid inertia and surface tension, thus the coalescence process mainly occurred between consecutive bubbles generated from the same nucleation site before detachment. This strongly suggests that resistance to coalescence, as well as the uniform size of bubbles

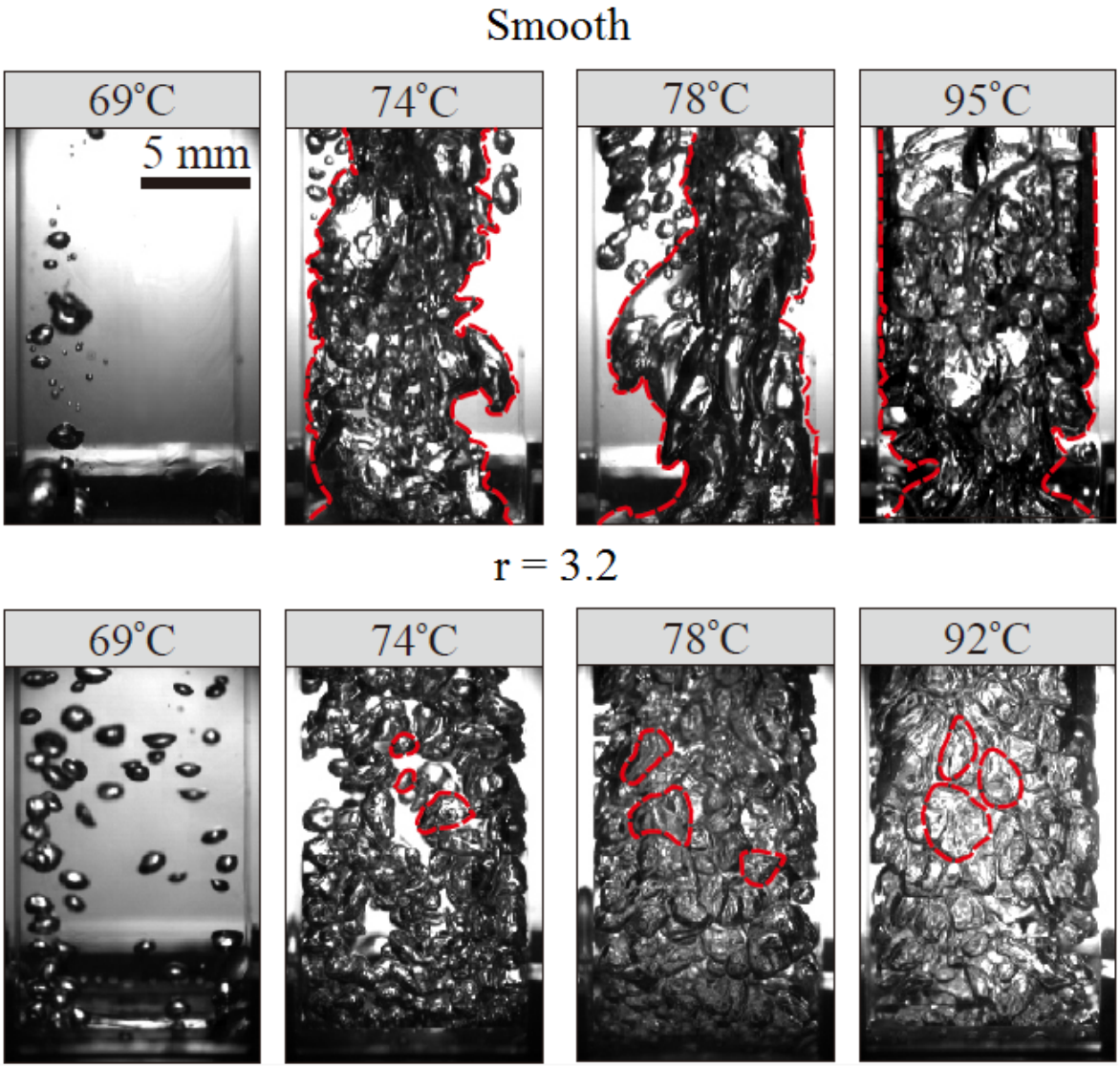

Figure 13: Representative snapshots showing boiling phenomenon on the smooth substrate (top panel) and the nanopillar substrate with $l = 1390\,\mathrm{nm}$ (bottom panel) at several surface temperatures T. While the smooth surface produces vapor bubbles which have tendency to coalesce (e.g., at $T = 74\,^{\circ}\mathrm{C}$) and form vapor columns (e.g., at $T = 78\,^{\circ}\mathrm{C}$), the nanopillar substrate produce bubbles which have a narrow size distribution tend to evolve separately without merging. The vapor column and bubbles are highlighted by red dashed lines.

generated from the nanopillar substrate result from an effective rewetting process, which facilitates bubble detachment from the surface. We hypothesise that deviation in boiling behavior of nanopillar substrates from the smooth substrate, therefore, originates from the nanopillar-induced enhancement in the rewetting process.

We now quantify the effect of nanopillars on the boiling performance by measuring the heat flux q for each substrate as a function of the superheat $\Delta T = T - T_b$, where $T_b = 56\,^{\circ}\mathrm{C}$ is the boiling temperature of FC-72 at atmospheric pressure. The dependence of q on ΔT for the smooth and all the nanopillar substrates is shown in Figure 14a. Starting from $\Delta T = 0$, q first gradually increased due to natural convection until it reached the onset of nucleate boiling ($\Delta T \approx 30\,\mathrm{K}$ for all tested substrates). In this natural convection regime, the presence of nanopillars had negligible effect on the heat flux, as the nanopillars were much smaller than the thermal boundary layer thickness. Here, the boundary layer thickness was roughly $57\mu m$, estimated using the ratio between the natural convection heat transfer coefficient and the thermal conductivity of FC-72 [139].

As ΔT increased past the onset of nucleate boiling, the heat flux on nanopillar substrates, denoted as q^n, deviated substantially from that of the smooth substrate. In particular, q^n after the system transitioned into the nucleate boiling regime was achieved at much lower superheat compared to that when system was still in the natural convection regime (inset of Figure 14a). For instance, for the substrate with $r = 2, q = 3.3W.cm^2$ was achieved at $\Delta T \approx 16\,\mathrm{K}$ when the system was in the nucleate boiling regime, whereas a slight increase in heat flux, $r = 2, q \approx 3.5W.cm^2$, was achieved at much higher superheat$\Delta T \approx 33\,\mathrm{K}$ in the natural convection regime. On the smooth substrate, however, the heat flux increased smoothly as the system transitioned into the nucleate boiling regime. The presence of nanopillars caused a substantial jump in heat flux as soon as the system transitioned to the nucleate boiling regime because the heat transfer mechanism was more efficient for the nanopillar substrates. The sudden discontinuity in the boiling curve was seen because of the homogeneous spread of nucleation sites, high generation frequency and narrow size distribution of bubbles on nanopillar substrates. With the superheat increasing beyond the onset of nucleate boiling, bubbles were generated with higher frequency and larger size, intensifying forced convection in the bulk liquid and subsequently enhancing the heat flux q. For each substrate, q increased

to the CHF q_c at the critical temperature T_c, beyond which it dropped sharply due to excessive vapor generation and lack of replenishing liquid to the substrate. The heat flux reached its minimum value at the so-called Leidenfrost temperature T_L, or the upper limit of nucleate boiling. The sudden drop in heat flux at T_L often triggers drastic spike in surface temperature causing the notorious "burn-out" in boiling applications. Thus designing heat-dissipating substrates with high T_L is as practically important as enhancing the critical heat flux.

We observed considerable enhancement in both q_c and T_L on nanopillar substrates. The dependences of q_c and T_L on the surface roughness r is shown in Figure 14b. Both q_c and T_L increased monotonically with the increase of r (or equivalently with pillar height l). Compared to the smooth substrate ($r = 1$), q_c and T_L on the nanopillar substrate with $r = 3.2$ increased $\approx 50\%$ and $\approx 25\,^{\circ}\mathrm{C}$, respectively. The enhancement in both q_c and T_L is a remarkable feature of the nanopillar substrates as opposed to those fabricated with larger scale structures. It was observed that micro-structures only enhance the heat flux without increasing the Leidenfrost temperature; typically T_L decreases with increasing height of microstructures [140]. Separate investigations on hierarchical substrates, i.e.,microstructured surfaces covered with nanograss, reported enhancement in either the Leidenfrost temperature [141, 142, 143], or the heat flux [120, 142, 144, 145, 146, 147, 148, 149].

3.3.2 Mechanism of Heat Transfer Enhancement on Nanopillar Substrates.

To understand how the nanopillars enhanced q_c and T_L, we investigated the heat transfer mechanism on nanopillar substrates. Based on the qualitative observations of the differences in bubble generation between the nanopillar substrates and the smooth one, we postulated that the major contributing factor leading to the observed change in q_c and T_L is the nanopillar-induced rewetting process. For hierarchical structured surfaces, i.e., microstructures covered by nano-grass, enhancement in q_c was observed. However it was attributed to the wicking process. More liquid was brought to the surface due to the enhancement in

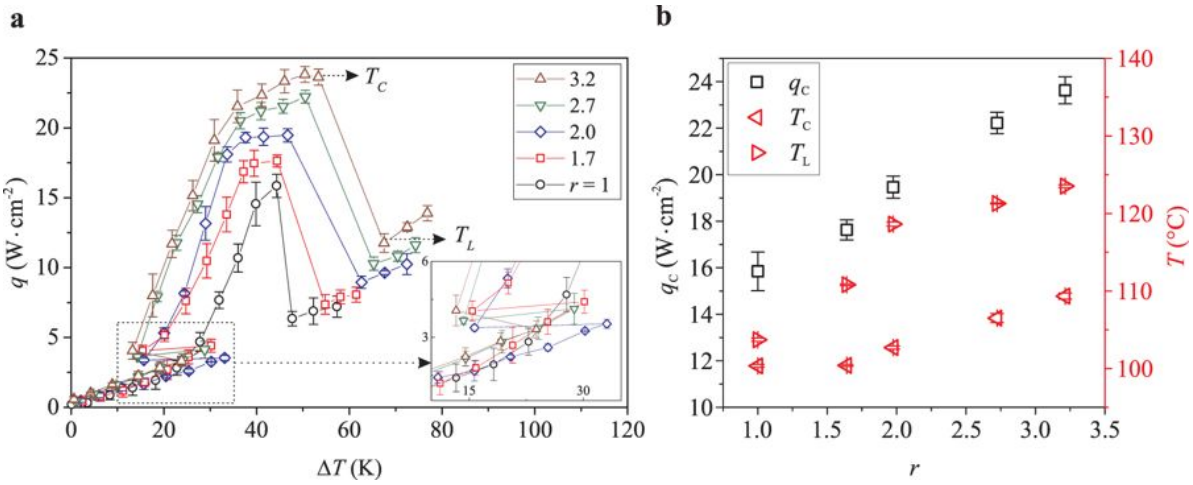

Figure 14: (a) Heat flux q versus wall superheat ΔT for smooth and nanopillar substrates. (b) Dependence of critical heat flux q_c (open squares), CHF temperature T_c (left-pointing triangles), and Leidenfrost temperature T_L (right-pointing triangles) on surface roughness r.

volume of liquid wicking through the microstructures, which resulted in an increase in heat flux by latent heat of evaporation. Because of the tremendous viscous stress induced in flows confined in such small length scales between pillars, [120] the wicking process is not possible for nanopillar substrates.

We focused on the advancing contact line of liquid to study the nanopillar-induced rewetting process and its effect on the enhancement of heat transfer. As shown in Figure 15, the rewetting process of vapor bubbles and the spreading process of liquid are similar. Taking advantage of this similarity, the dynamics of the advancing contact line can be studied separately in the case of spreading liquid on nanopillar substrates [122, 129]. The rewetting process has been studied extensively [120], which revealed contributing factors such as surface-induced capillary force [120], hydrostatic and hydrodynamic forces [129], reshaping effects [150], vaporisation [151]. For the nanopillar substrates, we investigated the spreading of liquid from a capillary tip onto heated substrates (Figure 15a) and determined the dominant effects responsible for the heat transfer. The surface temperature was varied. The temperature dependence of the apparent spreading velocity v_s on each nanopillar substrate was determined by tracking the three-phase contact-line (TCL), when the liquid was spread-

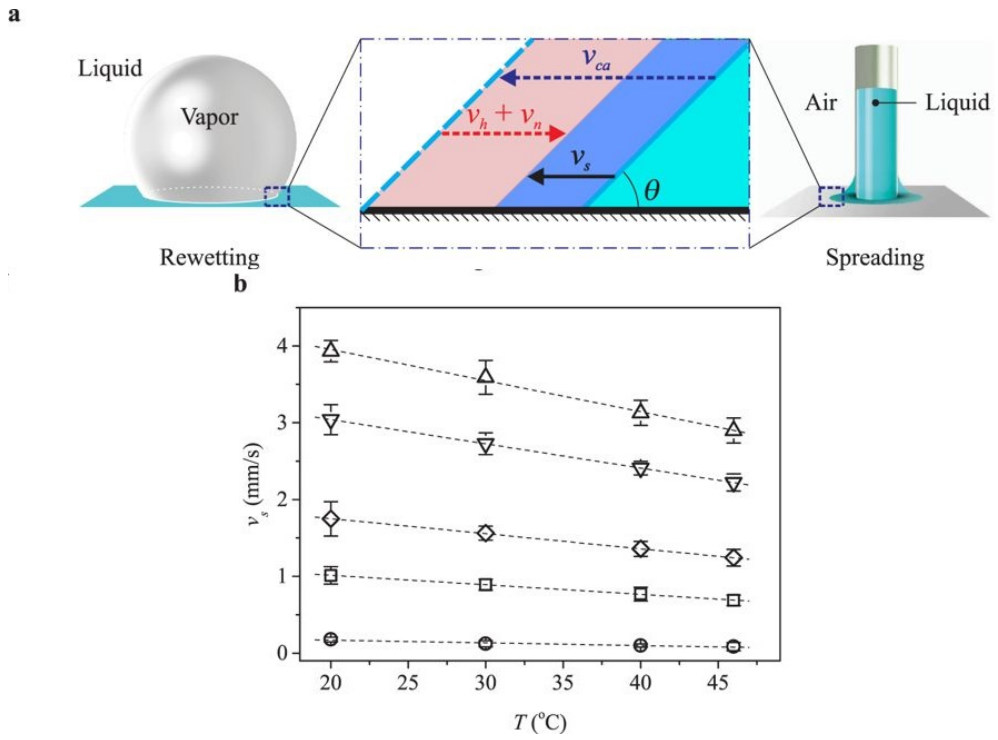

Figure 15: (a) Schematics showing that the rewetting process in pool boiling (left panel) is similar to the spreading process (right panel), in particular in the motion of liquid at the three-phase contact line (middle panel). (b) Apparent spreading velocity v_s of FC-72 on different substrates over a range of temperature from 20 °C to 46 °C.

ing. The surface temperature can be varied from room temperature $T_r = 20\,^{\circ}\mathrm{C}$ up to $46\,^{\circ}\mathrm{C}$ without causing the liquid to boil. Although the displacement of the TCL results from various coupled effects, we simplified the analysis by decomposing v_s into several independent components (Figure 15b):

$$v_s = v_{ca} - v_n - v_h, \tag{3.3}$$

where the component v_{ca} is caused by capillary force on the substrate and therefore is a function of the surface roughness r only. The component v_h represents the reduction in spreading velocity as liquid absorbs heat from the surface and evaporates. Thus at room temperature $v_h = 0$, as there is no heat transferred from the surface to the liquid. The velocity component v_n represents the reduction in spreading velocity due to natural evaporation of liquid. In the case of boiling, it vanishes as bubbles generated during boiling of liquid are filled only with saturated vapor. Here, we neglected contributions to TCL displacement from hydrostatic pressure of the liquid column, and from capillary pressure at the upper liquid surface in the tube due to the small gap between the capillary tube and the substrate.

We postulate that nanopillar-induced enhancement in wetting increases the heat flux on nanopillar substrates. This is suggested from the linear correlation between the critical heat flux of different substrates and the spreading velocity v_s measured on respective substrates at surface temperature $T = 20\,^{\circ}\mathrm{C}$. In other words, the presence of nanopillars intensifies the rewetting process, leading to an added amount of liquid brought to and subsequently evaporated from the surface. Among the contributing components to the apparent spreading velocity, v_{ca} inherits the effect of r on capillary wetting, thus has a direct relation to the enhanced rewetting process. In addition, as the surface temperature for spreading liquid was set lower than the liquid's boiling temperature, we assume that with constant surface temperature, v_n remains fixed for all the substrates, i.e., $v_n^n = v_n^s$, where the superscripts n and s respectively indicate quantities of the nanopillar substrates and the smooth substrate. We recall that v_{ca} is independent of T and $v_h = 0$ at room temperature. As a result, at room temperature T_r, the spreading velocity difference $\delta v_s(T_r) = v_s^n(T_r) - v_s^s(T_r)$ between a nanopillar substrate and a smooth substrate only depends on the change in capillary velocity between the two substrates $\delta v_{ca} = v_{ca}^n - v_{ca}^s$. Thus, δv_{ca} can be estimated as $\delta v_{ca} \approx \delta v_s(T_r)$. We measure the spreading velocity v_s for all nanopillar substrates and the smooth substrate

(see Figure 15b). The spreading velocity increase $\delta v_s(T_r)$ is calculated for each nanopillar substrate to obtain δv_{ca}. The spreading velocity increases with increasing nanowire height due to the increasing energetic favorability of wetted nanowire surfaces of increasing height. The energy of the different dry nanopillar substrates is approximately the same. However, the energy of different wetted nanopillar substrates decreases with increasing height due to the the larger interface between the liquid and solid nanopillar array. This energy difference drives the spreading of the FC-72, and thus, the spreading velocity increases with increasing nanopillar height.

We note that the heat flux at CHF on smooth substrates depends on the surface temperature and can be predicted using the classical model for nucleate boiling by Zuber [137]. A comparative study between the model and our boiling data on the smooth substrate shows an excellent agreement (Figure 12). The results of the nanopillar substrates also suggest that the boiling crisis is mainly dictated by the intensity of the rewetting process, and the increase in critical heat flux is a direct consequence of the faster rewetting velocity using longer nanopillars.

3.4 Conclusion

The boiling behavior in the nucleate boiling regime is significantly affected by the presence of nanopillars fabricated on boiling substrates. Both the heat flux and surface temperature at CHF can be enhanced by increasing the height of nanopillars. We attribute such enhancement to the nanopillar-induced increase in rewetting velocity. Based on the observations that the rewetting velocity increases for substrates with longer nanopillars, as well as the assumption that the enhancement in heat flux dominantly takes place at the three-phase contact line, a mechanistic model was developed to explain the increase in both the CHF and the temperature at CHF of nanopillar substrates. This model takes into account the nanoscales of the pillars, and thus, excludes the wicking motion, or imbibition of

fluid, as plausible mechanisms for heat transfer enhancement. The enhanced capillary force due to the presence of nanopillars is the major cause of the intensified rewetting process and subsequent increases in heat flux and temperature at CHF. The enhancement in both of these critical quantities in pool boiling is a remarkable feature of nanopillar substrates in comparison with nano/micro-engineered substrates in which only either one can be increased and these results provide new insights regarding the design of textured substrate for boiling applications.

4.0 Stable Lotus Leaf-Inspired Hierarchical, Fluorinated Polypropylene Surfaces for Reduced Bacterial Adhesion

4.1 Introduction

Plastics are used in a wide range of medical components such as prosthetics, implants, catheters, and syringes, due to their chemical resistance, versatility in manufacturing, high specific strengths, and low cost [152]. However, contaminating bacteria can attach to plastic surfaces and grow and form biofilms that lead to healthcare associated infections [153]. The consequences on patients and their families are serious, as infections can extend hospital stays, create long-term disability, increase healthcare costs, and even result in unnecessary deaths [154, 155]. In the United States alone, there are 90,000 deaths associated with healthcare-associated infections every year [156] These issues are even worse in developing countries where resources and accountability are poor [157]. Bacteria cause infections by attaching to a surface and forming organized and multicellular biofilms. Two strategies for creating antibacterial surfaces are (1) bactericidal surfaces that kill bacteria cells that come in proximity of or contact the surface and (2) anti-biofouling surfaces that make the bacterial attachment process difficult. In this study, we focus on modifying polypropylene (PP), which is a thermoplastic suitable for use in clinical environments due to its unique rigidness, chemical solvent resistance, and ability to withstand high temperatures compared to other polymers [158]. PP is commonly used for injectors, syringes, medical packaging and cases for contact lenses [159, 160, 161, 162, 163] and is expected to be the fastest growing plastic for medical packaging [164]. Many bactericidal PP surfaces have been studied by incorporating silver nanoparticles-zeolite plastics [165], copper nanoparticles [166, 167], and silver nanoparticles [168, 169]. However, nanoparticles are easily removed by abrasion [170, 171] and the metal ions eventually leach out of the surface completely, rendering the surface sterile against bacteria. Metal ions may also be toxic to aquatic organisms and the environment [172, 173]. Furthermore, bactericide agents must be used in high concentration because many bacteria can sustain growth in low concentrations [174]. Anti-biofouling

PP surface modifications have been investigated to combat these issues. PP membranes have been fabricated by the UV-induced grafting of zwitterionic anti-fouling polymers and demonstrated a 77% reduction in *Escherichia coli* (*E. coli*) adhesion [175]. Anti-biofouling PP surfaces have also been prepared by thermal annealing to create microscale patterns of rice that reduce the adhesion of *E. coli* by 53% compared to controls [176]. In this study, we examined how different reactive ion etching (RIE) processes affect the anti-biofouling properties of PP samples. Our reactive ion etching method provides a single step approach without the need for patterning or the incorporation of additional materials. We studied how different oxygen and fluorine reactive ion etching (RIE) treatments affect the surface chemistry, morphology, and wettability, and bacteria adhesion of PP. We found that a light power oxygen etching treatment creates a hydrophilic surface that reduces bacteria adhesion of *E. coli* by 68.7% compared to untreated PP. Etching a PP surface with high power oxygen creates a surface with about the same surface energy, but nanofibril structures with microscale roughness. These structures exhibit increased bacteria adhesion due to a combination of greater microscale roughness and air pockets that reduce the effectiveness of the liquid barrier. In contrast, we demonstrate substantially reduced bacteria adhesion through lotus-leaf-inspired low surface energy, hierarchical microstructure/nanofibrils in PP. These surfaces exhibit lotus-leaf-like wetting with high static water contact angle (155°) and low hysteresis (less than 10°). Water droplets easily roll off these surfaces as opposed to the other PP samples. Furthermore, these lotus-leaf-like surfaces reduce *E. coli* by 99.6% compared to untreated control samples. These surfaces demonstrate water contact angle stability over a week in contrast to hydrophilic samples, where the contact angle degrades after just one day.

4.2 Methods

4.2.1 Materials

PP sheets were purchased from an online vendor (Small Parts), which have a standard tolerance and meet ASTM D4101-PP0112 specifications [177]. The thickness of the PP sheet was 1.57 mm. Electronic grade acetone (99.5%), methanol (99.9%) and isopropyl alcohol (99.5%) were bought from VWR. Diiodomethane (99%) was bought from Sigma-Aldrich. Deionized water was obtained from a Millipore Academic A10 system with total organic carbon below 40 ppb.

4.2.2 Sample Preparation

Circular coupons with 12.7 mm diameter were made from the PP sheet using a custom-made hole punch. Afterwards, the samples were cleaned with acetone, methanol, and isopropyl alcohol and dried with nitrogen gas. All samples including the control were cleaned with a low power argon plasma (Diener Electronic GmbH) using diffusion process plasma cleaning. The plasma clean parameters for all samples were set to power = 20 Watts, pressure = 100 mTorr, flow rate = 30 sccm and duration = 70 sec. Then, experimental samples were treated by reactive ion etching (Trion III). Two types of samples were prepared by oxygen treatment. Both oxygen treatments were performed under pressure = 100 mTorr, O2 flow rate = 98 sccm, and duration = 120 sec. However, one treatment had high power (HP) of 200 Watts and the other had a low power (LP) of 25 Watts. The fluorinated samples were initially treated with oxygen for 70 seconds and then treated with CF4 and SF6 gasses in order to maximize fluorination at power = 200 Watts, pressure = 250 mTorr, CF4 flow rate = 86 sccm, SF6 flow rate = 52 sccm, and duration = 1800 sec (or 30 minutes).

4.2.3 Surface Characterization

Morphology Characterization The physical morphology of PP surfaces was characterized by scanning electron microscopy (SEM, Zeiss Sigma 500 VP) and atomic force

microscopy (AFM, Multimode SPM with a Digital Instruments Nanoscope III controller). For SEM imaging, the samples were sputter coated with 7 nm gold/palladium (80:20) using a sputter coater (Hummer), as the polymer samples were non-conductive. For AFM, the PP surfaces were imaged in tapping mode, using silicon nitride tips to assess surface topography and roughness in 20 μm by 20 μm areas. The AFM tip had a radius of 8 nm, and the total tip height was 12-18 μm. Data analysis was performed with Digital Instruments version v720 and Gwyddion software. Additionally, dimensional stability was tested with the ASTM D1204 standard (except with 3 inch by 3 inch samples) by comparing the dimensions of samples before and after RIE treatment [178]. Measurements of the sample width and length before and after plasma treatments were conducted using a digital vernier scale caliper.

Contact Angle Measurements and Surface Energy Calculation Static water contact angles (WCA) for all the surfaces were measured using a video contact angle goniometer (VCA 2000 Optima XE). This goniometer utilizes a precision camera and advanced PC technology to capture static or dynamic images of the droplet and determine tangent lines for the basis of contact angle measurement. Contact angle measurements were taken in ambient air at 2225 °C and 2030% relative humidity. Contact angle measurements were taken from 5 μl droplets of deionized water. Similarly, the hysteresis was tabulated for each treatment by measuring the advancing and receding contact angles during syringe controlled water dispersion and withdrawal, respectively. Hysteresis is defined as the difference between the advancing and receding contact angle. The fractional surface areas in analyzing different wetting states were calculated using MATLAB Image Processing Toolbox.

X-ray Photoelectron Spectroscopy All samples were analyzed by x-ray photoelectron spectroscopy (XPS, Thermo Fisher ESCALAB 250 Xi multichannel) with monochromatic Al K radiation. XPS was performed at an acceleration voltage of 15 kV with an emission current of 15 mA, in a residual vacuum of approximately 1×10^9 Torr. The analyzer was used in fixed analyzer transmission (FAT) mode. The spectra were taken from two areas on each sample, and a minimum of two replicate samples were analyzed for each recipe. Sample surface compositions were determined from the average of these measurements.

4.2.4 Bacterial Adhesion Experiments

Adhesion to surfaces was tested using a fluorescent bacterial strain. To generate a fluorescent bacteria, *E. coli* K-12 strain W3110 was transformed by electroporation with GFP expressing plasmid pGFPmut2 [179, 180]. Cultures of the fluorescent *E. coli* were grown in 5 ml of LB broth at 30°C for 18-20 hours with aeration and normalized to $OD_{600} = 0.1$ using saline (NaCl 0.9 %) in a spectrophotometer (SpectraMax M3) [181]. Coupons were glued to the bottoms of the wells of 12 wells plates as previously described and the silicon sealant was allowed to dry for 30 minutes [182]. The wells were then filled with 2.5 ml of the fluorescent bacteria in saline. After 30 minutes at 37°C, the saline was removed, and the coupons were rinsed three times with 2.5 ml of saline to remove non-adhered bacteria. The exposed coupon surface was then placed under a coverslip and observed by fluorescent microscopy (Nikon TE2000-E microscope with a Photometrics CoolSNAP HQ-camera and a 20X objective). NIS-Elements 3.2 software was used to obtain digital images that were then analyzed for the number of attached bacteria using ImageJ software (NIH). In some cases a few loosely attached bacteria cells were observed, which were moving on the surface. Those were manually calculated and subtracted from the counts obtained from ImageJ counts, and these bacteria represented less than 10% of the total bacteria in all cases. The field of view for each picture was 350 μm by 265 μm. Approximately 10 images were taken across the mid-point of each coupon from side to side to gain representative data and eight separate coupons of each type were read for each experiment.

4.3 Results and Discussion

4.3.1 Fabrication

In this study, both oxygen plasma treated hydrophilic and fluorine treated hydrophobic PP samples were investigated. Oxygen plasma tends to render the surfaces hydrophilic, while fluorine tends to make the surface hydrophobic. Both types of RIE treatments were studied as surface wetting properties have been observed to have a significant impact on

bacterial adhesion [183] and both hydrophilic [184]and hydrophobic [185] surface functionalization have been utilized previously to reduce bacterial adhesion. RIE recipes of different samples were tuned for a range of observable wetting results from plasma modified PP. The RIE process modifies the surface morphology from a combination of physical and chemical reactions with the substrate due to the prolonged surface bombardment of activated ions in a controlled environment. We varied the power to prepare two types of oxygen treated samples having similar hydrophilicity, but different surface morphology. Initially, three types of fluorination recipes were evaluated, using only CF4, only SF6 and a combination of both gases, to prepare the hydrophobic samples. Different durations of 10, 30, and 60 minutes were also tested. An optimized recipe for obtaining superhydrophobic samples (in terms of highest contact angle) were obtained while CF4 and SF6 were set at 86 and 52 sccm, respectively for a 30 minute duration.

4.3.2 Surface Characterization

The surface topography and surface chemistry was altered by plasma ion bombardment during the RIE process. The physical morphology of PP surfaces was characterized by SEM. Figure 16 shows the top view and Figure 17 shows the 75° tilted view of SEM images of each types of samples. These images demonstrate the difference in surface morphology of the control (Figure 17a), LP oxygen sample (Figure 17b), HP oxygen sample (Figure 17c), and fluorinated sample (Figure 17d). The surface of the untreated control samples and the LP oxygen treated samples look similar and are both relatively smooth. On the other hand, the surface of HP oxygen treated samples show nanofibril structures. The HP oxygen PP surface morphology consists of dense forests of nanofibrils about 40 nm diameter and 1 μm height. The fluorinated samples have hierarchical features, with microstructures of about 1 μm in height and nanofibrils of about 30 nm diameter of about 0.5 μm height. These nanofibrils are not as dense as the HP oxygen treated samples.

The surface morphologies of the four types of samples were further characterized by AFM (Figure 18a). The surface morphology was characterized by the root mean square (RMS) roughness and the power spectral density function. The RMS value of the surface

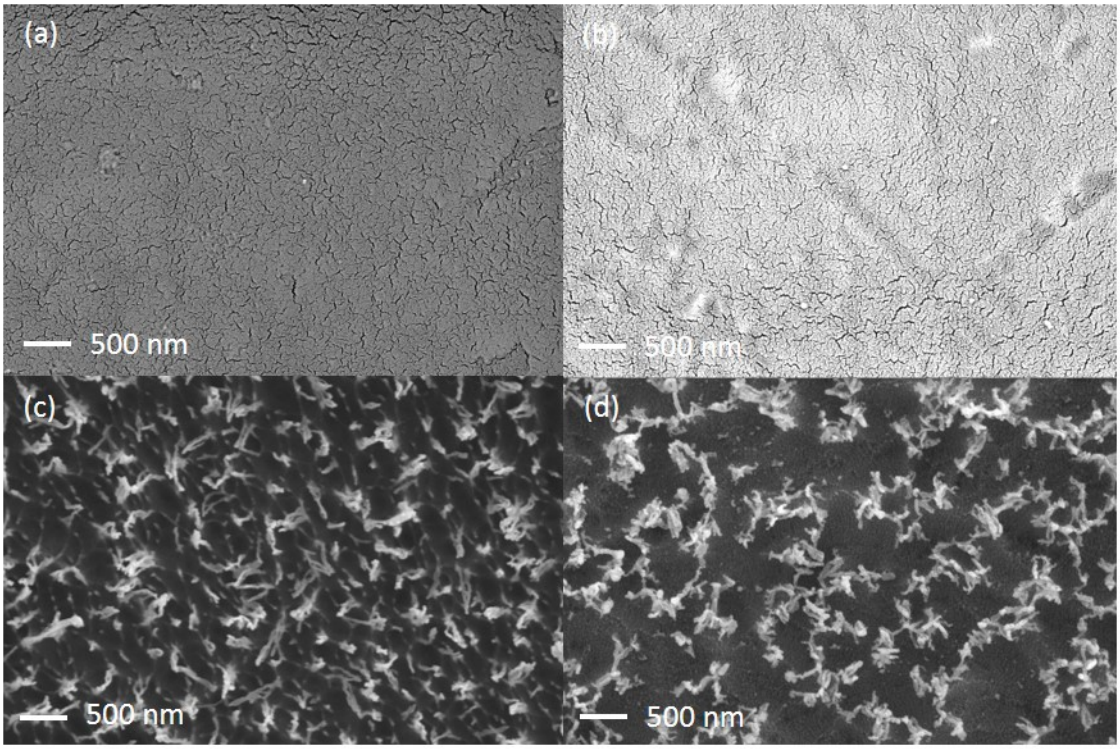

Figure 16: Top view SEM images of different samples: (a) Control, (b) LP oxygen, (c) HP oxygen, and (d) fluorinated samples. All images were taken at same magnification level.

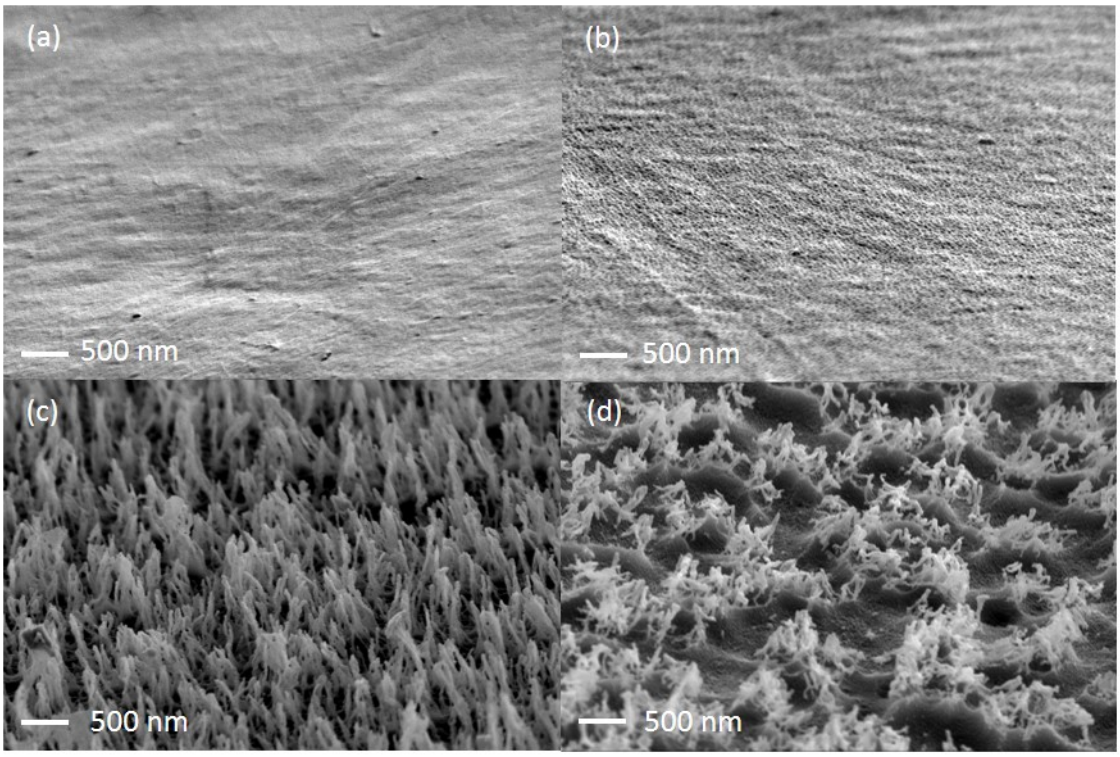

Figure 17: 75° tilted view SEM images of different samples: (a) Control, (b) LP oxygen, (c) HP oxygen, and (d) fluorinated samples. All images were taken at same magnification level.

roughness of the control, LP oxygen treated, HP oxygen treated, and fluorinated samples were 20, 37, 230, and 154 nm respectively. While the untreated and LP oxygen treated samples are relatively flat, the HP oxygen treated samples and the fluorinated samples have much more roughness. Figure 18b plots the roughness power spectral density as function of the roughness wavelength. The HP oxygen sample has more roughness across all length scales compared to the LP oxygen sample. For length scales below 1 μm, the surface is self-affine or fractal [186] as the power spectral density has a power-law dependence on the spatial frequency of roughness. For roughness wavelengths above 1 μm, the power spectral density is fairly flat. In contrast, the fluorinated PP samples are self-affine across almost the entire roughness wavelengths shown, ranging from 20 μm down to 100 nm. This self-affinity across multiple length scales is also present in lotus leaves [187] and why we describe these surfaces as hierarchical.

The dimensional stability of the PP was also evaluated after RIE. Morphological changes may occur in thermoplastics from high temperature treatments due to the mismatch between the thermo-elastic properties of the polymer matrix and fibril structures [188]. The mean dimensional changes of LP oxygen treated, HP oxygen treated, and fluorinated samples were $0.03\% \pm 0.05\%$, $-0.42\% \pm 0.23\%$, and $0.13\% \pm 0.10\%$, respectively. All types of samples were dimensionally stable with negligible changes in length and width after the corresponding reactive ion etching treatments.

Figure 19 shows static water contact angle (WCA) results on the four different types of samples during WCA. The static WCA weas measured for 3 samples of each type at 3 random spots per sample. The numbers in the figure denote the mean and standard error among treatments. The WCA was $98 \pm 0.9^\circ$ for the control samples where the $\pm 0.9^\circ$ refers to the standard error of the 9 measurements. Both types of samples prepared by oxygen treatment were hydrophilic. The LP oxygen treated samples had WCA of $51 \pm 1.3^\circ$ and HP oxygen treated samples had WCA of $72 \pm 1.5^\circ$. On the other hand, the fluorinated samples are superhydrophobic with a WCA of $156 \pm 0.6^\circ$.

The advancing, and receding contact angle of the four samples were further characterized. Figure 20 shows the results of this characterization where 3 samples were again measured 3 times each. The hysteresis is the difference between the advancing and receding contact

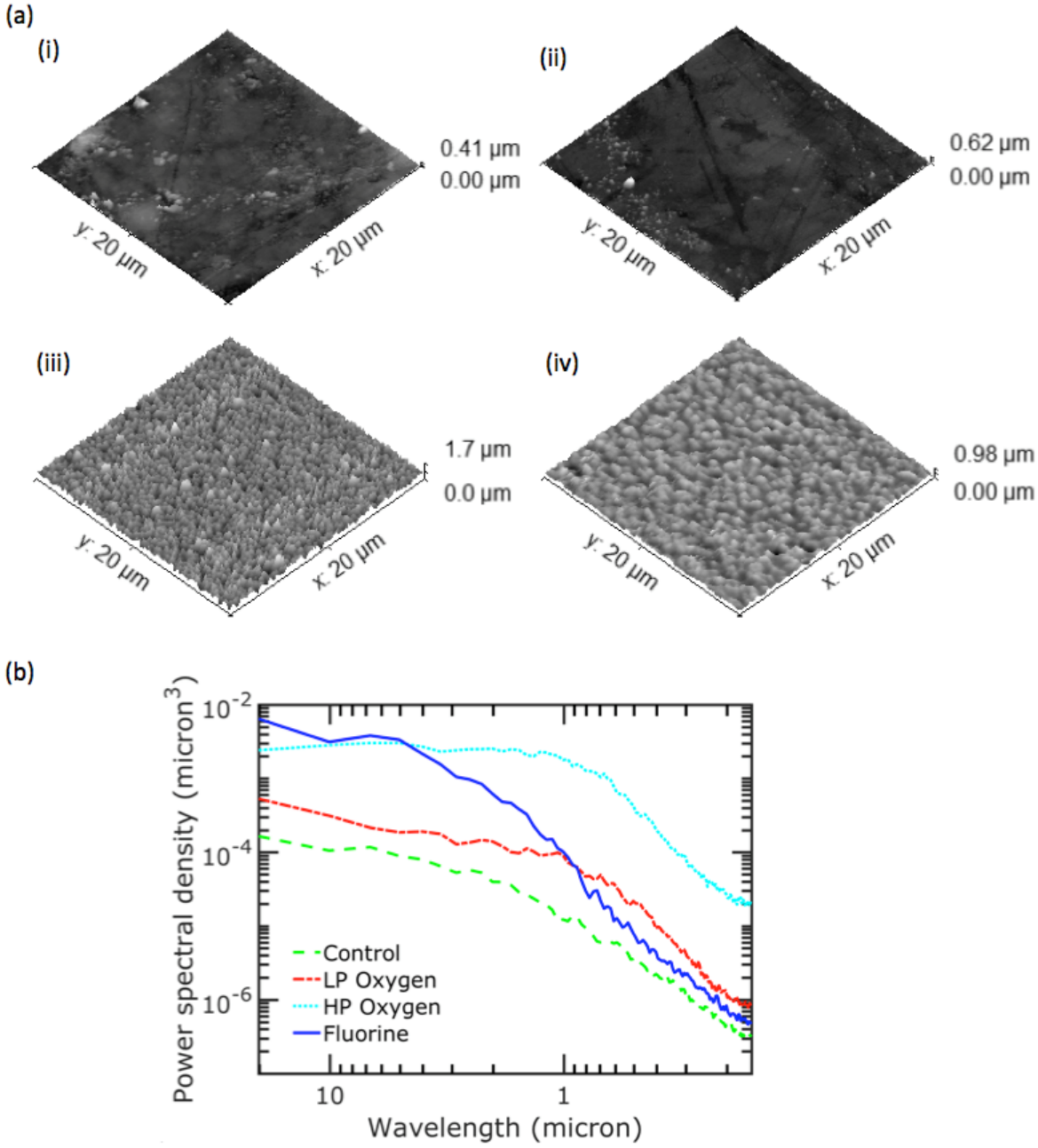

Figure 18: (a) 3-D plots by AFM show physical surface at microscale of different samples (i) Control, (ii) LP oxygen, (iii) HP oxygen, and (iv) fluorinated, (b) Power spectral density of four samples as a function of roughness wavelength.

RIE Recipe	Control	Low Power Oxygen	High Power Oxygen	Fluorinated
Contact Angle	98° ± 0.9°	51° ± 1.3°	72° ± 1.5°	156° ± 0.6°
Images	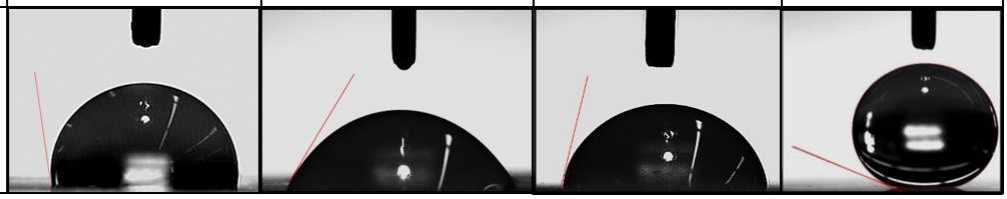			

Figure 19: Contact angle of different samples and representative images of the water.

angles. The hysteresis was fairly high for the control sample and the oxygen treated samples, which are indicative of strong adhesion between the water and PP. These three samples may all be turned upside down with the water droplet still adhering to the substrate (Figure 20 images). On the other hand, the contact angle hysteresis for the superhydrophobic samples was approximately less than 10°, suggesting that the adhesion force between the liquid and surface is weak [189]. The water droplets easily roll off these surfaces with the slightest tilt. This combination of high WCA and low hysteresis is referred to as the lotus leaf wetting state and an indicator of self-cleaning ability [189].

The total surface energy of different samples was calculated from Fowkes method experiments, where the contact angle of diiodomethane, Θ_{DIM}, and water Θ_{H20} were used to calculate the total surface energy values (Table 5). Static contact angles of diiodomethane (DIM), a purely dispersive liquid, were measured together with those of water, a highly polar liquid [190]. The independent dispersion and polar surface energy components for each sample type are calculated using Youngs and Dupres definition of adhesion equations. These quantities are summed for the overall surface free energy [191, 192]. Youngs contact angles were obtained from the observed contact angle values and corresponding wetting state equations. For the Wenzel wetting state,

$$cos(\theta_W) = rcos(\theta_Y) \tag{4.1}$$

RIE Recipe	Control	Low Power Oxygen	High Power Oxygen	Fluorinated
Advancing CA	106.0° ± 1.2°	78.4° ± 3°	90.5° ± 3.1°	156.5° ± 1.1°
Receding CA	62.8° ± 3.2°	18.2° ± 2.9°	20° ± 1.4°	147.5° ± 1.2°
Hysteresis	43.1° ± 3.2°	60° ± 3.7°	70.5° ± 3.4°	8.9° ± 1.1°
Images	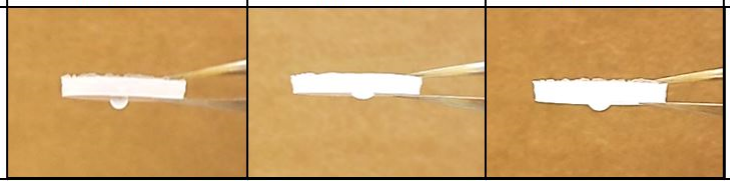			

Figure 20: Contact angle hysteresis of different samples and images of 180° tilted samples. No image is obtained for the Fluorinated sample as water droplets easily roll off these surfaces with the slightest tilt.

where θ_W is the observed contact angle in the Wenzel wetting state and θ_Y is the Youngs contact angle. In the Cassie Baxter wetting state,

$$cos(\theta_{CB}) = rfcos(\theta_Y) - (1 - f) \tag{4.2}$$

where θ_{CB} is the observed contact angle in the Cassie Baxter wetting state. r is the roughness ratio factor and f is the solid-liquid fractional surface area where 1- f is the solid-air fractional surface area. The flat control and LP oxygen samples are in the Wenzel wetting state due to the relatively flat surfaces. In the Wenzel wetting state, the roughness parameter enhances the intrinsic wetting property of a surface, while in the Cassie-Baxter wetting state the roughness always make the surface more hydrophobic. The observed wetting behavior of the HP oxygen samples suggests that they are in the Cassie-Baxter wetting state. In addition, the fluorinated samples must be in the Cassie-Baxter wetting state due to the superhydrophobic behavior of the surface. The mean and standard error of these values are shown in the table. The surface energy, $_S$ is the sum of the dispersive and polar component of surface energy. The fluorinated samples are superhydrophobic due to a combination of low surface energy and hierarchical surface structures. In contrast, the oxygen treated samples have high surface energy, explaining the lower static contact angles and higher hysteresis.

Table 5: Roughness ratio factor (r) , solid-liquid fractional surface area (f), and Youngs contact angle (Θ_Y), Diiodomethane (DIM) contact angle (Θ_{DIM}), water contact angle (Θ_{H_20}), surface energy of different samples (Ω_S)

	r	f	Θ_Y (Degree)	Θ_{DIM} (Degree)	Θ_{H_20} (Degree)	Ω_S (mNm-1)
control	1.03	1	98.2	60 ± 2.2	98 ± 0.9	28.4 ± 2
LP Oxygen	1.11	1	55.3	62 ± 2	51 ± 1.3	46.7 ± 2.3
HP Oxygen	3.02	0.38	36	13.5 ± 3.0	72 ± 1.5	59.6 ± 2.2
Fluorinated	2.63	0.21	103.2	110 ± 4.4	156 ± 0.6	12.9 ± 2.2

Table 6 summarizes our XPS results. It was observed the fluorinated samples had 55% fluorine on the surface. The untreated samples did not have any fluorine, while the LP oxygen treated samples had very small amount fluorine (0.85%). However, the HP oxygen treated samples had higher amount of fluorine (5%) compared to the control and LP oxygen treated samples. The presence of fluorine in our HP and LP oxygenated samples are possibly due to the presence of fluorine in the chuck and backstreaming of oil during the RIE process. XPS survey scan of different samples are shown in Figure 22-25.

Contact angles were measured over a week of time for all samples to check the stability (Figure 21). The standard error was always within 2° for control, LP oxygen treated and fluorinated samples, while it was a little higher (4°) for HP oxygen treated samples. The LP and HP oxygen treated samples were observed to have decreasing hydrophilicity in ambient conditions after just one day. This is likely due to particulates landing on the high energy surface. However, the fluorinated samples demonstrated stable superhydrophobicity over a week as the mean contact angle was always higher than 146°. The fluorinated samples were also observed to be chemically stable in ambient conditions for over a week. XPS analysis was conducted after one week of sample preparation and showed negligible change in atomic percentage of fluorine, demonstrating that the fluorine ions on the surface are stably bounded from polar covalent carbon-fluorine bonds formed after treatment (Figure 26).

Table 6: XPS surface chemical analysis of the various surfaces

Atomic %						
Name	C 1s	O 1s	N 1s	F 1s	Si 2s	Al 2p
Control	88.35	9.55	0.73	0	1.37	0
LP Oxygen	82.16	13.89	0.75	0.85	0.97	1.38
HP Oxygen	66.39	21.09	1.38	5.51	1	4.63
Fluorinated	43.19	0.86	0.68	55.27	0	0

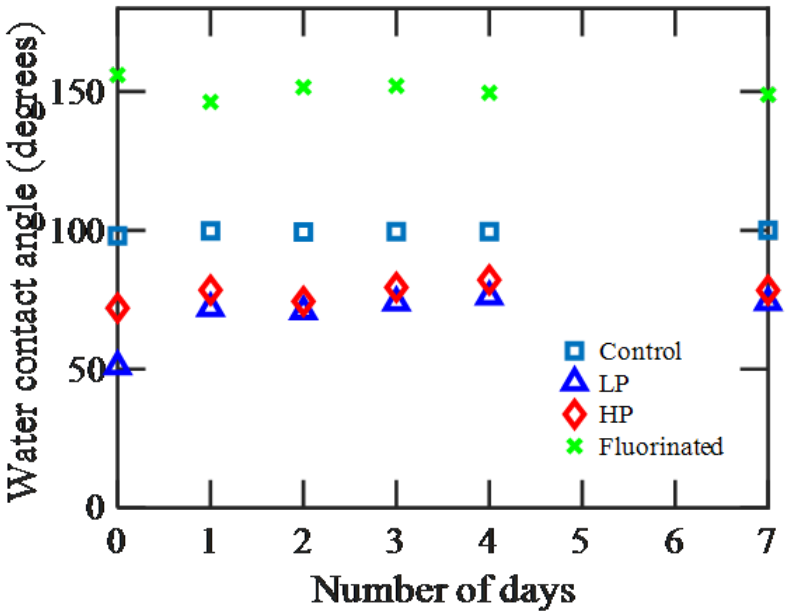

Figure 21: Water contact angle of different samples over time.

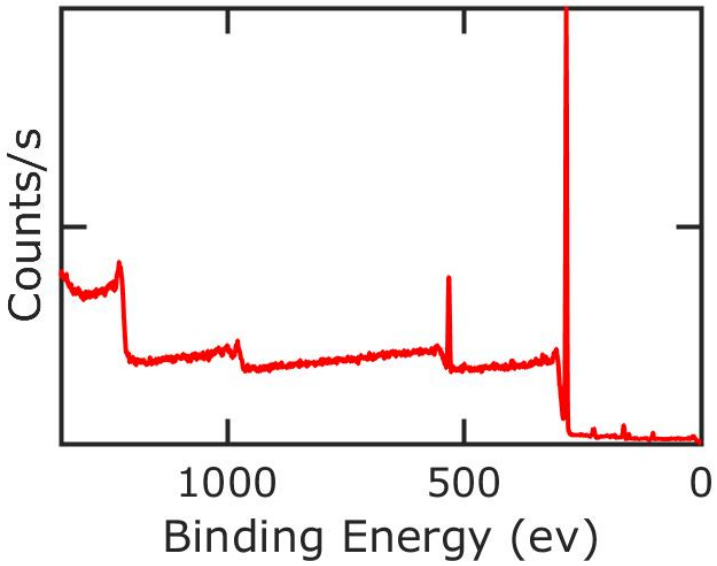

Figure 22: XPS survey scan of control sample.

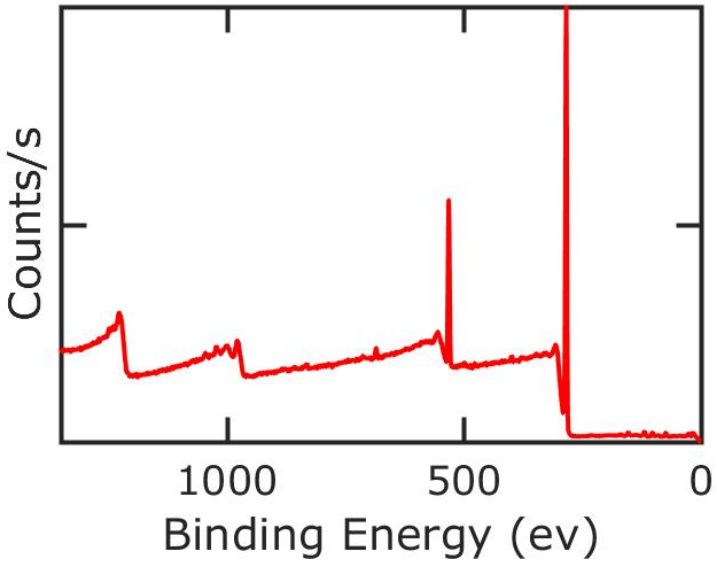

Figure 23: XPS survey scan of LP Oxygen treated sample.

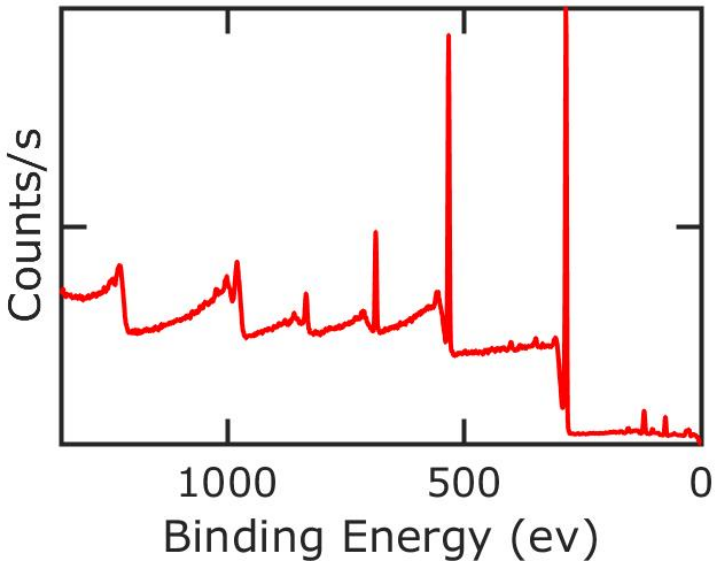

Figure 24: XPS survey scan of HP Oxygen treated sample.

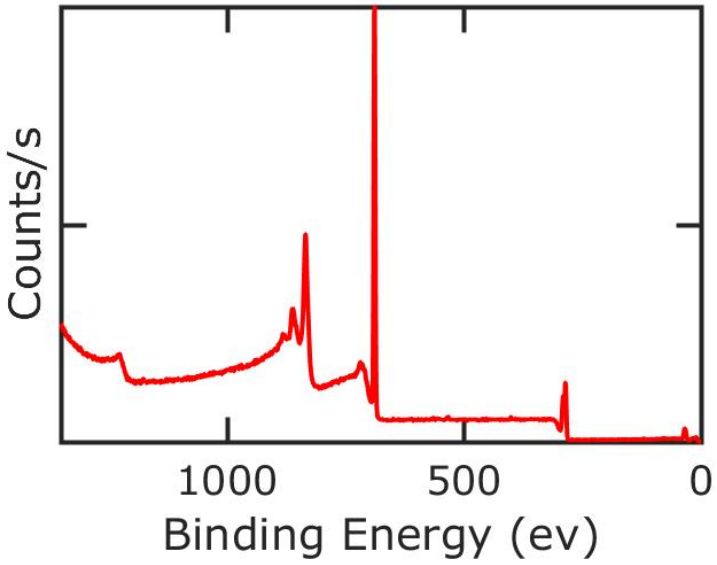

Figure 25: XPS survey scan of Fluorinated sample.

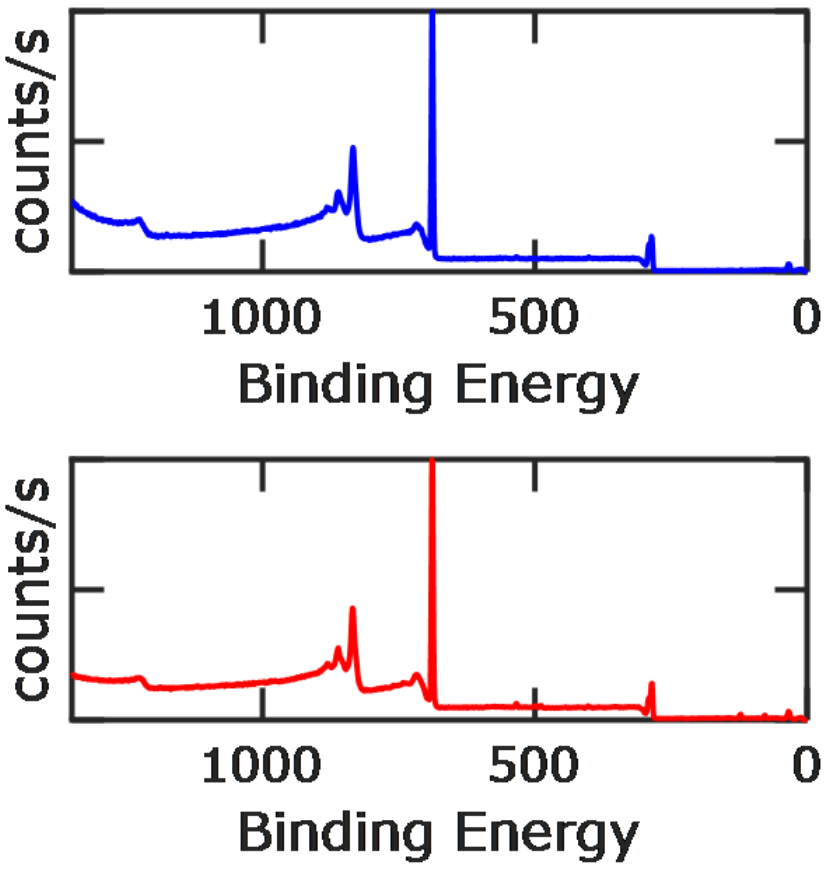

Figure 26: Comparison of XPS survey scan of fresh fluorinated samples (top) and 1-week old fluorinated samples (bottom).

4.3.3 Results of Bacterial Adhesion Tests

Figure 27 shows the results of the bacterial adhesion experiments and fluorescent representative images of different treated samples with bacteria. Bacterial adhesion was evaluated by fluorescent optical microscopy. Afterwards, ImageJ software was used to count the number of bacteria cells that adhered to the surface. The number of bacteria cells per millimeter squared is plotted for each sample type. Eight coupons were characterized for each RIE treatment. The red solid line represents the mean count, the pink region represents the standard error around the mean, and the black circles represent individual data points. Results show the difference between the LP oxygen treated samples (1209 ± 120 cells/mm^2) and the HP oxygen treated samples (5176 ± 835 cells/mm^2). The LP oxygen treated samples exhibit a decrease in adhered bacteria compared with the control. The decreased bacteria adhesion in these samples is because the hydrophilic surface energetically maintains a liquid barrier between the surface and the bacteria cells, hindering cell-to-surface contact [193, 194]. On the other hand, the adhesion of *E. coli* to the HP oxygen treated samples was much more than the control samples. While the surface energies of both types of samples are similar (Table 5), the surfaces of HP oxygen treated samples consist of dense nanofibrils in contrast to the relatively flat LP oxygen treated samples. The power spectral density of HP oxygen treated samples show a significantly higher frequency of roughness across all roughness wavelengths compared to the relatively flat LP oxygen sample. The increase in bacterial adhesion to the HP oxygen samples might be attributed to the increased wavelength roughness that is equivalent or larger than *E. coli* cells (rod-shaped about 2 μm long and diameter .25 to 1 μm). This roughness increases surface to cell binding sites. Furthermore, the HP oxygen samples contain air pockets that may decrease the effectiveness of the liquid barrier between the bacteria cells and surface. Indeed, these air pockets are why the water contact angle of the HP oxygen surfaces increase over that of LP oxygen surfaces. The effect of surface roughness on bacterial adhesion was studied previously. Harris *et al.* mentioned the effect of surface morphology on the adhesion of Staphylococcus aureus on the micro-rough and electropolished titanium surfaces [195]. Irregularities of polymeric surfaces promotes bacterial adhesion whereas ultra-smooth surfaces do not [196]. The size of roughness irregularities in

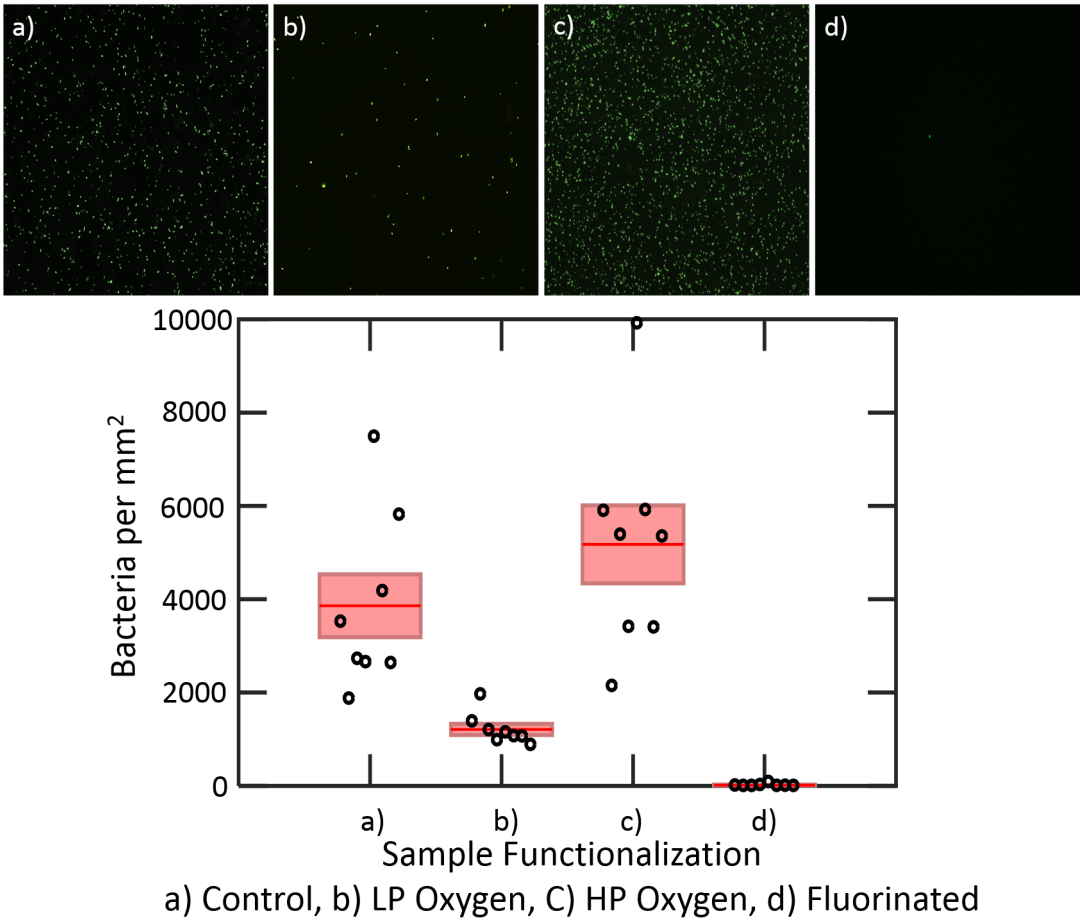

Figure 27: Bacterial counts per mm^2 for differently treated samples and fluorescent images of PP samples with adhered bacteria. The red solid line represents the mean count, error bars indicate standard error (n=8). a) Control, b) LP oxygen plasma treated, c) HP oxygen plasma treated, d) Fluorinated plasma treated.

comparison to the size of the bacteria seems an important parameter. Previous study on bacterial adhesion reported that bacteria adhere more to irregularities that conform to the size of the bacteria, as this maximizes the surface area in contact with the cell [197]. Our HP oxygen samples had increased wavelength roughness that is equivalent or larger than *E. coli* cells and an increase in adhesion was observed for these samples. On the other hand, depressions or grooves too small for bacterium to fit into reduce the contact area of the bacterium, and hence adhesion [197].

The best results were obtained with fluorine plasma treated samples, which are lotus leaf-like. Lotus leaf surfaces are superhydrophobic due to their micron-sized papillae with nanometer-size protrusions and low surface-energy layer of epicuticular wax [198]. These structures are known to resist fouling from soil or dust [199, 200, 201]. Likewise, our treatment creates hierarchical microstructure/nanofibrils from a fluorine plasma etch process and the fluorination provides low surface energy. These PP surfaces exhibit lotus-leaf wetting due to a combination of high water static contact angle and low hysteresis. The number of bacteria cells adhered to the fluorinated samples (15 ± 10 cells/mm^2) was extremely low, 99.6% less than the control samples (3860 ± 673 cells/mm^2). Under the fluorescent microscope, barely any bacteria cells could be seen on these samples. The nanofibrils are smaller in size than bacteria and together with low surface energy significantly reduce the number of adhesion sites for *E. coli* cells. These fluorinated PP samples emulate the lotus leafs self-cleaning ability. Statistical analysis (Two-Sample t-Test) was done to evaluate the significance of the anti-biofouling performance of the various samples. The p values were 0.006, 0.242, and 0.001 when the control was compared to the LP oxygen treated samples, HP oxygen treated samples, and the superhydrophobic, lotus-leaf like fluorine treated samples, respectively.

4.4 Conclusion

We studied how reactive ion etching modifies the surface of PP samples and affects bacterial adhesion. The effect of different reactive ion etching recipes on morphology, surface energy, and wettability was also investigated. The bacteria adhesion on the LP oxygen

treated samples was significantly lower compared to the HP oxygen treated samples. The best anti-biofouling results were obtained from fluorine reactive ion etched samples that created lotus leaf-like hierarchical structures consisting of microstructures and nanofibrils. These PP surfaces exhibit super hydrophobicity, low hysteresis, and 99.6% less adhesion of *E. coli* than control samples. The combination of low surface energy and hierarchical morphology reduces the number of active sites for *E. coli* to adhere to the treated PP, emulating the lotus leaf self-cleaning effect.

5.0 Bactericidal Effect of Silicon Nanostructured Surfaces

5.1 Introduction

There is a great need for antibacterial surfaces that may reduce infections and illness in healthcare applications such as medical devices, sutures, contact lens cases, dental implants and catheters [202, 203, 204, 205, 206, 207, 208] as well as everyday household items such as kitchen and bathroom surfaces, appliances [209, 210], consumer hygiene products, health club equipment, and food packaging. The most widely used strategy has been the use of some sort of antimicrobials such as organic compounds like triclosan and zinc pyrithione [211, 212] or metallic ions such as Ag^+ [213]. However, this approach suffers from drawbacks such as high-cost, short-term efficacy, and biological and/or environmental toxicity [214, 215, 216]. Bacteria have also evolved resistance and can sustain growth in the presence of low concentrations of antibiotics [217].

Recent nanofabrication approaches have been able to demonstrate bio-inspired antibacterial surfaces that either reduce bacteria adhesion or mechanically kill bacteria cells. The first approach uses a combination of surface nanotopography and surface functionalization to reduce bacteria adhesion [75, 218] .The second approach was inspired by the wings of insects (*Psaltoda claripennis*) wing surfaces are bactericidal to *Pseudomonas aeruginosa* cells [219]. However, cicada wing structures have demonstrated limited effect on rigid bacteria cells such as Gram-positive bacteria [220], which have a peptidoglycan cell wall about 4 to 5 times thicker than those of Gram-negative bacteria [221]. Ivanova *et al.* compared the bactericidal activity of black silicon to that of the wings of the dragonfly *Diplacodes bipunctata* [222]. Both the needle like structures on the surface of black silicon and the nanoprotrusions on the dragonfly wings form hierarchical structures and a mechanical bactericidial effect is observed. Hazell *et al.* used black silicon and diamond coated black silicon substrates with variuos surface morphologies and tested those surfaces against both Gram-positive and Gram-negative cells [223]. However killing was only observed for Gram-negative cells. It is attributed to the difference in the thickness of the cell wall of Gram-positive bacteria

compared to Gram-negative bacteria. The thickness of the cell wall of Gram-positive bacteria is around 20-80 nm, which consists of several layers of peptidoglycan. On the other hand, the cell wall of most Gram-negative bacteria is 5-10 nm thick, consisting of a single peptidoglycan layer [224]. This same phenomenon has been observed in other studies also, where the bactericidal effect against Gram-positive bacteria was negligible compared to that of Gram-negative bacteria [223, 225]. As previous studies found the gram positive bacteria difficult to kill, we concentrate on the killing of Gram-positive bacteria cells in the present study.

Infections due to bacterial adhesion is very common for implanted medical devices and extensive research is being done to address this issue. We focus on *Staphylococcus epidermidis* (*S. epidermidis*), a Gram-positive bacteria, which is a common source of infections on indwelling medical devices such as catheter. To evaluate the mechanical bactericidal effect on this bacteria, we prepared uniform and regular SiNC arrays. The morphology of these structures were varied and optimized. As mentioned earlier, the bactericidal nature of the nanostructures on cicada wings and black silicon, was demonstrated in recent research. But these random structures lack uniformity, both in terms of distribution of the structures and their shape. We have been able to fabricate uniform and regular nanostructured arrays with control over pitch, diameter, taper, and height. Nanosphere lithography (NSL) and combination of reactive ion etching (RIE) and deep reactive ion etching (DRIE) were utilized to prepare uniform silicon nanostructure arrays of different morphology. The objective of this current study is to investigate the impact of these parameters on the bactericidal performance of SinC arrays, while they are varied systematically. Our results demonstrate that these structures have a mechanical bactericidal effect on *S. epidermidis* and we present results on how morphology affects this killing rate.

5.2 Experimental Procedure

5.2.1 Fabrication of SiNC Substrates

P-type boron-doped (100) silicon wafer was used as substrate. The substrate was cleaned with acetone, methanol and isopropanol and then dried with nitrogen gas. Then polystyrene (PS) nanospheres were patterned on the substrate by the self-assembly method [226, 227, 228]. PS nanospheres were self-assembled in the air-water interface and then the monolayer was transferred to the substrate. After that the substrate was dried in air at room temperature. Then, reactive ion etching (RIE) with oxygen was used to reduce the diameter of the PS nanospheres. The pressure was set at 25 mTorr and the RF power was set at 25 W. The flow rate of oxygen was 25 sccm, which yielded an etch rate of 80 nm per minute. By varying the etch duration, it is possible to vary the diameters of the mask and hence that of the nanowires. After that we used the Inductively coupled plasma reactive ion etching (ICPRIE) to etch the silicon, while the PS nanospheres served as the mask for silicon. SF_6 was used as the etch gas and C_4F_8 was used as the passivation gas. After varying the ratio of the gases and observing the structure of the nanowires, the optimal ratio of the etch gas and passivation gas was determined to be 33 sccm : 82 sccm. The etch duration was varied to obtain nanowires of different height. Typically the height of the nanowires increased with an increase of etch duration. We observed tapering effects on the nanowires and all structures had different top and bottom diameters. Finally, we removed the PS nanospheres by ultrasonication in acetone for 5 minutes.

5.2.2 Bacterial Culture Preparation

A 5mL overnight culture was inoculated with a single colony from a streak plate and was incubated at 37°C for approximately 8 hours. A 50mL culture was then inoculated from the overnight culture in mid-exponential phase by combining 2mL of the culture and 48mL of peptone yeast-extract dextrose (PYD) in a 250mL baffled flask. The culture was incubated for 18 hours overnight at 37°C. The following day, the OD_{600} was taken and proved to be 1.49 abs. The 50mL culture was transferred to a 50mL conical tube and was centrifuged at

5000g by repeated inversion. The bacterial culture was then diluted 1:10 in 0.01M PBS by combining 5 mL of the culture with 45 mL of 0.01M PBS in a new 250 mL flask. This new culture yielded an OD_{600} of 0.1 abs.

5.2.3 Bacterial Experiment

For all samples, 10 μL of the 1:10 *S. epidermidis* PBS culture was aliquoted onto each substrate of 1.5 cm by 1.5 cm size. Separate samples were used for different time points. For the zero hour time point the culture was dropped and then withdrawn immediately from the substrates. For the one hour and three hour time points, the substrates were kept inside a humidity controlled environment after the culture was aliquoted for the specified amount of time. The relative humidity was maintained at nearly 100% to avoid evaporation. As complete recovery of the 10μL culture is difficult 90μL PBS was added and mixed well by pipetting before the 100μL was withdrawn. Then the bacterial culture was serially diluted 10-fold in 270uL of 1x PBS. Then 100ul was plated on PYD agar and spread with sterile glass beads. The bactericidal effect was evaluated in triplicate for both the bare silicon control and SiNC arrays. The plates were incubated at 37°C for 24 hours. Afterwards the plates were counted and CFU/mL counts were obtained. SEM was used to evaluate the surface of the used SiNC samples after the experiment.

5.3 Characterization of Fabricated Substrates

The physical morphology of the SiNC surfaces was characterized by scanning electron microscopy (SEM, Zeiss Sigma 500 VP). Top view, cross sectionl, and tilted view SEM images (Figure 28) were taken. The height, pitch and Tip diameter of different samples were measured using the SEM. Static water contact angles (Figure 29) for all the surfaces were measured using a VCA 2000 Optima XE video contact angle goniometer. This goniometer utilizes a precision camera and advanced PC technology to capture static or dynamic images of the droplet and determine tangent lines for the basis of contact angle measurement.

Table 7: Topographical parameters of SiNC substrates, as measured by SEM

Sl	DRIE Duration(min)	Pitch(nm)	Top diameter(nm)	Height(μm)
1	32	1400	460	6
2	17	800	110	2.3
3	11	500	80	2
4	7	300	80	1

Contact angle measurements were taken in ambient air at 22-25 °C and 20-30 % relative humidity. Contact angle measurements were taken from 5 μl droplets of deionized water.

5.4 Results and Discussion

In order to study the pitch dependence of the SiNC substrates we fabricated samples of different pitch. The pitch of 4 types of samples were 300, 500, 800, and 1400 nm. The diameter of *S. epidermidis*, the bacteria used for the experiments, is 0.7-1 μm. Hence, the pitch of two types of samples were smaller than the diameter of the bacteria. The other two samples had pitch larger than or in the same level of magnitude compared to the bacteria. The height of the samples also varied due to the nature of the deep reactive ion etching process. From cross-section SEM images the height and top diameter of the structures were measured. The measurements have been tabulated in table 7. The height of the structures varied between 1 μm, and 6 μm, while the tip diameter varied between 80 nm, and 460 nm.

No difference in the CFU/mL counts was observed at the zero hour time point for any types of samples. As mentioned earlier the 10 μL bacterial culture was aliquoted and retrieved immediately to get the data for zero hour time point (Figure 30). It was done to ensure that no difference in the counts were observed because of the presence of the nanos-

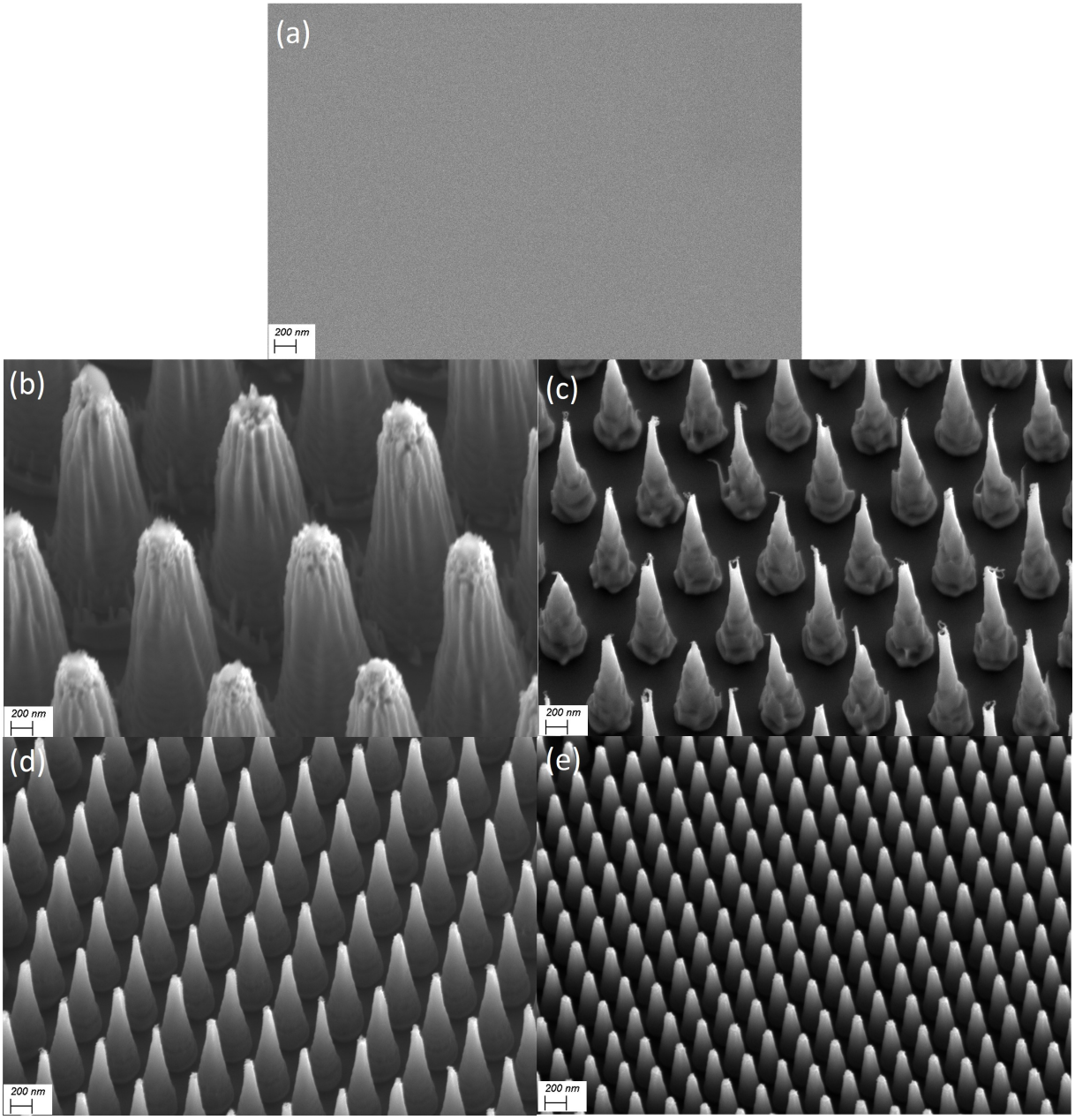

Figure 28: SEM image of fabricated SiNC substrates. a) Bare silicon, b) 1400 nm pitch, c) 800 nm pitch, d) 500 nm pitch, e) 300 nm pitch.

tructures only, when there was not sufficient time of interaction. The bactericidal effect for a particular type of sample was quantified by subtracting the number of surviving cells on the

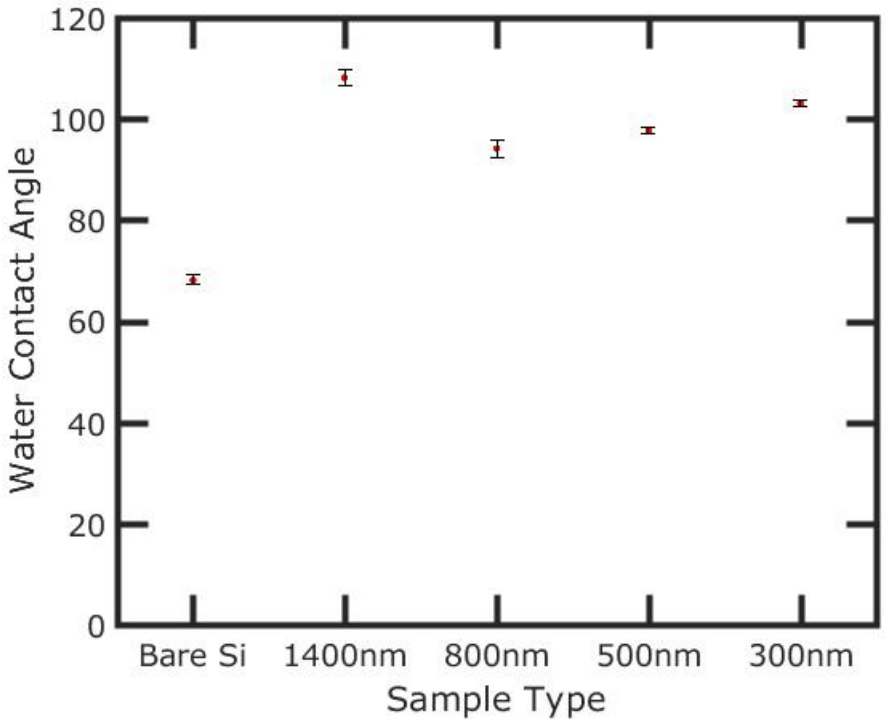

Figure 29: Measured water contact angle of fabricated bactericidal samples. Error bars indicate standard error.

substrate from the number of cells remaining in the bare silicon sample at the corresponding time point. At the one hour time point bactericidal effect was observed only for the 300 nm pitch samples. 20% killing was observed for these samples. For the other types of samples, there was some natural variation. But the killing was not evident at the one hour time point. At the three hour time point, some mild killing was observed for 800 nm and 1400 nm pitch samples. Both of these samples exhibited around 10% killing of *S. epidermidis*. 500 nm pitch samples had around 30% killed. While the best performance was observed for the 300 nm pitch samples. These samples had significantly reduced the number of viable cells and the killing was measured to be around 82%.

The difference in the number of cells for different samples can be seen in Figure 31. Among different reports regarding the bactericidal effects of nanostructured surfaces, some

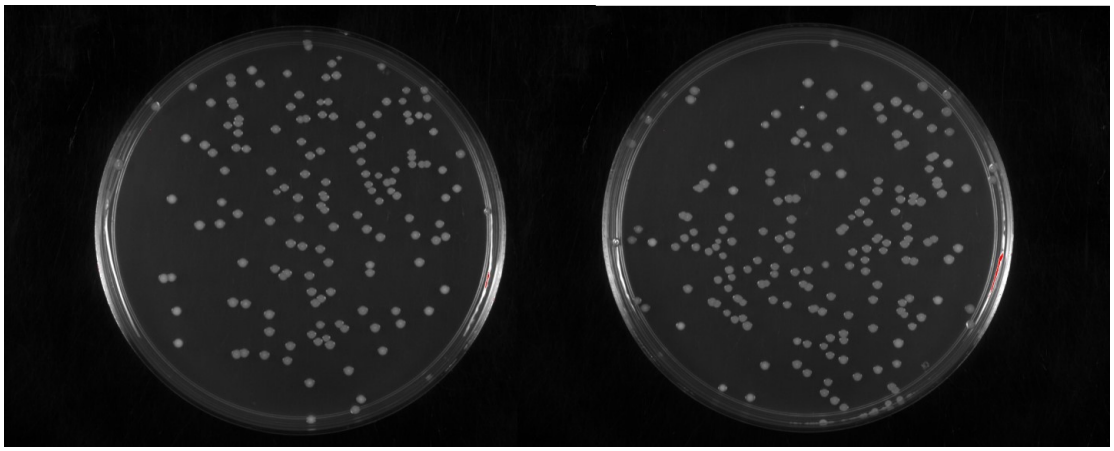

Figure 30: Representative optical images of plates of the 0 hour time point at the end of the 24 hour incubation period.

reports suggested that the pitch of the nanostructures plays an important role in the bactericidal performance and an increase in bactericidal performance is observed associated with the variation of pitch. It has also been reported that there exists some optimal pitch, for which the best bactericidal performance is obtained [223]. Wu *et al.* studied the antibacterial properties of gold nanostructured surfaces and varied the height of these nanostructures [229]. They reported that structures with smaller height (50 nm) did not allow sufficient stretching/deformation of the cell membrane and most of the bacteria cells appeared alive. However, the minimum height of our structures was 1 μm, 20 times larger than this reported lower limit.

We observed the maximum death on the 300 nm pitch samples, which had the nanostructures with minimum height and maximum density. Figure 32 summarizes the results of our experiments at the 3 hour time point. The mechanism behind the bactericidal effects of nanostructured surfaces have been studied and different theories have been provided. We suggest that the stretching of the cell membrane is insufficient for cell rupture, when the pitch is larger than/comparable to the diameter of the *S. epidermidis* cells. The bacteria cells can settle down at the vacant large spacing among the nanostructures. This is verified by the SEM images (Figure 34), obtained after the experiment for the 800 nm and 1400 nm pitch

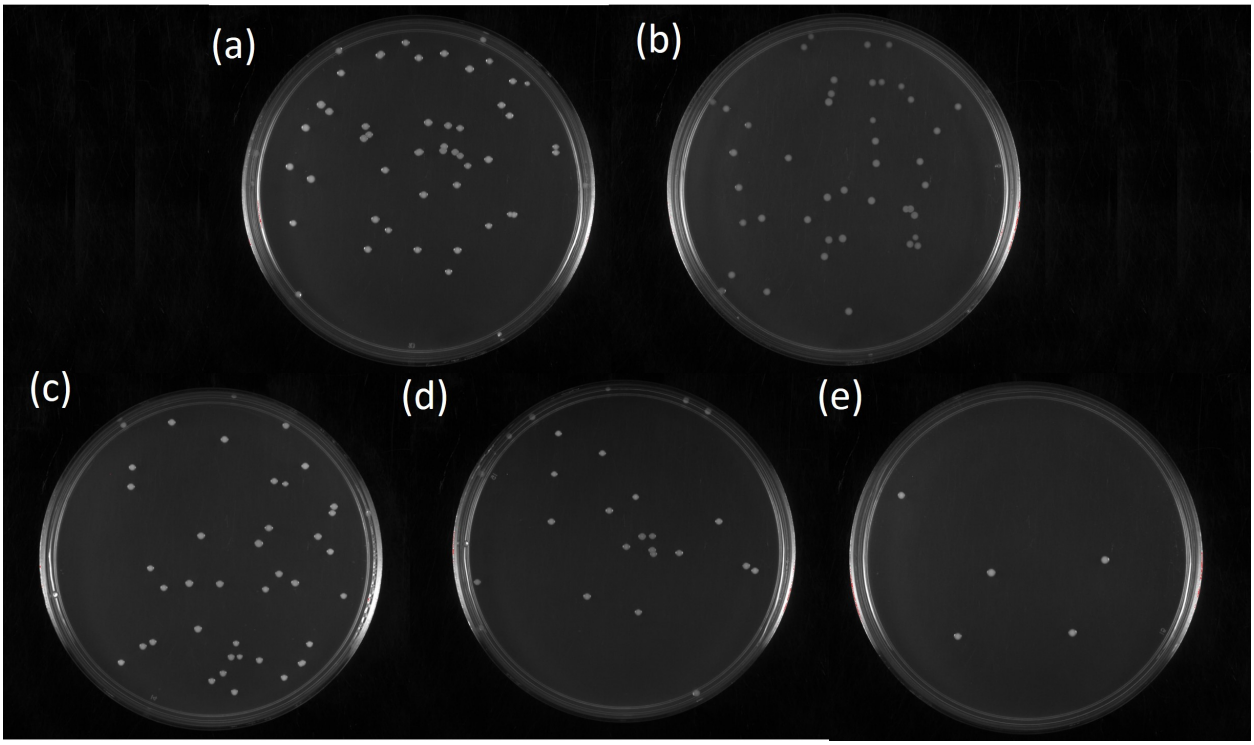

Figure 31: Representative optical images of plates of the 3 hour time point after the 24 hour incubation period. (a) bare silicon, (b) 1400 nm, (c) 800 nm, (d) 500 nm, (e) 300 nm pitch samples.

samples. The small percentage of observed killing might be due to the direct penetration of the membrane by the nanostructures.

On the other hand, when the pitch is smaller than the diameter of the bacteria cell, there is not sufficient spacing among the nanostructures for the bacteria cells to settle down. The bacteria cells sit on top the nanostructures. Multiple nanostructures, present underneath individual cells for both 300 nm and 500 nm pitch samples, causes stretching of the bacterial cell membrane. Based on the number of nanostructures underneath the cells the stretching impact varies. The 300 nm pitch samples having a density of 2.8 times compared to the 500 nm substrates have a significantly higher impact in this regard. The cell death mechanism can be explained in the following manner. Because of the significant stretching impact on the

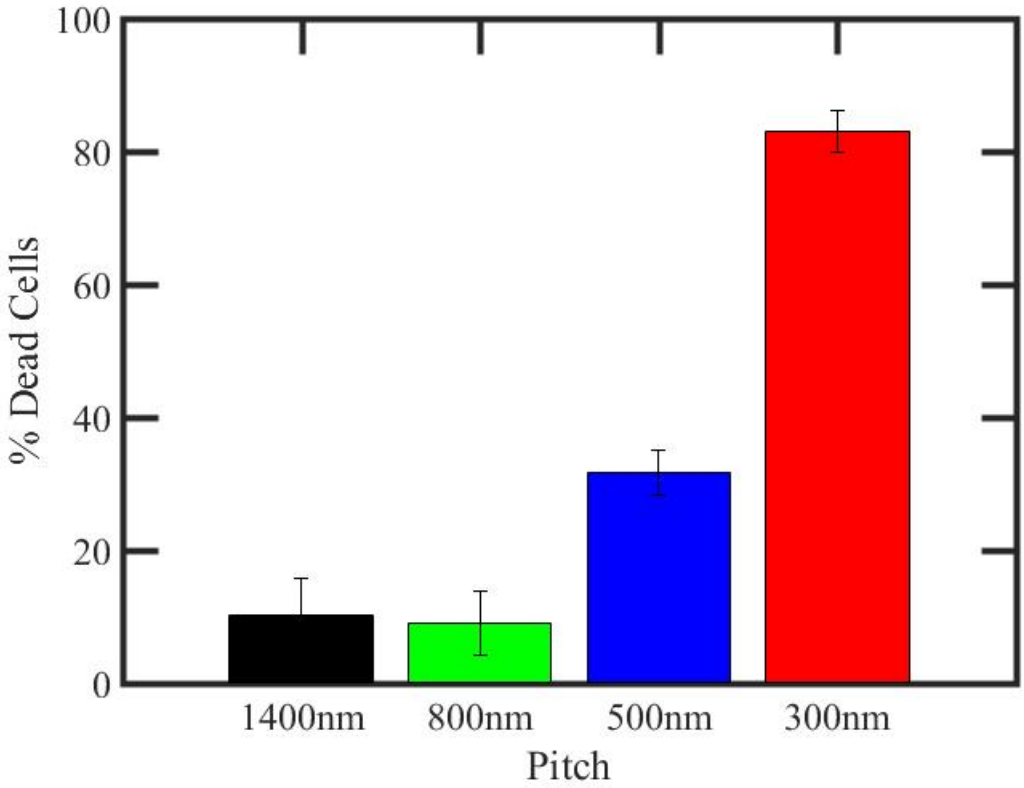

Figure 32: Percentage of dead cells after 3 hour incubation of *S. epidermidis* on fabricated bacteridial samples. Error bars indicate standard error.

cell by the nanostructures of 300 nm pitch samples, the membrane is teared. The top surface of the spherical cell is flattened and lysis is observed. As a result of that significant killing is observed for the 300 nm pitch samples at the 3 hour time point, compared to that of the 500 nm pitch sample. SEM images in Figure 33 shows severely deformed lysed *S. epidermidis* cells observed on the 300 nm sample. These SEM images suggest the cytoplasmic materials inside the bacterial cell comes out after interaction with the nanpstructures, as the bacteria cells look completely flattened compared to their original spherical shape. The deformation and death of cells is evident from these images, as the flattened cells looks very much different compared to viable spherical *S. epidermidis*. 500 nm pitch samples, for which lesser amount of bactericidal performance was observed, can be seen in Figure 34a, and 34b. While many

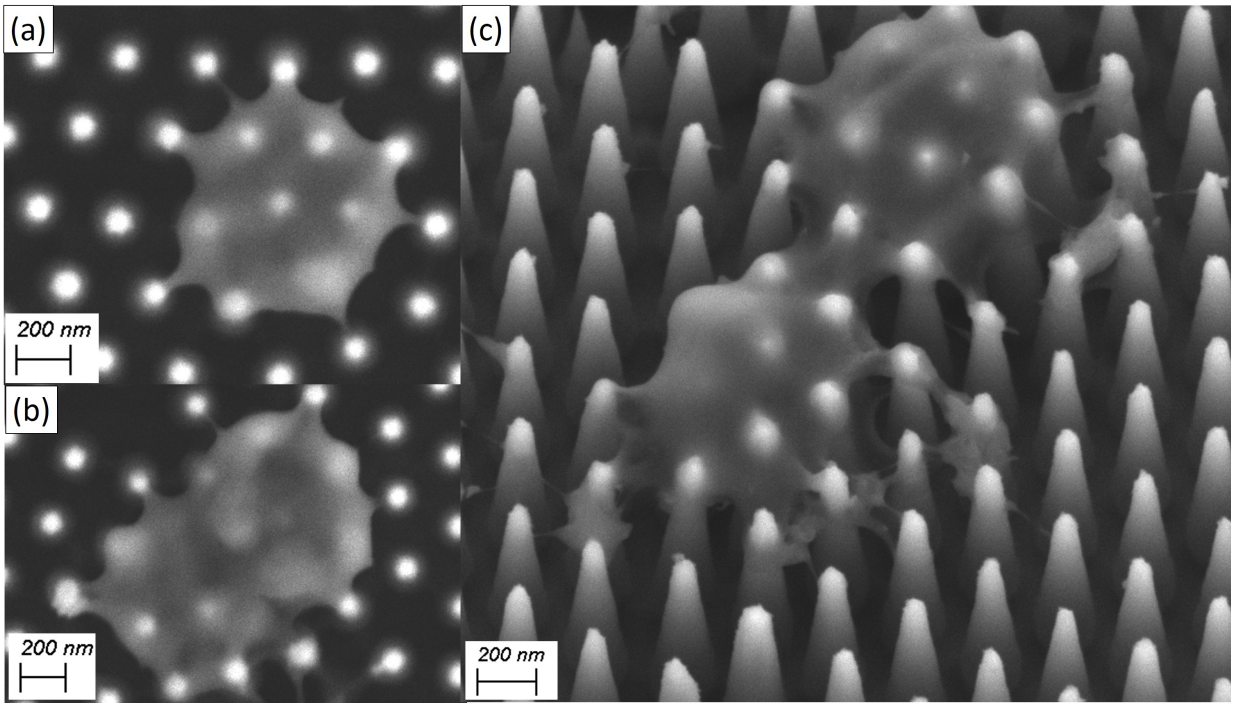

Figure 33: SEM image of punctured bacteria cell on 300 nm pitch samples. (a,b) top view, (c) tilted view.

cells appeared viable and spherical, pore formation was observed for some bacteria cells. The similar effect was observed when bacteria cells were treated by ultrasound by Li *et al.* [230]. The SEM images of the 500 nm pitch samples with bacteria after pore formation in our study resembles their findings. The difference between the 300 nm and 500 nm pitch samples is that flattening of cell is not observed for the 500 nm pitch samples. That might be attributed to the difference in density of the nanostructures in these substrates.

5.5 Conclusion

SiNC substrates were fabricated by deep reactive ion etching. The height, pitch, top diameter of these structures were controlled. The bactericidal effect of these structures were

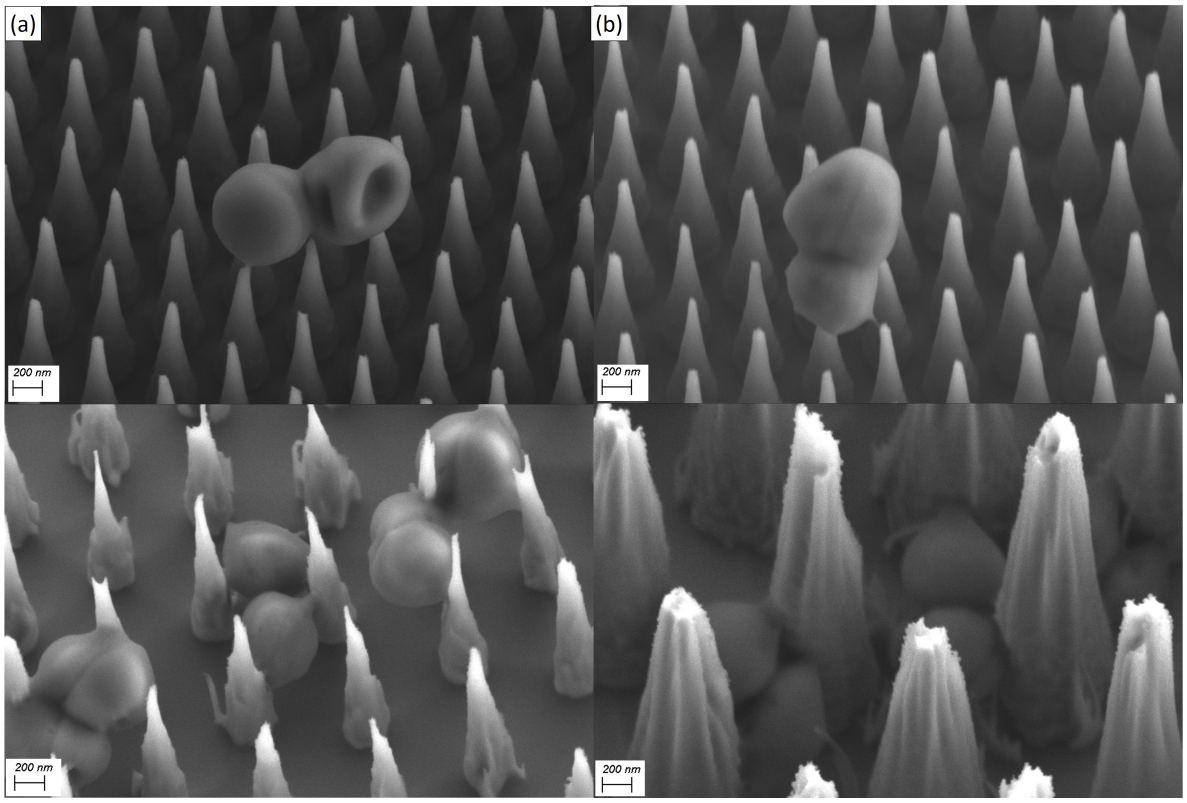

Figure 34: Tilted view SEM image of bacteria cell on different samples.
(a,b) 500 nm, (c) 800 nm, (d) 1400 nm pitch samples.

tested against the Gram-positive bacteria, *S. epidermidis*. Gram-positive bacteria have a thicker cell wall compared to Gram-negative bacteria, and has been reported difficult to kill mechanically. SEM images revealed that the bacteria cells could sit in between the structures on samples with larger pitch, but not for the samples with smaller pitch. 300 nm pitch samples had the best results with bacterial killing of 82% at the three hour time point. As the bacteria cells develop resistance to drugs, these results provide insights towards an alternative approach to encounter this phenomenon.

6.0 Conclusions and prospects

Micro/nanostructured materials are quite useful due to their unique chemical, physical, and mechanical properties. In my work, I focused on simulation studies as well as the fabrication of micro/nanostructured materials materials to improve device performance. Our finite difference time domain simulation results showed that the absorption enhancement in vertical nanowire arrays over silicon thin films can be further improved through tilted nanowires. Tilted nanowire arrays exhibit improved absorption over the infrared, visible, and ultraviolet regime compared with vertical nanowires since the tilt removes symmetry requirements on the resonance modes in the nanowires. Incorporation of these structures could improve the efficiency of solar cells. We successfully fabricated wafer scale silicon nanopillar structures with different geometries. By using nanopillars with systematically varying heights on silicon substrates, we demonstrated scalable boiling enhancement with increasing height of nanopillars. Increasing the height of nanopillars effectively resulted in considerable enhancement of both heat flux and surface temperature at CHF. We attribute such enhancement to the nanopillar-induced increase in rewetting velocity.

We fabricated of micro/nanostructured materials with anti-biofouling and bactericidal properties. We reported on the micro-/nanostructuring and surface functionalization of PP substrates through various oxygen and fluorine reactive ion etching (RIE) treatments and their effects on wettability and bacteria adhesion. We found that oxygen treatment creates a hydrophilic surface that reduces bacteria adhesion compared to the control, but additional nanostructuring reduces the surface's anti-biofouling properties due to increased microscale roughness and air pockets that reduce the effectiveness of the liquid barrier. Our best samples were prepared by a fluorine etch chemistry may be utilized to create lotus leaf-inspired, low surface energy, hierarchical micro-structure/nanofibrils in PP. Due to the low surface energy and hierarchical morphology, the surface exhibits lotus-leaf wetting (high contact angle and low contact angle hysteresis) where water droplets easily roll off the surface in contrast to other PP samples. The lotus leaf-inspired hierarchical, fluorinated surfaces exhibit a 99.6% reduction of *E. coli* cell adhesion compared to untreated PP.

We then fabricated bactericidal surfaces consisting of uniform and regular nanostructured arrays. The pitch, diameter, taper, and height of the nanostructures are controlled. The bactericidal effect of these structures were investigated against Gram-positive bacteria (*S. epidermidis*). Gram-positive bacteria have a thicker cell wall compared to Gram-negative bacteria, and has been reported difficult to kill mechanically. Our results shows that the center-to-center spacing among the pillars plays an important role in the bactericidal performance of the substrate. Significant enhancement in killing was observed for 1μm long, 300 nm pitch nanostructured surface with a tip diameter of 80 nm compared to the flat control substrates.

While our results are promising, there are still room for improvement. Increasing the height of nanopillars effectively resulted in considerable enhancement of both heat flux and surface temperature at CHF within the range of the heights we studied. However, there remains a question regarding the range of heights for which this effect would continue. As the spreading velocity might not increase indefinitely due to the competing effect of contact line friction with the increase of height of nanopillars. Similarly, the bactericidal results form our study can be used to fabricate improved nanostructured surfaces to exhibit complete killing of bacteria cells.

Appendix

A. Tilted Silicon Nanowire Array Simulation

We also studied the similar properties of the 500 nm long nanowires. The pitch a was varied from 40 nm to 1000 nm and the diameter d was also varied from 20 nm up to the pitch. The highest efficiency was obtained for 680 nm pitch and 640 nm diameter. The increase

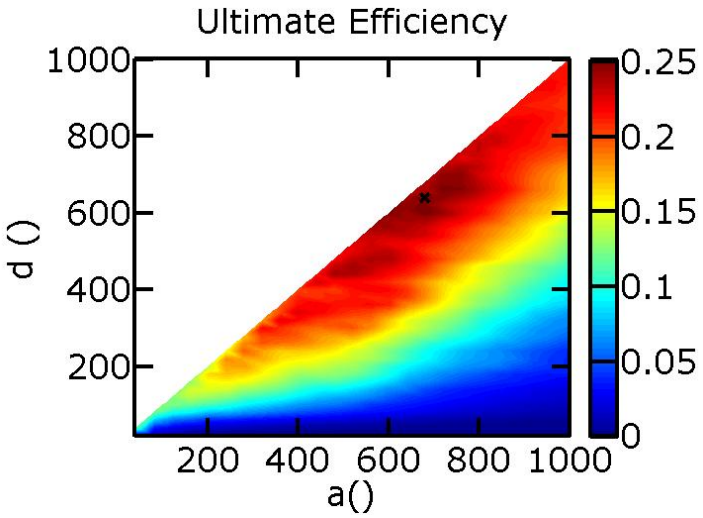

Figure 35: Ultimate efficiency of square arrays of vertical nanowires. The vertical nanowires ($\alpha = 0$) have height $h = 500$ nm and the ultimate efficiency is shown as a function of array pitch a and nanowire diameter d. The highest ultimate efficiency is at $a = 680$ nm, $d = 640$ nm, which is marked in the contour plot.

in efficiency for the 500 nm long nanowires was less than that of 1000 nm long nanowires. We also did the simulation study of the 500nm long tilted nanowires. At 72.8^0 tilt angle the efficiency was maximum and the increase in efficiency was 6.47% compared to vertical ones.

Bibliography

[1] B. S. Murty, P. Shankar, B. Raj, B. B. Rath, and J. Murday, *Applications of Nanomaterials*. Berlin, Heidelberg: Springer Berlin Heidelberg, 2013, pp. 107–148. [Online]. Available: https://doi.org/10.1007/978-3-642-28030-6_4

[2] N. Govindaraju and R. Singh, "Synthesis and properties of boron nitride nanotubes," in *Nanotube Superfiber Materials*. Elsevier, 2014, pp. 243–265.

[3] D. Gong, C. A. Grimes, O. K. Varghese, W. Hu, R. Singh, Z. Chen, and E. C. Dickey, "Titanium oxide nanotube arrays prepared by anodic oxidation," *Journal of Materials Research*, vol. 16, no. 12, pp. 3331–3334, 2001.

[4] O. K. Varghese, D. Gong, M. Paulose, C. A. Grimes, and E. C. Dickey, "Crystallization and high-temperature structural stability of titanium oxide nanotube arrays," *Journal of Materials Research*, vol. 18, no. 1, pp. 156–165, 2003.

[5] R. Fan, Y. Wu, D. Li, M. Yue, A. Majumdar, and P. Yang, "Fabrication of silica nanotube arrays from vertical silicon nanowire templates," *Journal of the American Chemical Society*, vol. 125, no. 18, pp. 5254–5255, 2003.

[6] Z. L. Wang, R. P. Gao, J. L. Gole, and J. D. Stout, "Silica nanotubes and nanofiber arrays," *Advanced Materials*, vol. 12, no. 24, pp. 1938–1940, 2000.

[7] M.-H. Park, M. G. Kim, J. Joo, K. Kim, J. Kim, S. Ahn, Y. Cui, and J. Cho, "Silicon nanotube battery anodes," *Nano letters*, vol. 9, no. 11, pp. 3844–3847, 2009.

[8] H. Wu, G. Chan, J. W. Choi, I. Ryu, Y. Yao, M. T. McDowell, S. W. Lee, A. Jackson, Y. Yang, L. Hu *et al.*, "Stable cycling of double-walled silicon nanotube battery anodes through solid–electrolyte interphase control," *Nature nanotechnology*, vol. 7, no. 5, p. 310, 2012.

[9] R. H. Baughman, A. A. Zakhidov, and W. A. De Heer, "Carbon nanotubes–the route toward applications," *science*, vol. 297, no. 5582, pp. 787–792, 2002.

[10] J. Wang, "Carbon-nanotube based electrochemical biosensors: A review," *Electroanalysis: An International Journal Devoted to Fundamental and Practical Aspects of Electroanalysis*, vol. 17, no. 1, pp. 7–14, 2005.

[11] Y. Yan, J. Miao, Z. Yang, F.-X. Xiao, H. Bin Yang, B. Liu, and Y. Yang, "Carbon nanotube catalysts: recent advances in synthesis, characterization and applications," *Chemical Society Reviews*, vol. 44, no. 10, pp. 3295–3346, 2015. [Online]. Available: https://pubs.rsc.org/en/content/articlelanding/2015/cs/c4cs00492b

[12] J. N. Coleman, U. Khan, W. J. Blau, and Y. K. Gunko, "Small but strong: A review of the mechanical properties of carbon nanotubepolymer composites," *Carbon*, vol. 44, no. 9, pp. 1624–1652, Aug. 2006. [Online]. Available: http://www.sciencedirect.com/science/article/pii/S0008622306001229

[13] G. K. Mor, O. K. Varghese, M. Paulose, K. Shankar, and C. A. Grimes, "A review on highly ordered, vertically oriented tio2 nanotube arrays: Fabrication, material properties, and solar energy applications," *Solar Energy Materials and Solar Cells*, vol. 90, no. 14, pp. 2011–2075, 2006.

[14] A. N. Shipway, E. Katz, and I. Willner, "Nanoparticle Arrays on Surfaces for Electronic, Optical, and Sensor Applications," *ChemPhysChem*, vol. 1, no. 1, pp. 18–52, Aug. 2000. [Online]. Available: https://onlinelibrary.wiley.com/doi/abs/10.1002/1439-7641%2820000804%291%3A1%3C18%3A%3AAID-CPHC18%3E3.0.CO%3B2-L

[15] T. M. Tolaymat, A. M. El Badawy, A. Genaidy, K. G. Scheckel, T. P. Luxton, and M. Suidan, "An evidence-based environmental perspective of manufactured silver nanoparticle in syntheses and applications: a systematic review and critical appraisal of peer-reviewed scientific papers," *Science of the total environment*, vol. 408, no. 5, pp. 999–1006, 2010.

[16] M.-J. Yoon, "Surface modifications and optoelectronic characterization of tio2-nanoparticles: Design of new photo-electronic materials," *Journal of the Chinese Chemical Society*, vol. 56, no. 3, pp. 449–454, 2009.

[17] P. I. Gouma and J. Lee, "Photocatalytic nanomats clean up produced water from fracking," *Translational Materials Research*, vol. 1, no. 2, p. 025002, 2014. [Online]. Available: http://stacks.iop.org/2053-1613/1/i=2/a=025002

[18] M. De, P. S. Ghosh, and V. M. Rotello, "Applications of nanoparticles in biology," *Advanced Materials*, vol. 20, no. 22, pp. 4225–4241, 2008.

[19] M. Ahamed, M. S. AlSalhi, and M. K. J. Siddiqui, "Silver nanoparticle applications and human health," *Clinica Chimica Acta*, vol. 411, no. 23, pp. 1841–1848, Dec. 2010. [Online]. Available: http://www.sciencedirect.com/science/article/pii/S0009898110005139

[20] H. Aldewachi, T. Chalati, M. Woodroofe, N. Bricklebank, B. Sharrack, and P. Gardiner, "Gold nanoparticle-based colorimetric biosensors," *Nanoscale*, vol. 10, no. 1, pp. 18–33, 2018.

[21] P. Ghosh, G. Han, M. De, C. K. Kim, and V. M. Rotello, "Gold nanoparticles in delivery applications," *Advanced drug delivery reviews*, vol. 60, no. 11, pp. 1307–1315, 2008.

[22] A. Deepak, A. K. Goyal, and G. Rath, "Nanofiber in transmucosal drug delivery," *Journal of Drug Delivery Science and Technology*, vol. 43, pp. 379–387, 2018.

[23] M. Nasrollahzadeh, Z. Issaabadi, M. Sajjadi, S. M. Sajadi, and M. Atarod, "Types of nanostructures," in *Interface Science and Technology*. Elsevier, 2019, vol. 28, pp. 29–80.

[24] A. Haider, S. Haider, and I.-K. Kang, "A comprehensive review summarizing the effect of electrospinning parameters and potential applications of nanofibers in biomedical and biotechnology," *Arabian Journal of Chemistry*, vol. 11, no. 8, pp. 1165–1188, Dec. 2018. [Online]. Available: http://www.sciencedirect.com/science/article/pii/S1878535215003275

[25] C. Chang, V. H. Tran, J. Wang, Y.-K. Fuh, and L. Lin, "Direct-Write Piezoelectric Polymeric Nanogenerator with High Energy Conversion Efficiency," Jan. 2010. [Online]. Available: https://pubs.acs.org/doi/abs/10.1021/nl9040719

[26] S. P. Miguel, D. R. Figueira, D. Simões, M. P. Ribeiro, P. Coutinho, P. Ferreira, and I. J. Correia, "Electrospun polymeric nanofibres as wound dressings: a review," *Colloids and surfaces B: Biointerfaces*, vol. 169, pp. 60–71, 2018.

[27] A. Paleo, P. Staiti, A. Brigandì, F. Ferreira, A. Rocha, and F. Lufrano, "Supercapacitors based on ac/mno2 deposited onto dip-coated carbon nanofiber cotton fabric electrodes," *Energy Storage Materials*, vol. 12, pp. 204–215, 2018.

[28] Z. He, M. Li, Y. Li, J. Zhu, Y. Jiang, W. Meng, H. Zhou, L. Wang, and L. Dai, "Flexible electrospun carbon nanofiber embedded with tio2 as excellent negative electrode for vanadium redox flow battery," *Electrochimica Acta*, vol. 281, pp. 601–610, 2018.

[29] E. Azwar, W. A. W. Mahari, J. H. Chuah, D.-V. N. Vo, N. L. Ma, W. H. Lam, and S. S. Lam, "Transformation of biomass into carbon nanofiber for supercapacitor application–a review," *International Journal of Hydrogen Energy*, vol. 43, no. 45, pp. 20 811–20 821, 2018.

[30] X. Zhao, X. Ma, and P. Zheng, "The preparation of carboxylic-functional carbon-based nanofibers for the removal of cationic pollutants," *Chemosphere*, vol. 202, pp. 298–305, 2018.

[31] K.-Q. Peng, X. Wang, X.-L. Wu, and S.-T. Lee, "Platinum nanoparticle decorated silicon nanowires for efficient solar energy conversion," *Nano letters*, vol. 9, no. 11, pp. 3704–3709, 2009.

[32] X. Duan, C. Niu, V. Sahi, J. Chen, J. W. Parce, S. Empedocles, and J. L. Goldman, "High-performance thin-film transistors using semiconductor nanowires and nanoribbons," *Nature*, vol. 425, no. 6955, p. 274, 2003.

[33] C. Fang, A. Agarwal, E. Widjaja, M. V. Garland, S. M. Wong, L. Linn, N. M. Khalid, S. M. Salim, and N. Balasubramanian, "Metallization of silicon nanowires and sers response from a single metallized nanowire," *Chemistry of Materials*, vol. 21, no. 15, pp. 3542–3548, 2009.

[34] J. Li and L.-W. Wang, "First principle study of core/shell structure quantum dots," *Applied physics letters*, vol. 84, no. 18, pp. 3648–3650, 2004.

[35] G.-J. Zhang, G. Zhang, J. H. Chua, R.-E. Chee, E. H. Wong, A. Agarwal, K. D. Buddharaju, N. Singh, Z. Gao, and N. Balasubramanian, "Dna sensing by silicon nanowire: charge layer distance dependence," *Nano letters*, vol. 8, no. 4, pp. 1066–1070, 2008.

[36] S. Su, Y. He, S. Song, D. Li, L. Wang, C. Fan, and S.-T. Lee, "A silicon nanowire-based electrochemical glucose biosensor with high electrocatalytic activity and sensitivity," *Nanoscale*, vol. 2, no. 9, pp. 1704–1707, 2010.

[37] S. Su, Y. He, M. Zhang, K. Yang, S. Song, X. Zhang, C. Fan, and S.-T. Lee, "High-sensitivity pesticide detection via silicon nanowires-supported acetylcholinesterase-

based electrochemical sensors," *Applied Physics Letters*, vol. 93, no. 2, p. 023113, 2008.

[38] F. Patolsky, G. Zheng, and C. M. Lieber, "Fabrication of silicon nanowire devices for ultrasensitive, label-free, real-time detection of biological and chemical species," *Nature protocols*, vol. 1, no. 4, p. 1711, 2006.

[39] D.-Y. Jeon, S. Pregl, S. J. Park, L. Baraban, G. Cuniberti, T. Mikolajick, and W. M. Weber, "Scaling and graphical transport-map analysis of ambipolar schottky-barrier thin-film transistors based on a parallel array of si nanowires," *Nano letters*, vol. 15, no. 7, pp. 4578–4584, 2015.

[40] Y. Wang, N. Lu, H. Xu, G. Shi, M. Xu, X. Lin, H. Li, W. Wang, D. Qi, Y. Lu *et al.*, "Biomimetic corrugated silicon nanocone arrays for self-cleaning antireflection coatings," *Nano Research*, vol. 3, no. 7, pp. 520–527, 2010.

[41] S. Jeong, E. C. Garnett, S. Wang, Z. Yu, S. Fan, M. L. Brongersma, M. D. McGehee, and Y. Cui, "Hybrid silicon nanocone–polymer solar cells," *Nano letters*, vol. 12, no. 6, pp. 2971–2976, 2012.

[42] J. N. Tiwari, T.-M. Chen, F.-M. Pan, and K.-L. Lin, "Ordered silicon nanocones as a highly efficient platinum catalyst support for direct methanol fuel cells," *Journal of Power Sources*, vol. 182, no. 2, pp. 510–514, 2008.

[43] S. Choi, "Microscale microbial fuel cells: advances and challenges," *Biosensors and Bioelectronics*, vol. 69, pp. 8–25, 2015.

[44] C. Wang, F. Luo, H. Lu, X. Rong, B. Liu, G. Chu, Y. Sun, B. Quan, J. Zheng, J. Li *et al.*, "A well-defined silicon nanocone–carbon structure for demonstrating exclusive influences of carbon coating on silicon anode of lithium-ion batteries," *ACS applied materials & interfaces*, vol. 9, no. 3, pp. 2806–2814, 2017.

[45] M. Kulkarni, A. Mazare, E. Gongadze, Š. Perutkova, V. Kralj-Iglič, I. Milošev, P. Schmuki, A. Iglič, and M. Mozetič, "Titanium nanostructures for biomedical applications," *Nanotechnology*, vol. 26, no. 6, p. 062002, 2015.

[46] N. Mitik-Dineva, J. Wang, V. K. Truong, P. Stoddart, F. Malherbe, R. J. Crawford, and E. P. Ivanova, "Escherichia coli, pseudomonas aeruginosa, and staphylococcus aureus attachment patterns on glass surfaces with nanoscale roughness," *Current microbiology*, vol. 58, no. 3, pp. 268–273, 2009.

[47] L. Tsakalakos, J. Balch, J. Fronheiser, B. A. Korevaar, O. Sulima, and J. Rand, "Silicon nanowire solar cells," *Applied Physics Letters*, vol. 91, no. 23, p. 233117, Dec. 2007. [Online]. Available: https://aip.scitation.org/doi/full/10.1063/1.2821113

[48] E. C. Garnett, M. L. Brongersma, Y. Cui, and M. D. McGehee, "Nanowire Solar Cells," *Annual Review of Materials Research*, vol. 41, no. 1, pp. 269–295, 2011. [Online]. Available: https://doi.org/10.1146/annurev-matsci-062910-100434

[49] J. Lee, P. Lee, H. Lee, D. Lee, S. Seob Lee, and S. Hwan Ko, "Very long Ag nanowire synthesis and its application in a highly transparent, conductive and flexible metal electrode touch panel," *Nanoscale*, vol. 4, no. 20, pp. 6408–6414, 2012. [Online]. Available: https://pubs.rsc.org/en/content/articlelanding/2012/nr/c2nr31254a

[50] T. Muraliganth, A. V. Murugan, and A. Manthiram, "Facile synthesis of carbon-decorated single-crystalline Fe3o4 nanowires and their application as high performance anode in lithium ion batteries," *Chemical Communications*, vol. 0, no. 47, pp. 7360–7362, 2009. [Online]. Available: https://pubs.rsc.org/en/content/articlelanding/2009/cc/b916376j

[51] Q. Wan and T. H. Wang, "Single-crystalline Sb-doped SnO 2 nanowires : synthesis and gas sensor application," *Chemical Communications*, vol. 0, no. 30, pp. 3841–3843, 2005. [Online]. Available: https://pubs.rsc.org/en/content/articlelanding/2005/cc/b504094a

[52] S.-J. Bao, C. M. Li, C.-X. Guo, and Y. Qiao, "Biomolecule-assisted synthesis of cobalt sulfide nanowires for application in supercapacitors," *Journal of Power Sources*, vol. 180, no. 1, pp. 676–681, May 2008. [Online]. Available: http://www.sciencedirect.com/science/article/pii/S0378775308002218

[53] J. Liang, L. Li, K. Tong, Z. Ren, W. Hu, X. Niu, Y. Chen, and Q. Pei, "Silver Nanowire Percolation Network Soldered with Graphene Oxide at Room Temperature and Its Application for Fully Stretchable Polymer Light-Emitting Diodes," *ACS Nano*, vol. 8, no. 2, pp. 1590–1600, Feb. 2014. [Online]. Available: https://doi.org/10.1021/nn405887k

[54] B. Zhou, Y. Li, G. Zheng, K. Dai, C. Liu, Y. Ma, J. Zhang, N. Wang, C. Shen, and Z. Guo, "Continuously fabricated transparent conductive polycarbonate/carbon nanotube nanocomposite films for switchable thermochromic applications," *Journal of Materials Chemistry C*, vol. 6, no. 31, pp. 8360–8371, 2018.

[55] G. Sharma, B. Thakur, M. Naushad, A. Kumar, F. J. Stadler, S. M. Alfadul, and G. T. Mola, "Applications of nanocomposite hydrogels for biomedical engineering and environmental protection," *Environmental chemistry letters*, vol. 16, no. 1, pp. 113–146, 2018.

[56] Y. Ma, D. Bai, X. Hu, N. Ren, W. Gao, S. Chen, H. Chen, Y. Lu, J. Li, and Y. Bai, "Robust and antibacterial polymer/mechanically exfoliated graphene nanocomposite fibers for biomedical applications," *ACS applied materials & interfaces*, vol. 10, no. 3, pp. 3002–3010, 2018.

[57] X. Zhao, B. Guo, H. Wu, Y. Liang, and P. X. Ma, "Injectable antibacterial conductive nanocomposite cryogels with rapid shape recovery for noncompressible hemorrhage and wound healing," *Nature communications*, vol. 9, no. 1, p. 2784, 2018.

[58] A. M. Amanulla, S. J. Shahina, R. Sundaram, C. M. Magdalane, K. Kaviyarasu, D. Letsholathebe, S. Mohamed, J. Kennedy, and M. Maaza, "Antibacterial, magnetic, optical and humidity sensor studies of β-comoo4-co3o4 nanocomposites and its synthesis and characterization," *Journal of Photochemistry and Photobiology B: Biology*, vol. 183, pp. 233–241, 2018.

[59] Z. Yang, X. Hao, S. Chen, Z. Ma, W. Wang, C. Wang, L. Yue, H. Sun, Q. Shao, V. Murugadoss *et al.*, "Long-term antibacterial stable reduced graphene oxide nanocomposites loaded with cuprous oxide nanoparticles," *Journal of colloid and interface science*, vol. 533, pp. 13–23, 2019.

[60] S. Dhanavel, N. Manivannan, N. Mathivanan, V. K. Gupta, V. Narayanan, and A. Stephen, "Preparation and characterization of cross-linked chitosan/palladium nanocomposites for catalytic and antibacterial activity," *Journal of Molecular Liquids*, vol. 257, pp. 32–41, 2018.

[61] M.-C. Lu, C.-H. Huang, C.-T. Huang, and Y.-C. Chen, "A modified hydrodynamic model for pool boiling chf considering the effects of heater size and nucleation site density," *International Journal of Thermal Sciences*, vol. 91, pp. 133–141, 2015.

[62] N. S. Dhillon, J. Buongiorno, and K. K. Varanasi, "Critical heat flux maxima during boiling crisis on textured surfaces," *Nature communications*, vol. 6, p. 8247, 2015.

[63] M. Shojaeian and A. Koşar, "Pool boiling and flow boiling on micro-and nanostructured surfaces," *Experimental Thermal and Fluid Science*, vol. 63, pp. 45–73, 2015.

[64] S. H. Kim, G. C. Lee, J. Y. Kang, K. Moriyama, M. H. Kim, and H. S. Park, "Boiling heat transfer and critical heat flux evaluation of the pool boiling on micro structured surface," *International Journal of Heat and Mass Transfer*, vol. 91, pp. 1140–1147, 2015.

[65] W. Fang, H.-Y. Guo, B. Li, Q. Li, and X.-Q. Feng, "Revisiting the critical condition for the cassie–wenzel transition on micropillar-structured surfaces," *Langmuir*, vol. 34, no. 13, pp. 3838–3844, 2018.

[66] F. Yang, S. Cheng, X. Zhang, X. Ren, R. Li, H. Dong, and W. Hu, "2d organic materials for optoelectronic applications," *Advanced Materials*, vol. 30, no. 2, p. 1702415, 2018.

[67] X. Yang, J. Wu, T. Liu, and R. Zhu, "Patterned perovskites for optoelectronic applications," *Small Methods*, vol. 2, no. 10, p. 1800110, 2018.

[68] Y. Luo, J. Shao, S. Chen, X. Chen, H. Tian, X. Li, L. Wang, D. Wang, and B. Lu, "Flexible capacitive pressure sensor enhanced by tilted micropillar arrays," *ACS applied materials & interfaces*, 2019.

[69] Y. Zhang, Z. Fan, W. Zhang, Q. Ma, Z. Jiang, and D. Ma, "High performance hybrid silicon micropillar solar cell based on light trapping characteristics of cu nanoparticles," *AIP Advances*, vol. 8, no. 5, p. 055309, 2018.

[70] F. Wu, H. Lin, Z. Yang, M. Liao, Z. Wang, Z. Li, P. Gao, J. Ye, and W. Shen, "Suppression of surface and auger recombination by formation and control of radial junction in silicon microwire solar cells," *Nano Energy*, vol. 58, pp. 817–824, 2019.

[71] V. K. Singh, J. Nagaraju, and S. Avasthi, "Radial junction silicon solar cells with micro-pillar array and planar electrode interface for improved photon management and carrier extraction," *Current Applied Physics*, vol. 19, no. 3, pp. 341–346, 2019.

[72] S.-S. Yoon and D.-Y. Khang, "Stretchable, bifacial si-organic hybrid solar cells by vertical array of si micropillars embedded into elastomeric substrates," *ACS applied materials & interfaces*, vol. 11, no. 3, pp. 3290–3298, 2018.

[73] M. I. Kayes and P. W. Leu, "Comparative study of absorption in tilted silicon nanowire arrays for photovoltaics," *Nanoscale Research Letters*, vol. 9, no. 1, November 2014. [Online]. Available: http://www.nanoscalereslett.com/content/9/1/620

[74] T.-B. Nguyen, D. Liu, M. I. Kayes, B. Wang, N. Rashin, P. W. Leu, and T. Tran, "Critical heat flux enhancement in pool boiling through increased rewetting on nanopillar array surfaces," *Scientific reports*, vol. 8, no. 1, p. 4815, 2018.

[75] M. I. Kayes, A. J. Galante, N. A. Stella, S. Haghanifar, R. M. Shanks, and P. W. Leu, "Stable lotus leaf-inspired hierarchical, fluorinated polypropylene surfaces for reduced bacterial adhesion," *Reactive and Functional Polymers*, vol. 128, pp. 40–46, 2018.

[76] N. Feng, J. Michel, L. Zeng, J. Liu, C. Hong, L. Kimerling, and X. Duan, "Design of highly efficient light-trapping structures for thin-film crystalline silicon solar cells," *Electron Devices, IEEE Transactions on*, vol. 54, no. 8, pp. 1926–1933, 2007. [Online]. Available: http://ieeexplore.ieee.org/xpls/abs_all.jsp?arnumber=4277956

[77] H. Stiebig, N. Senoussaoui, C. Zahren, C. Haase, and J. Müller, "Silicon thin-film solar cells with rectangular-shaped grating couplers," *Progress in Photovoltaics: Research and Applications*, vol. 14, no. 1, pp. 13–24, 2006. [Online]. Available: http://dx.doi.org/10.1002/pip.638

[78] P. Bermel, C. Luo, L. Zeng, L. C. Kimerling, and J. D. Joannopoulos, "Improving thin-film crystalline silicon solar cell efficiencies with photonic crystals," *Opt. Express*, vol. 15, no. 25, pp. 16 986–17 000, Dec 2007. [Online]. Available: http://www.opticsexpress.org/abstract.cfm?URI=oe-15-25-16986

[79] A. Chutinan and S. John, "Light trapping and absorption optimization in certain thin-film photonic crystal architectures," *Phys. Rev. A*, vol. 78, p. 023825, Aug 2008. [Online]. Available: http://link.aps.org/doi/10.1103/PhysRevA.78.023825

[80] D. Zhou and R. Biswas, "Photonic crystal enhanced light-trapping in thin film solar cells," *Journal of Applied Physics*, vol. 103, no. 9, p. 093102, 2008. [Online]. Available: https://aip.scitation.org/doi/10.1063/1.2908212

[81] S. B. Mallick, M. Agrawal, and P. Peumans, "Optimal light trapping in ultra-thin photonic crystal crystalline silicon solar cells," *Opt. Express*, vol. 18, no. 6, pp. 5691–5706, Mar 2010. [Online]. Available: http://www.opticsexpress.org/abstract.cfm?URI=oe-18-6-5691

[82] C. Rockstuhl, S. Fahr, K. Bittkau, T. Beckers, R. Carius, F. Haug, T. Söderström, C. Ballif, and F. Lederer, "Comparison and optimization of randomly textured surfaces in thin-film solar cells," *Optics Express*, vol. 18, no. S3, pp. A335–A341, 2010. [Online]. Available: http://www.opticsexpress.org/abstract.cfm?URI=oe-18-103-A335

[83] C. Hsu, G. F. Burkhard, M. D. McGehee, and Y. Cui, "Effects of nanostructured back reflectors on the external quantum efficiency in thin film solar cells," *Nano Research*, vol. 4, pp. 153–158, Nov. 2010. [Online]. Available: http://www.springerlink.com/content/4677176p38105363/

[84] E. Yablonovitch and G. Cody, "Intensity enhancement in textured optical sheets for solar cells," *Electron Devices, IEEE Transactions on*, vol. 29, no. 2, pp. 300–305, 1982. [Online]. Available: http://ieeexplore.ieee.org/xpls/abs_all.jsp?arnumber=1482197&tag=1

[85] E. Yablonovitch, "Statistical ray optics," *Journal of the Optical Society of America*, vol. 72, no. 7, pp. 899–907, Jul. 1982. [Online]. Available: http://www.opticsinfobase.org/abstract.cfm?URI=josa-72-7-899

[86] M. D. Kelzenberg, S. W. Boettcher, J. A. Petykiewicz, D. B. Turner-Evans, M. C. Putnam, E. L. Warren, J. M. Spurgeon, R. M. Briggs, N. S. Lewis, and H. A. Atwater, "Enhanced absorption and carrier collection in Si wire arrays for photovoltaic applications," *Nat Mater*, vol. 9, no. 3, pp. 239–244, Mar. 2010. [Online]. Available: http://dx.doi.org/10.1038/nmat2635

[87] Y. Lin, A. Harb, K. Lozano, D. Xu, and K. P. Chen, "Five beam holographic lithography for simultaneous fabrication of three dimensional photonic crystal templates and line defects using phase tunable diffractive optical element," *Optics Express*, vol. 17, no. 19, pp. 16 625–16 631, Sep. 2009. [Online]. Available: http://www.opticsexpress.org/abstract.cfm?URI=oe-17-19-16625

[88] E. Garnett and P. Yang, "Light Trapping in Silicon Nanowire Solar Cells," *Nano Lett.*, vol. 10, no. 3, pp. 1082–1087, Mar. 2010. [Online]. Available: http://dx.doi.org/10.1021/nl100161z

[89] K. Peng, Y. Xu, Y. Wu, Y. Yan, S. Lee, and J. Zhu, "Aligned single-crystalline Si nanowire arrays for photovoltaic applications," *Small*, vol. 1, no. 11, pp. 1062–1067, 2005.

[90] L. Tsakalakos, J. Balch, J. Fronheiser, B. A. Korevaar, O. Sulima, and J. Rand, "Silicon nanowire solar cells," *Appl. Phys. Lett.*, vol. 91, no. 23, p. 233117, 2007.

[91] T. H. Stelzner, M. Pietsch, G. Andrä, F. Falk, E. Ose, and S. Christiansen, "Silicon nanowire-based solar cells," *Nanotechnology*, vol. 19, no. 29, p. 295203, 2008.

[92] G. Yu, X. Li, C. M. Lieber, and A. Cao, "Nanomaterial-incorporated blown bubble films for large-area, aligned nanostructures," *Journal of Materials Chemistry*, vol. 18, no. 7, p. 728, 2008. [Online]. Available: http://pubs.rsc.org/en/Content/ArticleLanding/2008/JM/b713697h

[93] C. Hu, C. Yang, and S. Hu, "Hydrophobic adsorption of surfactants on water-soluble carbon nanotubes: A simple approach to improve sensitivity and antifouling capacity of carbon nanotubes-based electrochemical sensors," *Electrochemistry Communications*, vol. 9, no. 1, pp. 128–134, Jan. 2007. [Online]. Available: http://www.sciencedirect.com/science/article/pii/S1388248106003894

[94] W. Q. Xie, J. I. Oh, and W. Z. Shen, "Realization of effective light trapping and omnidirectional antireflection in smooth surface silicon nanowire arrays," *Nanotechnology*, vol. 22, p. 065704, Feb. 2011. [Online]. Available: http://iopscience.iop.org/0957-4484/22/6/065704

[95] Z. Fan, D. J. Ruebusch, A. A. Rathore, R. Kapadia, O. Ergen, P. W. Leu, and A. Javey, "Challenges and prospects of nanopillar-based solar cells," *Nano Research*, vol. 2, no. 11, pp. 829–843, Nov. 2009. [Online]. Available: http://dx.doi.org/10.1007/s12274-009-9091-y

[96] B. M. Kayes, H. A. Atwater, and N. S. Lewis, "Comparison of the device physics principles of planar and radial p-n junction nanorod solar cells," *Journal of Applied Physics*, vol. 97, no. 11, pp. 114 302–11, 2005. [Online]. Available: http://link.aip.org/link/?JAP/97/114302/1

[97] Z. Fan, H. Razavi, J. won Do, A. Moriwaki, O. Ergen, Y. Chueh, P. W. Leu, J. C. Ho, T. Takahashi, L. A. Reichertz, S. Neale, K. Yu, M. Wu, J. W. Ager, and A. Javey, "Three-dimensional nanopillar-array photovoltaics on low-cost and flexible substrates," *Nature Materials*, vol. 8, no. 8, pp. 648–653, 2009. [Online]. Available: http://dx.doi.org/10.1038/nmat2493

[98] B. Wang and P. W. Leu, "Enhanced absorption in silicon nanocone arrays for photovoltaics," *Nanotechnology*, vol. 23, no. 19, p. 194003, May 2012. [Online]. Available: http://iopscience.iop.org/0957-4484/23/19/194003

[99] K. X. Wang, Z. Yu, V. Liu, Y. Cui, and S. Fan, "Absorption enhancement in ultrathin crystalline silicon solar cells with antireflection and light-trapping nanocone gratings," *Nano Letters*, vol. 12, no. 3, pp. 1616–1619, Mar. 2012, 00057. [Online]. Available: http://dx.doi.org/10.1021/nl204550q

[100] H.-P. Wang, T.-Y. Lin, M.-L. Tsai, W.-C. Tu, M.-Y. Huang, C.-W. Liu, Y.-L. Chueh, and J.-H. He, "Toward Efficient and Omnidirectional n-Type Si Solar Cells: Concurrent Improvement in Optical and Electrical Characteristics by Employing Microscale Hierarchical Structures," *ACS Nano*, vol. 8, no. 3, pp. 2959–2969, Mar. 2014. [Online]. Available: http://dx.doi.org/10.1021/nn500257g

[101] Y. Lin, S. Zhou, S. W. Sheehan, and D. Wang, "Nanonet-based hematite heteronanostructures for efficient solar water splitting," *Journal of the American Chemical Society*, vol. 133, no. 8, pp. 2398–2401, Mar. 2011. [Online]. Available: http://dx.doi.org/10.1021/ja110741z

[102] "Solar spectral irradiance: Air mass 1.5." [Online]. Available: http://rredc.nrel.gov/solar/spectra/am1.5/

[103] W. Shockley and H. J. Queisser, "Detailed balance limit of efficiency of p-n junction solar cells," *Journal of Applied Physics*, vol. 32, no. 3, p. 510, 1961. [Online]. Available: http://link.aip.org/link/JAPIAU/v32/i3/p510/s1&Agg=doi

[104] E. D. Palik, *Handbook of Optical Constants of Solids*. Academic Press, Nov. 1997.

[105] J. Berenger, "A perfectly matched layer for the absorption of electromagnetic waves," *Journal of Computational Physics*, vol. 114, no. 2, pp. 185–200, Oct. 1994. [Online]. Available: http://www.sciencedirect.com/science/article/pii/S0021999184711594

[106] J. Li, H. Yu, S. M. Wong, X. Li, G. Zhang, P. G. Lo, and D. Kwong, "Design guidelines of periodic Si nanowire arrays for solar cell application," *Applied Physics Letters*, vol. 95, no. 24, p. 243113, 2009. [Online]. Available: http://link.aip.org/link/APPLAB/v95/i24/p243113/s1&Agg=doi

[107] B. Wang and P. W. Leu, "Tunable and selective resonant absorption in vertical nanowires," *Optics Letters*, vol. 37, no. 18, pp. 3756–3758, Sep. 2012. [Online]. Available: http://ol.osa.org/abstract.cfm?URI=ol-37-18-3756

[108] X. Fang, C. Y. Zhao, and H. Bao, "Radiative behaviors of crystalline silicon nanowire and nanohole arrays for photovoltaic applications," *Journal of Quantitative Spectroscopy and Radiative Transfer*, vol. 133, pp. 579–588, Jan. 2014, 00000. [Online]. Available: http://www.sciencedirect.com/science/article/pii/S002240731300397X

[109] V. K. Dhir, "Boiling heat transfer," *Annual Review of Fluid Mechanics*, vol. 30, no. 1, pp. 365–401, Jan. 1998. [Online]. Available: https://www.annualreviews.org/doi/10.1146/annurev.fluid.30.1.365

[110] N. Karwa, T. Gambaryan-Roisman, P. Stephan, and C. Tropea, "A hydrodynamic model for subcooled liquid jet impingement at the Leidenfrost condition," *International Journal of Thermal Sciences*, vol. 50, no. 6, pp. 993–1000, Jun. 2011. [Online]. Available: http://www.sciencedirect.com/science/article/pii/S1290072911000305

[111] X. Xu and T. Qian, "Single-bubble dynamics in pool boiling of one-component fluids," *Phys. Rev. E*, vol. 89, p. 063002, Jun 2014. [Online]. Available: https://link.aps.org/doi/10.1103/PhysRevE.89.063002

[112] V. P. Carey, "Liquid vapor phase change phenomena," *CRC Press*, 2018. [Online]. Available: https://www.crcpress.com/Liquid-Vapor-Phase-Change-Phenomena-An-Introduction-to-the-Thermophysics/Carey/p/book/9781591690351

[113] T. G. Theofanous, J. P. Tu, A. T. Dinh, and T. N. Dinh, "The boiling crisis phenomenon: Part I: nucleation and nucleate boiling heat transfer," *Experimental Thermal and Fluid Science*, vol. 26, no. 6, pp. 775–792, Aug. 2002. [Online]. Available: http://www.sciencedirect.com/science/article/pii/S0894177702001929

[114] J. Kim, "Review of nucleate pool boiling bubble heat transfer mechanisms," *International Journal of Multiphase Flow*, vol. 35, no. 12, pp. 1067–1076, Dec. 2009. [Online]. Available: http://www.sciencedirect.com/science/article/pii/S0301932209001311

[115] D. E. Kim, D. I. Yu, D. W. Jerng, M. H. Kim, and H. S. Ahn, "Review of boiling heat transfer enhancement on micro/nanostructured surfaces," *Experimental Thermal and Fluid Science*, vol. 66, pp. 173–196, Sep. 2015. [Online]. Available: http://www.sciencedirect.com/science/article/pii/S0894177715000928

[116] A. R. Betz, J. Jenkins, C.-J. . Kim, and D. Attinger, "Boiling heat transfer on superhydrophilic, superhydrophobic, and superbiphilic surfaces," *International Journal of Heat and Mass Transfer*, vol. 57, no. 2, pp. 733–741, Feb. 2013. [Online]. Available: http://www.sciencedirect.com/science/article/pii/S0017931012008460

[117] T. Laurila, A. Carlson, M. Do-Quang, T. Ala-Nissila, and G. Amberg, "Thermohydrodynamics of boiling in a van der Waals fluid," *Physical Review E*,

vol. 85, no. 2, p. 026320, Feb. 2012. [Online]. Available: https://link.aps.org/doi/10.1103/PhysRevE.85.026320

[118] J. Liu, M. Do-Quang, and G. Amberg, "Thermohydrodynamics of boiling in binary compressible fluids," *Physical Review E*, vol. 92, no. 4, p. 043017, Oct. 2015. [Online]. Available: https://link.aps.org/doi/10.1103/PhysRevE.92.043017

[119] R. Kamatchi and S. Venkatachalapathy, "Parametric study of pool boiling heat transfer with nanofluids for the enhancement of critical heat flux: A review," *International Journal of Thermal Sciences*, vol. 87, pp. 228–240, Jan. 2015. [Online]. Available: http://www.sciencedirect.com/science/article/pii/S1290072914002518

[120] N. S. Dhillon, J. Buongiorno, and K. K. Varanasi, "Critical heat flux maxima during boiling crisis on textured surfaces," *Nature Communications*, vol. 6, p. 8247, Sep. 2015. [Online]. Available: https://www.nature.com/articles/ncomms9247

[121] M. Zupani, M. Steinbcher, P. Gregori, and I. Golobi, "Enhanced pool-boiling heat transfer on laser-made hydrophobic/superhydrophilic polydimethylsiloxane-silica patterned surfaces," *Applied Thermal Engineering*, vol. 91, pp. 288–297, Dec. 2015. [Online]. Available: http://www.sciencedirect.com/science/article/pii/S1359431115008212

[122] M. M. Rahman, J. Pollack, and M. McCarthy, "Increasing Boiling Heat Transfer using Low Conductivity Materials," *Scientific Reports*, vol. 5, p. 13145, Aug. 2015. [Online]. Available: https://www.nature.com/articles/srep13145

[123] P. Xu, Q. Li, and Y. Xuan, "Enhanced boiling heat transfer on composite porous surface," *International Journal of Heat and Mass Transfer*, vol. 80, pp. 107–114, Jan. 2015. [Online]. Available: http://www.sciencedirect.com/science/article/pii/S0017931014007467

[124] B. Tang, R. Zhou, L. Lu, and G. Zhou, "Augmented boiling heat transfer on a copper nanoporous surface and the stability of nano-porosity in a hydrothermal environment," *International Journal of Heat and Mass Transfer*, vol. 90, pp. 979–985, Nov. 2015. [Online]. Available: http://www.sciencedirect.com/science/article/pii/S0017931015007723

[125] D. Zhong, J. Meng, Z. Li, and Z. Guo, "Experimental study of saturated pool boiling from downward facing surfaces with artificial cavities," *Experimental Thermal and Fluid Science*, vol. 68, pp. 442–451, Nov. 2015. [Online]. Available: http://www.sciencedirect.com/science/article/pii/S0894177715001521

[126] ——, "Critical heat flux for downward-facing saturated pool boiling on pin fin surfaces," *International Journal of Heat and Mass Transfer*, vol. 87, pp. 201–211, Aug. 2015. [Online]. Available: http://www.sciencedirect.com/science/article/pii/S0017931015003592

[127] C. H. Li and R. P. Rioux, "Independent and collective roles of surface structures at different length scales on pool boiling heat transfer," *Scientific Reports*, vol. 6, p. 37044, Nov. 2016. [Online]. Available: https://www.nature.com/articles/srep37044

[128] M. M. Rahman, E. lerolu, and M. McCarthy, "Role of Wickability on the Critical Heat Flux of Structured Superhydrophilic Surfaces," *Langmuir*, vol. 30, no. 37, pp. 11 225–11 234, Sep. 2014. [Online]. Available: https://doi.org/10.1021/la5030923

[129] B. S. Kim, G. Choi, S. Shin, T. Gemming, and H. H. Cho, "Nano-inspired fluidic interactivity for boiling heat transfer: impact and criteria," *Scientific Reports*, vol. 6, p. 34348, Oct. 2016. [Online]. Available: https://www.nature.com/articles/srep34348

[130] X. Ye and L. Qi, "Two-dimensionally patterned nanostructures based on monolayer colloidal crystals: controllable fabrication, assembly, and applications," *Nano Today*, vol. 6, no. 6, pp. 608–631, 2011.

[131] J. Yu, C. Geng, L. Zheng, Z. Ma, T. Tan, X. Wang, Q. Yan, and D. Shen, "Preparation of high-quality colloidal mask for nanosphere lithography by a combination of air/water interface self-assembly and solvent vapor annealing," *Langmuir*, vol. 28, no. 34, pp. 12 681–12 689, 2012.

[132] G. D. Moon, T. I. Lee, B. Kim, G. Chae, J. Kim, S. Kim, J.-M. Myoung, and U. Jeong, "Assembled monolayers of hydrophilic particles on water surfaces," *ACS nano*, vol. 5, no. 11, pp. 8600–8612, 2011.

[133] D. Cooke and S. G. Kandlikar, "Pool boiling heat transfer and bubble dynamics over plain and enhanced microchannels," *Journal of Heat Transfer*, vol. 133, no. 5, p. 052902, 2011.

[134] Z. Yao, Y.-W. Lu, and S. Kandlikar, "Effects of nanowire height on pool boiling performance of water on silicon chips," *International Journal of Thermal Sciences*, vol. 50, no. 11, pp. 2084–2090, 2011.

[135] S. Ujereh, T. Fisher, and I. Mudawar, "Effects of carbon nanotube arrays on nucleate pool boiling," *International Journal of Heat and Mass Transfer*, vol. 50, no. 19-20, pp. 4023–4038, 2007.

[136] W. M. Rohsenow, "A method of correlating heat transfer data for surface boiling of liquids," Cambridge, Mass.: MIT Division of Industrial Cooporation,[1951], Tech. Rep., 1951.

[137] N. Zuber, "Hydrodynamic Aspects Of Boiling Heat Transfer (Thesis)," Ramo-Wooldridge Corp., Los Angeles, CA (United States); Univ. of California, Los Angeles, CA (United States), Tech. Rep. AECU-4439, Jun. 1959. [Online]. Available: https://www.osti.gov/biblio/4175511

[138] M. Zupani, M. Moe, P. Gregori, A. Sitar, and I. Golobi, "Evaluation of enhanced nucleate boiling performance through wall-temperature distributions on PDMS-silica coated and non-coated laser textured stainless steel surfaces," *International Journal of Heat and Mass Transfer*, vol. 111, pp. 419–428, Aug. 2017. [Online]. Available: http://www.sciencedirect.com/science/article/pii/S0017931017306488

[139] A. Bejan, "Heat Transfer Handbook." [Online]. Available: https://www.wiley.com/en-us/Heat+Transfer+Handbook-p-9780471390152

[140] H. Nair, H. J. J. Staat, T. Tran, A. v. Houselt, A. Prosperetti, D. Lohse, and C. Sun, "The Leidenfrost temperature increase for impacting droplets on carbon-nanofiber surfaces," *Soft Matter*, vol. 10, no. 13, pp. 2102–2109, Mar. 2014. [Online]. Available: https://pubs.rsc.org/en/content/articlelanding/2014/sm/c3sm52326h

[141] H.-m. Kwon, J. C. Bird, and K. K. Varanasi, "Increasing Leidenfrost point using micro-nano hierarchical surface structures," *Applied Physics Letters*, vol. 103, no. 20, p. 201601, Nov. 2013. [Online]. Available: https://aip.scitation.org/doi/10.1063/1.4828673

[142] H. S. Ahn, N. Sinha, M. Zhang, D. Banerjee, S. Fang, and R. H. Baughman, "Pool Boiling Experiments on Multiwalled Carbon Nanotube (MWCNT) Forests," *Journal of Heat Transfer*, vol. 128, no. 12, pp. 1335–1342, May 2006. [Online]. Available: http://dx.doi.org/10.1115/1.2349511

[143] V. Sathyamurthi, H.-S. Ahn, D. Banerjee, and S. C. Lau, "Subcooled Pool Boiling Experiments on Horizontal Heaters Coated With Carbon Nanotubes," *Journal of Heat Transfer*, vol. 131, no. 7, pp. 071 501–071 501–10, Apr. 2009. [Online]. Available: http://dx.doi.org/10.1115/1.3000595

[144] S. Vemuri and K. J. Kim, "Pool boiling of saturated FC-72 on nano-porous surface," *International Communications in Heat and Mass Transfer*, vol. 32, no. 1, pp. 27–31, Jan. 2005. [Online]. Available: http://www.sciencedirect.com/science/article/pii/S0735193304002003

[145] W. Wu, H. Bostanci, L. C. Chow, Y. Hong, M. Su, and J. P. Kizito, "Nucleate boiling heat transfer enhancement for water and FC-72 on titanium oxide and silicon oxide surfaces," *International Journal of Heat and Mass Transfer*, vol. 53, no. 9, pp. 1773–1777, Apr. 2010. [Online]. Available: http://www.sciencedirect.com/science/article/pii/S0017931010000141

[146] R. Chen, M.-C. Lu, V. Srinivasan, Z. Wang, H. H. Cho, and A. Majumdar, "Nanowires for Enhanced Boiling Heat Transfer," *Nano Letters*, vol. 9, no. 2, pp. 548–553, Feb. 2009. [Online]. Available: https://doi.org/10.1021/nl8026857

[147] S. Launay, A. G. Fedorov, Y. Joshi, A. Cao, and P. M. Ajayan, "Hybrid micro-nano structured thermal interfaces for pool boiling heat transfer enhancement," *Microelectronics Journal*, vol. 37, no. 11, pp. 1158–1164, Nov. 2006. [Online]. Available: http://www.sciencedirect.com/science/article/pii/S002626920500306X

[148] C. Li, Z. Wang, P.-I. Wang, Y. Peles, N. Koratkar, and G. P. Peterson, "Nanostructured Copper Interfaces for Enhanced Boiling," *Small*, vol. 4, no. 8, pp. 1084–1088, Aug. 2008. [Online]. Available: https://onlinelibrary.wiley.com/doi/abs/10.1002/smll.200700991

[149] Y. Im, Y. Joshi, C. Dietz, and S. S. Lee, "Enhanced boiling of a dielectric liquid on copper nanowire surfaces," *Int. J. Micro-Nano Scale Transp*, vol. 1, no. 1, pp. 79–95, 2010.

[150] M. G. Cooper and T. T. Chandratilleke, "Growth of diffusion-controlled vapour bubbles at a wall in a known temperature gradient," *International Journal of Heat and Mass Transfer*, vol. 24, no. 9, pp. 1475–1492, Sep. 1981. [Online]. Available: http://www.sciencedirect.com/science/article/pii/0017931081902155

[151] A. Zou, D. P. Singh, and S. C. Maroo, "Early Evaporation of Microlayer for Boiling Heat Transfer Enhancement," *Langmuir*, vol. 32, no. 42, pp. 10 808–10 814, Oct. 2016. [Online]. Available: https://doi.org/10.1021/acs.langmuir.6b02642

[152] G. Akovali, *Plastics, rubber and health*. iSmithers Rapra Publishing, 2007.

[153] E. T. J. Rochford, A. H. C. Poulsson, J. Salavarrieta Varela, P. Lezuo, R. G. Richards, and T. F. Moriarty, "Bacterial adhesion to orthopaedic implant materials and a novel oxygen plasma modified PEEK surface," *Colloids and Surfaces B: Biointerfaces*, vol. 113, pp. 213–222, Jan. 2014. [Online]. Available: http://www.sciencedirect.com/science/article/pii/S0927776513005808

[154] K. Page, M. Wilson, and I. P. Parkin, "Antimicrobial surfaces and their potential in reducing the role of the inanimate environment in the incidence of hospital-acquired infections," *Journal of Materials Chemistry*, vol. 19, no. 23, pp. 3819–3831, 2009.

[155] A. Y. Peleg and D. C. Hooper, "Hospital-acquired infections due to gram-negative bacteria," *New England Journal of Medicine*, vol. 362, no. 19, pp. 1804–1813, 2010.

[156] L. G. Glance, P. W. Stone, D. B. Mukamel, and A. W. Dick, "Increases in mortality, length of stay, and cost associated with hospital-acquired infections in trauma patients," *Archives of surgery*, vol. 146, no. 7, pp. 794–801, 2011.

[157] "Hospital-Acquired Infections: Practice Essentials, Background, Pathophysiology," May 2017. [Online]. Available: http://emedicine.medscape.com/article/967022-overview

[158] H. A. Maddah, "Polypropylene as a promising plastic: A review," *American Journal of Polymer Science*, vol. 6, no. 1, pp. 1–11, 2016.

[159] P. Chen, *Material Science and Engineering: Proceedings of the 3rd Annual 2015 International Conference on Material Science and Engineering (ICMSE2015, Guangzhou, Guangdong, China, 15-17 May 2015)*. CRC Press, 2016.

[160] M. Sandholzer, K. Bernreitner, and K. Klimke, "Polypropylene and polypropylene-elastomer blends for medical packaging," in *AIP Conference Proceedings*, vol. 1779, no. 1. AIP Publishing, 2016, p. 110001.

[161] M. Râpă, E. Matei, P. N. Ghioca, C. Cincu, and M. Niculescu, "Structural changes of modified polypropylene with thermoplastic elastomers for medical devices applications," *Journal of adhesion science and Technology*, vol. 30, no. 16, pp. 1727–1740, 2016.

[162] P. L. Tran, E. Huynh, P. Pham, B. Lacky, C. Jarvis, T. Mosley, A. N. Hamood, R. Hanes, and T. Reid, "Organoselenium polymer inhibits biofilm formation in

polypropylene contact lens case material," *Eye & contact lens*, vol. 43, no. 2, pp. 110–115, 2017.

[163] P. B. Vermeltfoort, J. M. Hooymans, H. J. Busscher, and H. C. van der Mei, "Bacterial transmission from lens storage cases to contact lenseseffects of lens care solutions and silver impregnation of cases," *Journal of Biomedical Materials Research Part B: Applied Biomaterials: An Official Journal of The Society for Biomaterials, The Japanese Society for Biomaterials, and The Australian Society for Biomaterials and the Korean Society for Biomaterials*, vol. 87, no. 1, pp. 237–243, 2008.

[164] "Medical Plastics Market Size, Share, Trend | Industry Report, 2018-2025." [Online]. Available: https://www.grandviewresearch.com/industry-analysis/medical-plastics-market

[165] A. Q. Le, N. D. Nguyen, C. T. Vu, Q. H. Nguyen *et al.*, "Preparation of polypropylene/silver nano-zeolite plastics and evaluation of antibacterial and mechanical properties," *International Journal of Composite Materials*, vol. 6, no. 4, pp. 89–94, 2016.

[166] K. Delgado, R. Quijada, R. Palma, and H. Palza, "Polypropylene with embedded copper metal or copper oxide nanoparticles as a novel plastic antimicrobial agent," *Letters in applied microbiology*, vol. 53, no. 1, pp. 50–54, 2011.

[167] H. Palza, S. Gutiérrez, K. Delgado, O. Salazar, V. Fuenzalida, J. I. Avila, G. Figueroa, and R. Quijada, "Toward tailor-made biocide materials based on poly (propylene)/copper nanoparticles," *Macromolecular rapid communications*, vol. 31, no. 6, pp. 563–567, 2010.

[168] P. Suktha, K. Lekpet, P. Siwayaprahm, and M. Sawangphruk, "Enhanced mechanical properties and bactericidal activity of polypropylene nanocomposite with dual-function silica–silver core-shell nanoparticles," *Journal of Applied Polymer Science*, vol. 128, no. 6, pp. 4339–4345, 2013.

[169] E. Fages, J. Pascual, O. Fenollar, D. García-Sanoguera, and R. Balart, "Study of antibacterial properties of polypropylene filled with surfactant-coated silver nanoparticles," *Polymer Engineering & Science*, vol. 51, no. 4, pp. 804–811, 2011.

[170] A. Störmer, J. Bott, D. Kemmer, and R. Franz, "Critical review of the migration potential of nanoparticles in food contact plastics," *Trends in food science & technology*, vol. 63, pp. 39–50, 2017.

[171] S. Addo Ntim, T. A. Thomas, T. H. Begley, and G. O. Noonan, "Characterisation and potential migration of silver nanoparticles from commercially available polymeric food contact materials," *Food Additives & Contaminants: Part A*, vol. 32, no. 6, pp. 1003–1011, 2015.

[172] J. Fabrega, S. N. Luoma, C. R. Tyler, T. S. Galloway, and J. R. Lead, "Silver nanoparticles: behaviour and effects in the aquatic environment," *Environment international*, vol. 37, no. 2, pp. 517–531, 2011.

[173] S. Pillai, R. Behra, H. Nestler, M. J.-F. Suter, L. Sigg, and K. Schirmer, "Linking toxicity and adaptive responses across the transcriptome, proteome, and phenotype of chlamydomonas reinhardtii exposed to silver," *Proceedings of the National Academy of Sciences*, p. 201319388, 2014.

[174] I. Chopra, "The increasing use of silver-based products as antimicrobial agents: a useful development or a cause for concern?" *Journal of antimicrobial chemotherapy*, vol. 59, no. 4, pp. 587–590, 2007.

[175] Y.-F. Yang, Y. Li, Q.-L. Li, L.-S. Wan, and Z.-K. Xu, "Surface hydrophilization of microporous polypropylene membrane by grafting zwitterionic polymer for anti-biofouling," *Journal of Membrane Science*, vol. 362, no. 1-2, pp. 255–264, 2010.

[176] E. J. Nodoushan, N. G. Ebrahimi, and M. Ayazi, "An anti-bacterial approach to nanoscale roughening of biomimetic rice-like pattern pp by thermal annealing," *Applied Surface Science*, vol. 423, pp. 1054–1061, 2017.

[177] ASTM International, West Conshohocken, PA, "Standard classification system and basis for specification for polypropylene injection and extrusion materials," ASTM International, Tech. Rep. [Online]. Available: http://www.astm.org/cgi-bin/resolver.cgi?D4101-17

[178] ——, "Standard test method for linear dimensional changes of nonrigid thermoplastic sheeting or film at elevated temperature," 2002.

[179] B. J. Bachmann, "Pedigrees of some mutant strains of escherichia coli k-12." *Bacteriological reviews*, vol. 36, no. 4, p. 525, 1972.

[180] B. P. Cormack, R. H. Valdivia, and S. Falkow, "Facs-optimized mutants of the green fluorescent protein (gfp)," *Gene*, vol. 173, no. 1, pp. 33–38, 1996.

[181] G. Bertani, "Studies on lysogenesis i.: The mode of phage liberation by lysogenic escherichia coli1," *Journal of bacteriology*, vol. 62, no. 3, p. 293, 1951.

[182] R. M. Shanks, J. L. Sargent, R. M. Martinez, M. L. Graber, and G. A. O'toole, "Catheter lock solutions influence staphylococcal biofilm formation on abiotic surfaces," *Nephrology Dialysis Transplantation*, vol. 21, no. 8, pp. 2247–2255, 2006.

[183] D. R. Absolom, F. V. Lamberti, Z. Policova, W. Zingg, C. J. van Oss, and A. W. Neumann, "Surface thermodynamics of bacterial adhesion." *Applied and environmental microbiology*, vol. 46, no. 1, pp. 90–97, 1983.

[184] H. Miao and C. Jierong, "Inactivation of escherichia coli and properties of medical poly (vinyl chloride) in remote-oxygen plasma," *Applied Surface Science*, vol. 255, no. 11, pp. 5690–5697, 2009.

[185] K. Yamauchi, Y. Yao, T. Ochiai, M. Sakai, Y. Kubota, and G. Yamauchi, "Antibacterial activity of hydrophobic composite materials containing a visible-light-sensitive photocatalyst," *Journal of Nanotechnology*, vol. 2011, 2011.

[186] T. D. Jacobs, T. Junge, and L. Pastewka, "Quantitative characterization of surface topography using spectral analysis," *Surface Topography: Metrology and Properties*, vol. 5, no. 1, p. 013001, 2017.

[187] M. Flemming, L. Coriand, and A. Duparré, "Ultra-hydrophobicity through stochastic surface roughness," *Journal of Adhesion Science and Technology*, vol. 23, no. 3, pp. 381–400, 2009.

[188] B.-S. Kim, N. Bernet, P. Sunderland, and J.-A. Manson, "Numerical analysis of the dimensional stability of thermoplastic composites using a thermoviscoelastic approach," *Journal of Composite Materials*, vol. 36, no. 20, pp. 2389–2403, 2002.

[189] Y. Huang, C. Huang, Y. Zhong, and S. Yi, "Preparing superhydrophobic surfaces with very low contact angle hysteresis," *Surface Engineering*, vol. 29, no. 8, pp. 633–636, 2013.

[190] M. Żenkiewicz, "Methods for the calculation of surface free energy of solids," *Journal of Achievements in Materials and Manufacturing Engineering*, vol. 24, no. 1, pp. 137–145, 2007.

[191] F. M. Fowkes, "Donor-acceptor interactions at interfaces," *The Journal of Adhesion*, vol. 4, no. 2, pp. 155–159, 1972.

[192] ——, "Attractive forces at interfaces," *Industrial & Engineering Chemistry*, vol. 56, no. 12, pp. 40–52, 1964.

[193] Y. Yuan, M. P. Hays, P. R. Hardwidge, and J. Kim, "Surface characteristics influencing bacterial adhesion to polymeric substrates," *RSC Advances*, vol. 7, no. 23, pp. 14 254–14 261, 2017.

[194] S. BinAhmed, A. Hasane, Z. Wang, A. Mansurov, and S. Romero-Vargas Castrillon, "Bacterial adhesion to ultrafiltration membranes: Role of hydrophilicity, natural organic matter, and cell-surface macromolecules," *Environmental science & technology*, vol. 52, no. 1, pp. 162–172, 2017.

[195] L. G. Harris, D. O. Meredith, L. Eschbach, and R. G. Richards, "Staphylococcus aureus adhesion to standard micro-rough and electropolished implant materials," *Journal of Materials Science: Materials in Medicine*, vol. 18, no. 6, pp. 1151–1156, 2007.

[196] K. J. Edwards and A. D. Rutenberg, "Microbial response to surface microtopography: the role of metabolism in localized mineral dissolution," *Chemical Geology*, vol. 180, no. 1-4, pp. 19–32, 2001.

[197] M. Katsikogianni and Y. Missirlis, "Concise review of mechanisms of bacterial adhesion to biomaterials and of techniques used in estimating bacteria-material interactions," *Eur Cell Mater*, vol. 8, no. 3, pp. 37–57, 2004.

[198] W. Barthlott and C. Neinhuis, "Purity of the sacred lotus, or escape from contamination in biological surfaces," *Planta*, vol. 202, no. 1, pp. 1–8, 1997.

[199] M. Zhang, S. Feng, L. Wang, and Y. Zheng, "Lotus effect in wetting and self-cleaning," *Biotribology*, vol. 5, pp. 31–43, 2016.

[200] L. Zhang, Z. Zhou, B. Cheng, J. M. DeSimone, and E. T. Samulski, "Superhydrophobic behavior of a perfluoropolyether lotus-leaf-like topography," *Langmuir*, vol. 22, no. 20, pp. 8576–8580, 2006.

[201] Y. Liu, J. Tang, R. Wang, H. Lu, L. Li, Y. Kong, K. Qi, and J. Xin, "Artificial lotus leaf structures from assembling carbon nanotubes and their applications in hy-

drophobic textiles," *Journal of Materials chemistry*, vol. 17, no. 11, pp. 1071–1078, 2007.

[202] A. Muñoz-Bonilla and M. Fernández-García, "Polymeric materials with antimicrobial activity," *Progress in Polymer Science*, vol. 37, no. 2, pp. 281–339, 2012.

[203] A. L. Hook, C.-Y. Chang, J. Yang, J. Luckett, A. Cockayne, S. Atkinson, Y. Mei, R. Bayston, D. J. Irvine, R. Langer *et al.*, "Combinatorial discovery of polymers resistant to bacterial attachment," *Nature biotechnology*, vol. 30, no. 9, p. 868, 2012.

[204] R. E. Weisbarth, M. M. Gabriel, M. George, J. Rappon, M. Miller, R. Chalmers, and L. Winterton, "Creating antimicrobial surfaces and materials for contact lenses and lens cases," *Eye & contact lens*, vol. 33, no. 6, pp. 426–429, 2007.

[205] N. Cole, E. B. Hume, A. K. Vijay, P. Sankaridurg, N. Kumar, and M. D. Willcox, "In vivo performance of melimine as an antimicrobial coating for contact lenses in models of clare and clpu," *Investigative ophthalmology & visual science*, vol. 51, no. 1, pp. 390–395, 2010.

[206] E. Tacconelli, G. Smith, K. Hieke, A. Lafuma, and P. Bastide, "Epidemiology, medical outcomes and costs of catheter-related bloodstream infections in intensive care units of four european countries: literature-and registry-based estimates," *Journal of Hospital Infection*, vol. 72, no. 2, pp. 97–103, 2009.

[207] L. Zhao, P. K. Chu, Y. Zhang, and Z. Wu, "Antibacterial coatings on titanium implants," *Journal of Biomedical Materials Research Part B: Applied Biomaterials*, vol. 91, no. 1, pp. 470–480, 2009.

[208] A. Cunha, A.-M. Elie, L. Plawinski, A. P. Serro, A. M. B. do Rego, A. Almeida, M. C. Urdaci, M.-C. Durrieu, and R. Vilar, "Femtosecond laser surface texturing of titanium as a method to reduce the adhesion of staphylococcus aureus and biofilm formation," *Applied Surface Science*, vol. 360, pp. 485–493, 2016.

[209] R. B. Simmons, L. J. Rose, S. A. Crow, and D. G. Ahearn, "The occurrence and persistence of mixed biofilms in automobile air conditioning systems," *Current Microbiology*, vol. 39, no. 3, pp. 141–145, Sep. 1999, 00027. [Online]. Available: http://link.springer.com/article/10.1007/s002849900435

[210] L. Hall-Stoodley and P. Stoodley, "Biofilm formation and dispersal and the transmission of human pathogens," *Trends in Microbiology*, vol. 13, no. 1, pp.

7–10, Jan. 2005. [Online]. Available: http://www.sciencedirect.com/science/article/pii/S0966842X04002586

[211] P. N. Danese, "Antibiofilm Approaches: Prevention of Catheter Colonization," *Chemistry & Biology*, vol. 9, no. 8, pp. 873–880, Aug. 2002. [Online]. Available: http://www.sciencedirect.com/science/article/pii/S1074552102001928

[212] N. Dror, M. Mandel, Z. Hazan, and G. Lavie, "Advances in Microbial Biofilm Prevention on Indwelling Medical Devices with Emphasis on Usage of Acoustic Energy," *Sensors*, vol. 9, no. 4, pp. 2538–2554, Apr. 2009. [Online]. Available: http://www.mdpi.com/1424-8220/9/4/2538

[213] Q. L. Feng, J. Wu, G. Q. Chen, F. Z. Cui, T. N. Kim, J. O. Kim, and others, "A mechanistic study of the antibacterial effect of silver ions on Escherichia coli and Staphylococcus aureus," *Journal of biomedical materials research*, vol. 52, no. 4, pp. 662–668, 2000. [Online]. Available: https://www.researchgate.net/profile/Qing_Feng/publication/247939816_A_mechanistic_study_of_the_antibacterial_effect_of_silver_ions_onEscherichia_coli_andStaphylococcus_aureus/links/53fbd9380cf2364ccc045db0.pdf

[214] S. H. Sicherer and D. Y. M. Leung, "Advances in allergic skin disease, anaphylaxis, and hypersensitivity reactions to foods, drugs, and insects in 2012," *The Journal of Allergy and Clinical Immunology*, vol. 131, no. 1, pp. 55–66, Jan. 2013.

[215] T. E. Stoker, E. K. Gibson, and L. M. Zorrilla, "Triclosan exposure modulates estrogen-dependent responses in the female wistar rat," *Toxicological Sciences: An Official Journal of the Society of Toxicology*, vol. 117, no. 1, pp. 45–53, Sep. 2010.

[216] B. A. Cunha, "Antibiotic Side Effects," *Medical Clinics of North America*, vol. 85, no. 1, pp. 149–185, Jan. 2001. [Online]. Available: http://www.sciencedirect.com/science/article/pii/S0025712505703096

[217] I. Chopra, "The increasing use of silver-based products as antimicrobial agents: a useful development or a cause for concern?" *Journal of Antimicrobial Chemotherapy*, vol. 59, no. 4, pp. 587–590, Apr. 2007. [Online]. Available: http://jac.oxfordjournals.org/content/59/4/587

[218] C. Desrousseaux, V. Sautou, S. Descamps, and O. Traoré, "Modification of the surfaces of medical devices to prevent microbial adhesion and biofilm formation," *Journal of hospital Infection*, vol. 85, no. 2, pp. 87–93, 2013.

[219] E. P. Ivanova, J. Hasan, H. K. Webb, V. K. Truong, G. S. Watson, J. A. Watson, V. A. Baulin, S. Pogodin, J. Y. Wang, M. J. Tobin *et al.*, "Natural bactericidal surfaces: mechanical rupture of pseudomonas aeruginosa cells by cicada wings," *Small*, vol. 8, no. 16, pp. 2489–2494, 2012.

[220] S. Pogodin, J. Hasan, V. A. Baulin, H. K. Webb, V. K. Truong, T. H. P. Nguyen, V. Boshkovikj, C. J. Fluke, G. S. Watson, J. A. Watson *et al.*, "Biophysical model of bacterial cell interactions with nanopatterned cicada wing surfaces," *Biophysical journal*, vol. 104, no. 4, pp. 835–840, 2013.

[221] A. M. Whatmore and R. H. Reed, "Determination of turgor pressure in bacillus subtilis: a possible role for k+ in turgor regulation," *Microbiology*, vol. 136, no. 12, pp. 2521–2526, 1990.

[222] E. P. Ivanova, J. Hasan, H. K. Webb, G. Gervinskas, S. Juodkazis, V. K. Truong, A. H. Wu, R. N. Lamb, V. A. Baulin, G. S. Watson *et al.*, "Bactericidal activity of black silicon," *Nature communications*, vol. 4, p. 2838, 2013.

[223] G. Hazell, P. W. May, P. Taylor, A. H. Nobbs, C. C. Welch, and B. Su, "Studies of black silicon and black diamond as materials for antibacterial surfaces," *Biomater. Sci.*, vol. 6, pp. 1424–1432, 2018. [Online]. Available: http://dx.doi.org/10.1039/C8BM00107C

[224] L. Brown, J. M. Wolf, R. Prados-Rosales, and A. Casadevall, "Through the wall: extracellular vesicles in gram-positive bacteria, mycobacteria and fungi," *Nature Reviews Microbiology*, vol. 13, no. 10, p. 620, 2015.

[225] T. Diu, N. Faruqui, T. Sjöström, B. Lamarre, H. F. Jenkinson, B. Su, and M. G. Ryadnov, "Cicada-inspired cell-instructive nanopatterned arrays," *Scientific reports*, vol. 4, p. 7122, 2014.

[226] X. Ye and L. Qi, "Two-dimensionally patterned nanostructures based on monolayer colloidal crystals: Controllable fabrication, assembly, and applications," *Nano Today*, vol. 6, no. 6, pp. 608–631, 2011.

[227] Y. Yu and L. Cao, "Coupled leaky mode theory for light absorption in 2d, 1d, and 0d semiconductor nanostructures," *Optics express*, vol. 20, no. 13, pp. 13 847–13 856, 2012.

[228] G. D. Moon, T. I. Lee, B. Kim, G. Chae, J. Kim, S. Kim, J.-M. Myoung, and U. Jeong, "Assembled monolayers of hydrophilic particles on water surfaces," *ACS nano*, vol. 5, no. 11, pp. 8600–8612, 2011.

[229] S. Wu, F. Zuber, J. Brugger, K. Maniura-Weber, and Q. Ren, "Antibacterial au nanostructured surfaces," *Nanoscale*, vol. 8, no. 5, pp. 2620–2625, 2016.

[230] J. Li, J. Ahn, D. Liu, S. Chen, X. Ye, and T. Ding, "Evaluation of ultrasound-induced damage to escherichia coli and staphylococcus aureus by flow cytometry and transmission electron microscopy," *Appl. Environ. Microbiol.*, vol. 82, no. 6, pp. 1828–1837, 2016.